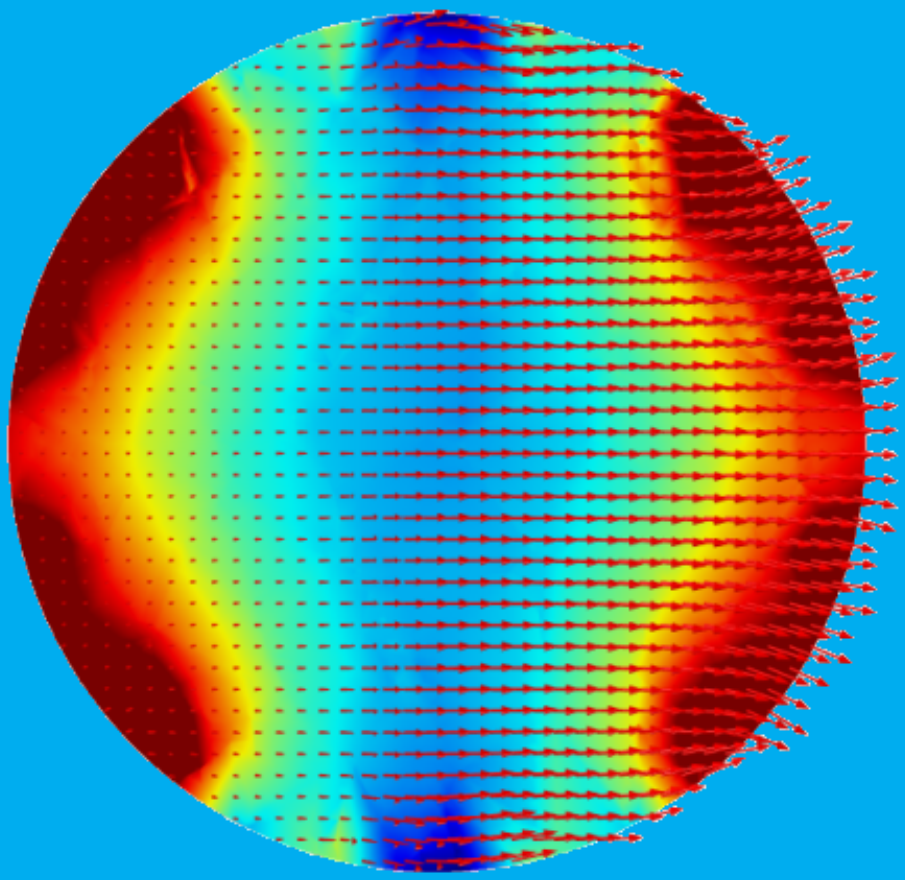

Technische Universiteit Delft

Image Reconstruction in MRI: The Possibilities of Portable, Low-cost MRI Scanners

M.S. Wijchers

TU Delft

Image Reconstruction in MRI:

The Possibilities of Portable, Low-cost MRI Scanners

by

M.S. Wijchers

A thesis submitted in partial fulfillment of the requirements for the degree of

Master of Science
in Applied Mathematics

at the Delft University of Technology,
to be defended publicly on Wednesday August 31, 2016 at 14:00.

Student number:	4087666	
Project duration:	November 1, 2015 – August 31, 2016	
Thesis committee:	Dr. Ir. M.B. van Gijzen,	TU Delft
	Prof. Dr. Ir. A.H. Heemink,	TU Delft
	Dr. Ir. R. Remis,	TU Delft
	Prof. Dr. A. Webb.	LUMC

This thesis is confidential and cannot be made public before August 31, 2016.

TU Delft

Abstract

Hydrocephalus is one of the most common abnormalities affecting the nervous system of children around the globe. Especially in developing countries hydrocephalus is a large problem. It is often left untreated resulting in suffering, brain damage, developmental delays and ultimately death. This makes an early detection more opportune than ever.
In standard MRI it is typical to adjust the hardware of the imager to minimise the effort needed in the reconstruction. MRI scanners are also heavy and expensive. Therefore a start is made in developing a sufficiently accurate image reconstruction algoritm that is able to effectively process signals produced by a low-cost MRI scanner.

An analytic signal is set up for the new prototype magnetic resonance imager and a measurement model consisting of a set of linear equations is derived. For two dimensions, a new encoding method (rotating the magnet) is implemented in a Matlab program. The Matlab program constructs the signal with a Shepp-Logan phantom image and then solves the set of linear equations to reconstruct the original image. Care needs to be taken when it comes to several practical aspects as wel as theoretical issues.

The model is analysed on its performance through tests on the Nyquist rate and its sensitivity to perturbations on the background magnetic flux density field. Satisfying the Nyquist rate is important when translating discrete signal samples in a continous signal. Perturbations due to human measurement errors have to be avoided where as perturbations due to limiting tools can be dealt with. Another study looks at the right balance between the number of rotations, the frequency bandwidth and the effective rank of the system matrix. The performance of iterative solvers CGLS and CGNE are tested. CGLS is the better choice when noise is included in the model. Which is the incentive for a short study about the p-norm. CGLS has been combined with Tikhonov regularisation and showed the best performance with regularisation matrix $L = I$ and extra a-priori information compared to other regularisation matrices.

Keywords MRI · Magnetic resonance modeling · Image reconstruction · Portable low-cost MRI · iterative solvers · Tikhonov regularisation

Preface

My Bachelor Applied Mathematics made clear for me that modeling and numerical mathematics are my area of interest. Applying that knowledge to medical purposes in my Bachelor's project was a good fit for me and therefore something I knew I would enjoy for my Master thesis as well. This thesis concludes the programme of the Master Applied Mathematics at Delft University of Technology.

This project was formulated by Andrew Webb, Martin van Gijzen and Rob Remis. Andrew Webb is a full professor and director at the 'C.J. Gorter Center for High-field MRI', which is part of the Leiden University Medical Center (LUMC). Martin was the daily supervisor of this project on behalf of TU Delft. He did this alongside Rob Remis, assistant professor in the Circuits and Systems group at TU Delft. I would like to sincerely thank these supervisors for their guidance, entertaining conversations and motivational talks. Furthermore, I would like to thank my friend Kirsten Koolstra for telling me about her thesis at the Gorter Center, as her enthousiasm contributed for me choosing this project.

One day a week I worked at the C.J. Gorter Center and I enjoyed listening to all the researchers telling enthousiastically about their respective projects. These days were definitely different from EEMCS's third floor at the TU Delft. So a thank you goes to the Gorter group for the nice work environment, fun breaks and drinks.

M.S. Wijchers
Delft, August 2016

Contents

List of Figures

List of Tables

1 Introduction

Hydrocephalus, or "water on the brain", is one of the most common abnormalities affecting the nervous system of children around the globe. Infant hydrocephalus can already be present at birth. Examples of causes are birth defects, genetic abnormalities or infections during pregnancy. It is also possible to acquire hydrocephalus in later stages. Examples of underlying causes in this case are meningitis, bleeding in the brain, head trauma or other injuries occuring before, during or after delivery.
Especially in developing countries hydrocephalus is a large problem, because the underlying causes happen more often and the life-saving neurosurgical care is limited. To emphasise this problem with some numbers: of approximately 400.000 newborns (with hydrocephalus) a year worldwide, 79% are born in a developing nation. which makes an early detection more opportune than ever.

So what is hydrocephalus and what are the actual causes? It is a medical condition that develops when the normal flow and absorption of cerebrospinal fluid (CSF) in the brain is partially or fully blocked. This leads to excessive accumulation of fluid in the ventricles of the brain. The difference between a healthy infant and an infant with hydrocephalus is shown in Figure 1.1. If hydrocephalus is left untreated, it will not only lead to pain and suffering, but also to significant brain damage, severe developmental delay, blindness, and ultimately death [17].

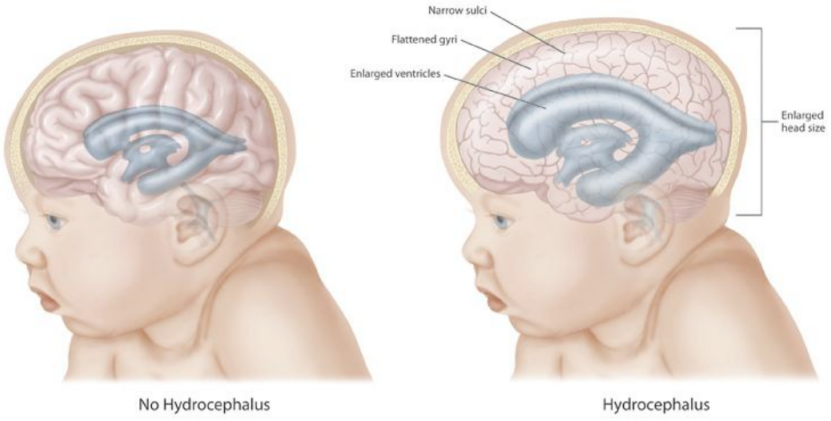

Figure 1.1: Difference between a child without and with hydrocephalus respectively.

CURE children's (charity) hospital of Uganda in Mbale is the only neurosurgical unit for children in sub-saharan Africa. They treat 4000 children with hydrocephalus a year. As many as 20 cases arrive every single day and many of them are severe because they have been left untreated for a long period of time. The lack of searching for treatment is caused by the long transfers, lacking finance and the African culture which considers the large head circumference (hydrocephalus) as a bad omen. Therefore, the parent is not supported by the community, which increases the problem as the parent can't provide the financial cost on her own.

Currently, medical practitioners in Africa have to expose young patients to repeated CT scans and X-ray radiation. Developing an inexpensive, portable magnetic resonance imaging (MRI) scanner could help make the diagnosis and treatment of infant hydrocephalus available and affordable in the remote regions. It would also prevent the children from being exposed to unnecessary levels of radiation, which they would get in a CT scan.

Standard MRI used in hospitals use a high magnetic field, typically 1.5 T or higher. At the LUMC there is even a 7 T MRI scanner. These devices require active cooling, including a bath of liquid helium and liquid nitrogen. A low-field portable device will operate at a field strength in the millitesla range (~ 200 mT), which is at least a thousand times weaker. This results in a signal-to-noise ratio that has been infeasible in the past and hence the image quality needs to be improved. Also the expensive hardware needs to be replaced by a cheaper alternative resulting in a device, which also has to be portable.

1.1. Motivation

MRI scanners consist of a main magnet, magnetic field gradient coils and RF coils. Traditional Fourier MRI methods rely on homogeneous static main fields (B_0) and high strength linear spatial encoding magnetic fields. These gradient fields are produced by expensive magnetic gradient coils. In MRI, it is typical to *adjust the hardware of the imager to minimise the effort needed in the image reconstruction.* This means that conventional scanners use high cost superconducting wire, liquid cryogen cooling systems, high power supplies and electronics.

Using a portable, low-cost scanner can be used for diagnosing hydrocephalus, but are also compelling for other applications where power, siting, and cost constraints prohibit conventional scanners. Examples include clinics in rural or underdeveloped areas, military field hospitals, sports arenas, and ambulances. However, it is difficult to simply scale-down MRI scanners to portable, low cost devices, because of the important link between the expensive hardware and the image reconstruction. Hence the development of a simplified MRI scanner relies on the design of new image reconstruction methods and simplified hardware. The function of the heavy switchable linear gradient coils could be replaced by a rotating permanent magnet (which creates an inhomogeneous stationary field). Instead of striving for a homogeneous field, the inhomogeneity could be used as a spatial encoding magnetic field.

Image reconstruction generally uses fast fourier transform (FFT) to convert the so called 'k-space' data to an image, when equidistant k-space sampling is assumed. However, if the static magnetic field and gradient fields are not linear, then the resulting image is distorted when FFT is applied directly. To obtain the image, a different image reconstruction algorithm has to be developed.

1.2. Research goals

As mentioned before, the 'scaling down' of conventional MRI cannot be done easily because the set-up of the hardware makes it impossible to use the current image reconstruction method. Therefore this main goal is

to develop a sufficiently accurate image reconstruction algorithm that is able to effectively process signals produced by a low-cost MRI scanner.

There are limitations in the choice of the set-up of the hardware, as the main magnet was already constructed before the start of this project. Hence the magnetic field is already determined and it is certain that using gradient coils is not an option because it uses great amounts of power and is too expensive. This leaves little room for changes in the hardware.

To reach the main goal some research questions have been formulated at the start of this thesis project. Because of the nature of the project (i.e. more research than development), some of the questions (or rather its underlying questions) had to be modified. The project offers many challenges which were not considered at the initial moment of formulating the research questions.
In Section 1.2.1 the original research questions will be explained shortly. Section 1.2.2 will discuss the ideas of how to approach those questions. It includes several modifications to the research questions.

1.2.1. Research questions

The questions below lead us further in achieving the main goal. These questions could lead to other questions which will be tried to answer or will be left for future research (depending on the time and necessity to answer them within this project).

1. Determine a correct formulation of the received signal.
2. What measuring method fits best to minimise the effort/time of the image reconstruction?
3. What are the conditions for the image to be *accurate enough*?
4. How do signal noise and system errors affect the image reconstruction and how can they be minimised?
5. Which regularisation method(s), preconditioner(s) and numerical solver(s) should be implemented to maximise results?
6. When the model is applied to real data, are the results still satisfactory? If not, how can the model be adjusted to deal with these inaccuracies/errors/noises.

1.2.2. Methodology

Note that the methodology is only a starting point in answering the research questions. The explanations are numerated respectively to the research questions. To fully understand these, background knowledge of MRI is required. It can also be found in Chapters 2, 3 and 4.

1. The formulation for the received signal was already set up in the literature study and is given in (3.57). This expression will be used when working with the real data. The formulation can be validated after experiments have been conducted. There open questions include; what is the sensitivity $c(\mathbf{r})$ and how to implement relaxation times $T_2(\mathbf{r})$.
2. There are two methods which seem to be the most obvious after considering the hardware constraints:
   - Change the frequency (bandwidth) of the pulse to excite spins at different locations within the circle. This gives information only at those locations. This is illustrated in Figure 1.2.

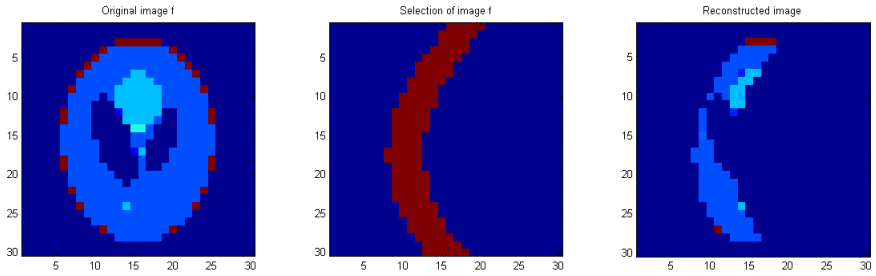

Figure 1.2: From left to right: original image used to make a signal (30×30 pixels), spatial locations corresponding to frequency bandwidth selection and a reconstruction. Reconstruction with the assumption of no noise, all frequencies in the bandwidth are received with the same sensitivity and the sample is placed in the lefthandside of the magnet. The effect of T_2 is ignored.

   - Rotate the sample or rotate the magnet around the sample. This way the excited spins are in the same locations within the circle but they correspond to a different part of the sample.

   Note that a combination of the two methods is also possible.
3. It is evident that the experts/doctors using the MRI (images) should give a measure for the accuracy (resolution). This measure needs to be translated to conditions and/or parameter settings in the model.
4. Different kinds of signal noise and system errors can be made, whether that are human mistakes or hardware errors.

- When signal noise is added, it will be complex white gaussian noise. However the amount and shape/distribution of the noise depends on the chosen frequency band and probably on some other factors. This will result in differences between image reconstruction of the artificial and the real data.
- A perturbation analysis will show how errors (human mistakes and hardware limitations) influence the accuracy of the image.

These differences need to be identified and included in the model.

5. We do not have a positive definite, well-conditioned matrix A. Therefore we cannot use the conjugate gradient (CG) method but resort to more general variations of CG. We will consider CGLS and CGNE, among others, as numerical solvers.

   Furthermore, we have to solve an ill-posed problem, which means we will need to add conditions for regularisation. The conditions are linked to the physics of a problem, therefore the conditions need to be explored for our specific case. Tikhonov and another regularisation method (1-norm optimisation) from [23] will be tested. Another subquestion is what basis to choose for the pixels. A rectangular function is chosen as a basis, but many other basis functions can be chosen. The implications of a change of basis are changes in system matrix A.

   All in all, it is important to understand the nature of the matrix A. How much information is in the system?

6. When an experiment is conducted with real phantom data, we will know what the outcome should be, i.e. the image is available to us. If there are differences between image reconstruction of the artificial, the real data and the available image, they need to be identified and processed in the model.

1.3. Chapter outline

This thesis is structured in the following way:

Chapter 2: The principles of MRI
To understand the above questions and implications more thoroughly, some background information needs to be researched. An overview of the workings of a conventional magnetic resonance imager is given. This is to understand the function of all different parts of the hardware and their importance in the image reconstruction.

Chapter 3: Model set-up
The hardware of the new prototype magnetic resonance imager is explained. This is the hardware that is given for use in the first possible experiments and was decided on before the start of this project. For this set-up, the image reconstruction method needs to be developed. The set-up is used to derive an expression for the signal that will be generated.
From the derived analytic signal we will set up a measurement model: a set of linear equations which need to be solved.

Chapter 4: Numerical solvers and regularisation
Chapter 4 explains some basic ideas used to solve the set of linear equations in the image reconstruction.

Chapter 5: Matlab programme for image reconstruction The image reconstruction programme based on the measurement model is explained. This includes some practical aspects for the use of the programme, as well as some important theoretical issues.

Chapter 6: Analysis of the model
A few of the returning questions concerning the model will be explained more thoroughly: the consequences of perturbations in the field strength and imaging using T_2 and T_2^*. These are larger issues because of the inhomogeneity of the magnetic field.

Chapter 7: Results
This chapter contains the most important results of the model: the iterative solvers and regularisation methods will be discussed.

Chapter 8: Conclusions and future research
The most important conclusions are explained. The focus lies on clarifying the answered questions and the remaining unanswered questions with its challenges.

1.4. Software

Throughout this project we will make use of several software packages.

`COMSOL` Multiphysics is a finite element analysis, solver and simulation software package with an interactive environment for modeling and simulating scientific and engineering problems. The model set-up for real data is mimicked in `COMSOL` and used for the validation of the magnetic field. It could also be possible to generate artificial data with `COMSOL`.

MATLAB is used to create the artificial signal to use for the image reconstruction. Also the implementation of reconstruction algorithms, as well as the testing of several numerical solvers and regularisation methods.

The MATLAB toolbox called 'Regularization Tools', created by Per Christian Hansen [12] was originally used for the investigation and implementation of regularisation methods and numerical solvers in our model. For example, the algorithm `cgls.m` by Per Christian Hansen has been used in the early stages of the project, but is now replaced by `cgls.m` by Martin van Gijzen. The Matlab application 'Curve Fitting Tool' is used to find a full magnetic flux density field.

2

Principles of a Magnetic Resonance Imager

The workings of a magnetic resonance imager (MRI scanner) can be broken down into three parts. First a signal must be generated and transmitted. This signal has some effect on the body and this is detected in the form of a receiving signal. The last step is to translate those signals to an image; localising the different kinds of tissue in the field of view.

It is stressed that this chapter covers the standard MRI. The workings of our set-up require some important and drastic changes. The information in this section originates from [18].

2.1. Signal Generation

To fully understand the basic principle of standard MRI the study starts at a microscopic level. The object subject to MRI can be broken down into molecules, molecules into atoms and those in turn can be broken down in nuclei and electrons. A fundamental property of nuclei is that they possess an angular momentum **J**, called *spin*, if they have odd atomic weights/numbers. An ensemble of nuclei of the same type is referred to as a *spin system* .
A large part of the human body contains hydrogen atoms, which have one single proton. It has electrical charge and it rotates around its own axis if it has nonzero spin. The *magnetic moment* causes a magnetic field. The spin angular momentum and magnetic moment are related by

$$\vec{\mu} = \gamma \mathbf{J} \tag{2.1}$$

where γ is the gyromagnetic ratio.
The magnitude of $\vec{\mu}$ is certain under any conditions (with or without an external magnetic field) due to thermal random motion. Therefore, at thermal equilibrium, no *net* magnetic field exists around a macroscopic object. To activate this macroscopic magnetism the spin vectors need to line up. This can be done by exposing the object to a strong external magnetic field of strength B_0, applied in the z direction of the laboratory frame. This is defined by

$$\mathbf{B}_0 = B_0 \mathbf{i}_z. \tag{2.2}$$

Depending on the *magnetic quantum number*, m_I, there are several possible orientations for $\vec{\mu}$ with respect to the direction of the external field. The angle θ between $\vec{\mu}$ and $\mathbf{B}_0$ can be calculated using

$$\cos(\theta) = \frac{\mu_z}{|\vec{\mu}|} = \frac{m_I}{\sqrt{I(I+1)}}. \tag{2.3}$$

For a spin$-1/2$ system, any magnetic moment vector can have two possible orientations. The vector points up (parallel) or points down (antiparallel).
The torque that $\vec{\mu}$ experiences from the external field is equal to the rate of change of its angular momentum

$$\frac{d\mathbf{J}}{dt} = \vec{\mu} \times B_0 \mathbf{i}_z \Rightarrow \frac{d\vec{\mu}}{dt} = \gamma \vec{\mu} \times B_0 \mathbf{i}_z \tag{2.4}$$

which can be solved to find

$$\begin{cases} \mu_{xy}(t) & = \mu_{xy}(0)e^{-i\gamma B_0 t} \\ \mu_z(t) & = \mu_z(0) \end{cases} . \tag{2.5}$$

This system of equations describes a precession of $\vec{\mu}$ about the $\mathbf{B}_0$ field, called *nuclear precession*. Note that the angular frequency of nuclear precession is

$$\omega_0 = \gamma B_0 \tag{2.6}$$

which is known as the *Larmor frequency*.
In the presence of B_0, the pointing up spins are the lower-energy state and the pointing down spins are the higher-energy state. The uneven spin distribution between the two spin states occurs because a spin is more likely to take the lower-energy state. An observable macroscopic bulk magnetization vector $\mathbf{M}(t)$ is generated from a spin system. The spin system is said to be *magnetised*. The vector $\mathbf{M}$ aligns along the $\mathbf{B}_0$ field lines. Although there is a microscopic transverse component for each magnetic moment vector, the transverse component of $\mathbf{M}$ is zero at equilibrium because the precessing magnetic moments have random phases.

An RF pulse is a synonym of the $\mathbf{B}_1(t)$ field, so called as the $\mathbf{B}_1$ field is shortlived and oscillates in the radio-frequency range. An RF pulse generates an oscillating $\mathbf{B}_1$ field perpendicular to the $\mathbf{B}_0$ field.
The time-dependent behaviour of $\mathbf{M}$ in the presence of an applied magnetic field $\mathbf{B}_1$ is described by the *Bloch equation*

$$\frac{d\mathbf{M}}{dt} = \gamma\mathbf{M} \times \mathbf{B} - \frac{M_x\mathbf{i}_x + M_y\mathbf{i}_y}{T_2} - \frac{(M_z - M_z^0)\mathbf{i}_z}{T_1} \tag{2.7}$$

where $\mathbf{M} = M_x\mathbf{i}_x + M_y\mathbf{i}_y + M_z\mathbf{i}_z$, M_z^0 is the thermal equilibruim for $\mathbf{M}$ in $\mathbf{B}_0$ and T_1 and T_2 time constants characterizing the relaxation process of a spin system after an RF pulse and $\mathbf{B} = \mathbf{B}_0 + \mathbf{B}_1$ the field experienced by the nuclei.

A rotating frame is a coordinate system whose transverse plane rotates clockwise at an angular frequency ω. To distinguish it from the conventional stationary frame, we use x', y', and z' to denote the three orthogonal axes of this frame. In the rotational frame (when the last two terms of the Bloch equation are disregarded, $\omega_1 \gg 1/T_1, 1/T_2$) the magnetisation becomes

$$\begin{cases} M_{x'}(t) & = 0 \\ M_{y'}(t) & = M_z^0 \sin(\omega_1 t) \quad 0 \le t \le \tau_p \\ M_{z'}(t) & = M_z^0 \cos(\omega_1 t) \end{cases} \tag{2.8}$$

where $\omega_1 = \gamma B_1$, τ_p the time duration of the pulse and x', y', z' the axes in the rotating frame. The precession of $\mathbf{M}$ about the $\mathbf{B}_1$ field is called *forced precession*. As a result of this, the bulk magnetisation is tipped away from the z'-axis, creating a measurable transverse component $M_{x'y'}$. The angle between $\mathbf{M}$ and the z-axis is called the *flip angle* and is denoted by α.

After a magnetized spin system has been perturbed from its thermal equilibrium state by an RF pulse, it will return to this state, provided the external force is removed and sufficient time is given. This process is called *free precession*; a recovery of the longitudinal magnetization M_z, called *longitudinal relaxation (T_1)*, and the destruction of the transverse magnetisation M_{xy}, called *transverse relaxation (T_2)*.

2.2. Signal Detection

According to the Faraday law of induction, the voltage induced in the receiver coil is

$$\mathscr{E}(t) = -\frac{d\Phi(t)}{dt} = -\frac{d}{dt}\int_{\text{object}} \mathbf{B}_r(\mathbf{r}) \cdot \mathbf{M}(\mathbf{r}, t)\, d\mathbf{r} \tag{2.9}$$

where $\mathbf{B}_r(\mathbf{r})$ is the laboratory frame magnetic field at location $\mathbf{r} = (x, y, z)$ produced by a hypothetical unit direct current flowing in the coil. With some manipulations this equation can be written as

$$\mathscr{E}(t) = \int_{\text{object}} \omega(\mathbf{r}) \left| B_{r,xy}(\mathbf{r}) \right| \left| M_{xy}(\mathbf{r}, 0) \right| e^{-t/T_2(\mathbf{r})} \cos\left(-\omega(\mathbf{r})t + \phi_e(\mathbf{r}) + \frac{\pi}{2}\right) d\mathbf{r} \tag{2.10}$$

with ϕ_e the initial phase shift introduced by the RF excitation.
It is a basic signal expression that explicitly shows the dependence of a detected voltage signal on the laboratory frame transverse magnetisation $M_{xy}(\mathbf{r},0)$, the free precession frequency $\omega(\mathbf{r})$, and the detection sensitivity of the receiver coil $B_{r,xy}(\mathbf{r},0)$.

The voltage signal is high-frequency because the transverse magnetisation vector precesses at the Larmor frequency, as observed at the laboratory frame. This can pose unnecessary problems. Therefore, $\mathscr{E}(t)$ is moved to a low-frequency band using the *phase-sensitive detection* (PSD) method, or *signal demodulation* method. It consists of multiplying $\mathscr{E}(t)$ by a reference sinusoidal signal and then low-pass-filtering it to remove the high-frequency component. After applying the PSD method, the voltage signal is denoted as $\mathscr{E}_{\text{psd.}}$.

Using a sinusoidal signal $2\cos\omega_0 t$ simplifies $\mathscr{E}$ to

$$\mathscr{E}_{\text{psd1}}(t) = \omega_0 \int_{\text{object}} \left|B_{r,xy}(\mathbf{r})\right| \left|M_{xy}(\mathbf{r},0)\right| e^{-t/T_2(\mathbf{r})} \cos\left(-\Delta\omega(\mathbf{r})\, t + \phi_e(\mathbf{r}) - \phi_r(\mathbf{r}) + \frac{\pi}{2}\right) d\mathbf{r} \tag{2.11}$$

with ϕ_r is the reception phase angle. As $\Delta\omega(\mathbf{r})$ is the precession frequency in the rotating frame, $\mathscr{E}_{\text{psd1}}$ is often regarded as the signal detected in the rotating frame. A drawback is the fact that we cannot determine whether the signal precesses clockwise or counterclockwise. To overcome this problem a second PSD system $\mathscr{E}_{\text{psd2}}$ is used with reference signal $2\sin(\omega_0 t)$, resulting in

$$\mathscr{E}_{\text{psd2}}(t) = \omega_0 \int_{\text{object}} \left|B_{r,xy}(\mathbf{r})\right| \left|M_{xy}(\mathbf{r},0)\right| e^{-t/T_2(\mathbf{r})} \sin\left(-\Delta\omega(\mathbf{r})\, t + \phi_e(\mathbf{r}) - \phi_r(\mathbf{r}) + \frac{\pi}{2}\right) d\mathbf{r}. \tag{2.12}$$

Let $S(t) = \mathscr{E}_{\text{psd1}}(t) + i\mathscr{E}_{\text{psd2}}(t)$. Then,

$$S(t) = \omega_0 \int_{\text{object}} \left|B_{r,xy}(\mathbf{r})\right| \left|M_{xy}(\mathbf{r},0)\right| e^{-t/T_2(\mathbf{r})} e^{-\mathrm{i}\left(\Delta\omega(\mathbf{r})\, t - \phi_e(\mathbf{r}) + \phi_r(\mathbf{r}) - \pi/2\right)} d\mathbf{r}. \tag{2.13}$$

Using $\left|B_{r,xy}(\mathbf{r})\right| e^{-\mathrm{i}\phi_r(\mathbf{r})} = B^*_{r,xy}(\mathbf{r})$ and $\left|M_{xy}(\mathbf{r},0)\right| e^{\mathrm{i}\phi_e(\mathbf{r})} = M_{xy}(\mathbf{r},0)$ and omitting the scaling constant $\omega_0 e^{\mathrm{i}\pi/2}$, this results in signal expression

$$S(t) = \int_{\text{object}} B^*_{r,xy}(\mathbf{r}) M_{xy}(\mathbf{r},0) e^{-t/T_2(\mathbf{r})} e^{-\mathrm{i}\Delta\omega(\mathbf{r})\, t} d\mathbf{r}. \tag{2.14}$$

2.3. Signal Characteristics

Free Induction Decays (FID) are the result of a single pulse on a nuclear spin system. 'Free' comes from the fact that the signal is generated by the free precession of the bulk magnetisation vector about the $\mathbf{B}_0$ field, 'induction' from the fact that the signal is produced based on Faraday's law of induction and 'decay' indicates the decrease of signal amplitude in time. FID signals are the most basic form of signals from a spin system after a pulse excitation. The decay rate of a FID signal is strongly tied to the underlying spectral distribution. In case of a single spectral component, the FID signal bears a characteristic T_2 decay.
Another form of signal is an echo signal. It can be generated by multiple RF pulses or by magnetic field gradient reversal. A gradient field can dephase and rephase a signal in a controlled fashion so that one or multiple echo signals can be created. A gradient field $\mathbf{B}_G$ in the context of MRI is a special kind of inhomogeneous field whose z-component varies linearly along a specific direction called the *gradient direction*. It is an x-gradient field if $B_{G,z} = xG_x$, with G_x the x-gradient.
After applying an $\alpha-$degree RF pulse a gradient can be turned on, say a negative x-gradient. As a result, spins in different x-positions will acquire different phases, which can be expressed in the rotating frame as

$$\phi(x,t) = \gamma \int_0^t -G_x x\, d\bar{t} = -\gamma G_x x t \quad 0 \le t \le \tau. \tag{2.15}$$

Gradually the loss of spin phase will become worse and the signal decays to zero. At that point a positive x-gradient is turned on to rephase the spins and the signal regrows (echoes). This technique is called *gradient echo*. A FID signal is the transient response of a spin system after a pulse excitation. The magnitude of the signal is dependent on a number of parameters, in particular the flip angle, the total number of spins in the sample and the magnetic field strength.

2.4. Signal Localisation

As the acquired signal generated is a sum of local signals from all parts of the object, it is necessary to differentiate local signals from different parts of a given object.
In standard MRI two things are essential to selectively excite spins in a slice: a gradient field and a shaped RF pulse. An RF pulse can only be frequency selective, and spins at different spatial locations will be excited in the same way if they resonate at the same frequency. Therefore, to make an RF pulse spatially selective, it is necessary to make the spin resonance frequency position-dependent; to vary linearly along the slice-select direction. A simple yet effective way to accomplish this is to augment the B_0 field with a linear gradient field *during the excitation period.* Note that we will not be able to use this technique due to the lack of the gradient coils and therefore the linear gradient fields.
After a signal has been activated by a selective or nonselective pulse, spatial information can be encoded into the signal during the free precession period. There are two ways to encode spatial information: *frequency encoding (fe)* and *phase encoding (pe)*.
Frequency encoding makes the oscillation frequency of an activated MR signal linearly dependent on its spatial origin by applying a linear gradient field $\mathbf{B}_{fe}$. The Larmor frequency at position $\mathbf{r}$ is

$$\omega(\mathbf{r}) = \omega_0 + \gamma \mathbf{G}_{fe} \cdot \mathbf{r} \tag{2.16}$$

and after demodulation results in the signal

$$S(t) = \int_{\text{object}} \rho(\mathbf{r}) e^{-\gamma \mathbf{G}_{fe} \cdot \mathbf{r} t} d\mathbf{r}. \tag{2.17}$$

For a fixed frequency-encoded gradient vector $\mathbf{G}_{fe} = (G_x, G_y, G_z)$, spatial information is frequency-encoded only along the direction of the gradient vector. This means only one-dimensional spatial localisation along the gradient direction is achieved. For the two-dimensional spatial localisation, phase encoding is needed.

After an RF pulse, a gradient is turned on for a short interval T_{pe} and then turned off. The initial phase angle is given by $\phi(\mathbf{r}) = -\gamma \mathbf{G}_{pe} \cdot \mathbf{r} T_{pe}$.

If a frequency-encoding gradient is turned on in the x-direction and a phase-encoding gradient in the y-direction, then in the k-space notation the signal $S(t)$ is proportional to

$$S(k_x, k_y) \propto \int_{\text{slice}} \int_{\text{slice}} \rho(x, y) e^{-\mathrm{i} k_x x} e^{-\mathrm{i} k_y y} dx dy \tag{2.18}$$

where $k_x = \gamma G_x t$ and $k_y = \gamma G_y T_{pe}$.

2.5. 2D Imaging and reconstruction

Denoting the desired image function by $I(x, y)$, it is related to the underlying three-dimensional function ρ by

$$I(x, y) = \int_{-\infty}^{\infty} \rho(x, y, z) dz. \tag{2.19}$$

Substituting Equation (2.19) in (2.18), the basic imaging equation is the two-dimensional Fourier transform

$$S(k_x, k_y) = \int_{-\infty}^{\infty} \int_{-\infty}^{\infty} I(x, y) e^{-\mathrm{i}(k_x x + k_y y)} dx dy. \tag{2.20}$$

The problem of reconstructing a function from its Fourier transform samples can be formulated as follows:

$$\begin{array}{ll} \text{Given} & S(\mathbf{k}_n) = \int I(\mathbf{r}) e^{-\mathrm{i}\mathbf{k}_n \cdot \mathbf{r}} d\mathbf{r} \quad \mathbf{k}_n \in \mathfrak{D} \\ \text{determine} & I(\mathbf{r}) \end{array} \tag{2.21}$$

where $\mathfrak{D}$ contains the set of k-space points at which measured data are collected.

3

Model set-up for real data

Before the start of this project, some thought had already be given to the model set-up as mentioned in the research goals. Firstly, taking into account the pre-described hardware means that we cannot create the strong homogeneous magnetic field $\mathbf{B}_0$ as in Equation (2.2). Instead the idea is to use permanent magnets in such a way that a field is created *mainly* in one direction and using the inhomogeneities in image reconstruction methods. This means that the largest components of the set-up are the main magnet (consisting of permanent magnets) and the coil which transmits the pulse and receives the signal.

The hardware is put together by Jelle Hockx, a physics student at Leiden University. His work is still in progress, but can eventually be found online [16].

3.1. The main magnet

This section will show the set-up of the main magnet as hardware (using permanent magnets) and software (using `COMSOL`).

3.1.1. Hardware

A circular permanent magnet is constructed with twelve magnets (see Figure 3.1). Its outer radius is 2 inches and the inner radius is 1 inch. The magnets are placed in a non-magnetic material in order to prevent outside influences on the magnetic field.

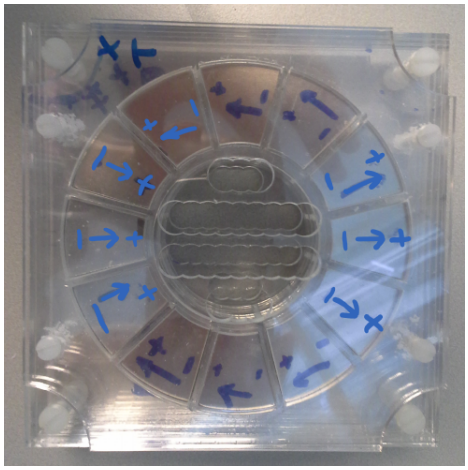

Figure 3.1: Main magnet constructed by the LUMC. The arrows show the direction of the magnetisation for each magnet.

The magnets are polarized as in Figure 3.1. This means that three different kinds of magnets are used, shown in Figure 3.2. There are six magnets as in Figure 3.2a, three as in Figure 3.2b and three as in Figure 3.2c.

(a) Magnetised South on outside face, strength of 0.624 T on the outside radius.

(b) Magnetised North on outside face, strength of 0.624 T on the outside radius.

(c) Magnetised through circumference, strength of 0.721 T on the outside radius.

Figure 3.2: Magnets used to construct the main magnet. Dimensions of 2" outside radius ×1" inside radius ×1" × 30°, made of NdFeB.

Note that the strengths of the magnets are different. Using these magnets with different magnetisations gives a very particular field. When the magnets are arranged in a different order or with different numbers of the kinds of magnets, then the field will be different (see Figure 3.3, [26]). For example, using only the magnets from Figure 3.2c the resulting field will be highest at the edges of the circle and zero in the middle. This is if all magnets are placed such that the south pole of one is next to the north pole of the next.
In our case, by arranging the magnets in the particular way as shown in the figure, it is almost like a Halbach cylinder (see Figure 3.3, $k = 2$) which creates a uniform field inside the bore. However, as it is not exactly arranged in that way, the field is almost uniform in one direction but differs in strength per location.

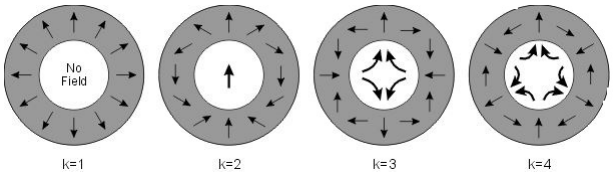

Figure 3.3: Halbach arrays with different magnetisation vectors, our main magnet is similar to the situation $k = 2$ [26].

In Figure 3.1 a thin slice of perspex plate is placed on both sides of the magnet covering the center. Holes are made such that a cylindrical measurement tool can be put through both sides and be held in place. This tool can measure the magnetic field inside the main magnet. In Figure 3.4 the results of the measurements are shown. The measurement tool allows measuring data in a parallel and perpendicular direction. The parallel axis is the z-axis (direction of main field) and perpendicular axis is the x-axis. These measurements are done at five different heights (y-axis), spaced equally. For all further work in two dimensions, the middle measurement layer is chosen in the (x, z)-plane.

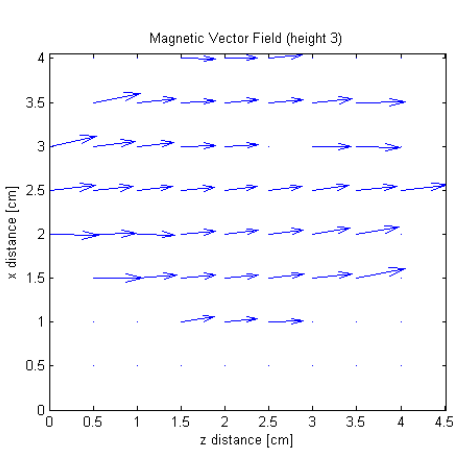

(a) Direction magnetic field in (x, z)-plane

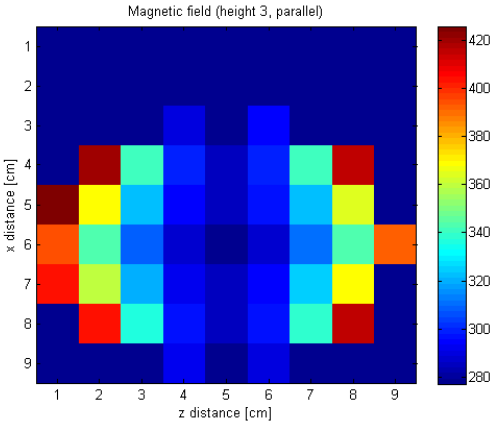

(b) Strength magnetic field (mT) in (x, z)-plane. The NaN's are represented as 0, the lowest value (dark blue).

Figure 3.4: The measurements of the magnetic field of the main magnet.

The measurements are entered into a 9×9 matrix. To create this many measurement points, the holes overlap and there is another set of perspex plates to cover different locations. More measurement points are not possible with the current measuring tools because of accuracy. The measurement matrix is square, but the

measurement points are inside a circular area. Therefore, the entries of locations which cannot be measured (e.g. close to or inside a magnet) are represented as 'NaN' (Not a Number).
The magnetic field in the LUMC magnet was measured and it points (roughly) from left to right, along the z-axis (see Figure 3.4a). The magnetic flux density field can be written as a main field of strength B_0 and small variations in x, y and z directions. For every 3D case it holds that

$$\mathbf{B}^{\text{tot}}(\mathbf{r}) = B_x(\mathbf{r})\mathbf{i}_x + B_y(\mathbf{r})\mathbf{i}_y + B_z(\mathbf{r})\mathbf{i}_z \tag{3.1}$$

where $B_k(\mathbf{r})\mathbf{i}_k$ (and $k = x, y, z$) is made up of a constant field over all positions $B_0\mathbf{i}_k$ and a term $\Delta B_k(\mathbf{r})\mathbf{i}_k$ for the variations in the k-direction. It now follows that in this project the total magnetic flux density field is

$$\mathbf{B}^{\text{tot}}(\mathbf{r}) = \Delta B_x(\mathbf{r})\mathbf{i}_x + \Delta B_y(\mathbf{r})\mathbf{i}_y + \Delta B_z(\mathbf{r})\mathbf{i}_z + B_0\mathbf{i}_z. \tag{3.2}$$

It is desired that this field varies *only* in the z direction, i.e. $\Delta B_x = \Delta B_y = 0$, to limit the difficulty of the problem. In the z-direction there should be a varying strength of the field per location. The measurement results show larger deviations occuring at the edges, the points closest to the magnet. The strength of the magnetic field is depicted in Figure 3.4b. It varies from 277 mT to 426 mT in the z-direction, with an average of 328 mT. The average of the perpendicular field (x) is 28 mT, which is about 8,5% of the average parallel field. This small deviation can also be seen in Figure 3.4a. Note that nothing can be determined about ΔB_y, as these measurements have not been made (only the parallel and perpendicular directions, the z and x directions, at different heights). The variations in the y direction are assumed to be of similar size as ΔB_x and therefore also small compared to ΔB_z.

The field strength matrix, depicted in Figure 3.4b, has asymmetric properties. The values are actually in a 7×9 matrix. This is not something that was expected; the measurements are taken within the main magnet circle which *is* symmetric. The explanation is as follows: in every hole of Figure 3.5 a measurement is taken. As visible in Figure 3.5a and 3.5b some perspex plate is needed between the columns (2.5 mm). This was forgotten in the calculations, resulting in a greater distance in one direction compared to the perpendicular direction. Hence the measurement points in the horizontal z-direction are closer togehter than the vertical x-direction. Figure 3.5c shows that there is symmetry in the overall area.
The explanation of the single measurement point the right hand side of Figure 3.4b (location (6,9) in the matrix) compared to the three measurement points on the left hand side of Figure 3.4b (position $(5-7, 1)$ in the matrix) is that the tool did not fit well in the other two holes. Therefore measurements could not be taken at these locations.

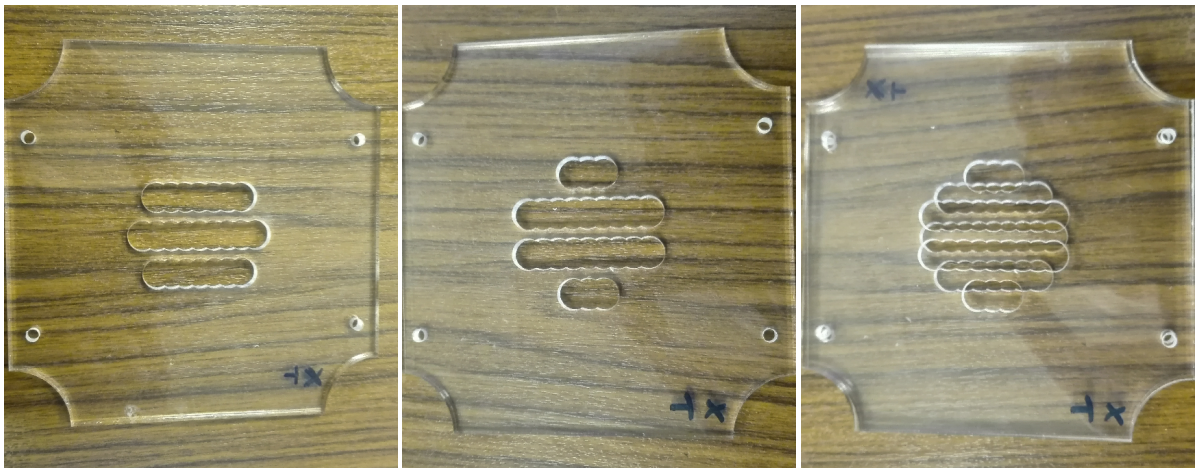

(a) Perspex measuring slide one. (b) Perspex measuring slide two. (c) Perspex measuring slides combined.

Figure 3.5: The magnetic field measurement positions of the main magnet.

3.1.2. Software

In COMSOL Multiphysics the main magnet is recreated as shown in Figure 3.6, using the Magnetic Fields, No Currents interface. Here the outer rectangular prism is the mathematical workspace. It contains the main magnet set-up as shown in Section 3.1.

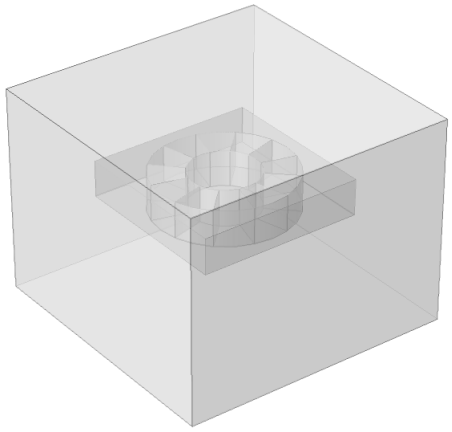

Figure 3.6: COMSOL model of the main magnet, showing the magnetic flux density in Tesla in colours and the arrow volume shows the direction of the magnetic flux density.

All the parts of the geometry are given the same material, namely air. Also, the physics needs to be assigned to model the LUMC magnet as closely as possible. This is done by assigning a *Magnetic Flux Conservation*. All elements are modelled using the consitutive relation

$$\mathbf{B}(\mathbf{r}, t) = \mu_0 \mu_r \mathbf{H}(\mathbf{r}, t) \tag{3.3}$$

where the relative permeability μ_r is given by the material (air). Next we override the physics for the magnets. The constitutive relation that holds is

$$\mathbf{B}(\mathbf{r}, t) = \mu_0 \left(\mathbf{H}(\mathbf{r}, t) + \mathbf{M}(\mathbf{r}, t)\right) \tag{3.4}$$

where the magnetisation vector $\mathbf{M}$ needs to be given for each magnet.

In Figure 3.7 the results are plotted. One can see in Figure 3.7a that the magnetisation directions per magnet deviate slightly across the magnet. It is mentioned because it has an influence on the magnetic field in Figure 3.7b. This figure shows the strength of the magnetic flux density in the z direction. This means that Figure 3.7b should resemble Figure 3.4b (the COMSOL and real, measured magnetic field strengths).

The value in the center of the circle in the COMSOL model is about 30 mT lower than the measured value. On the edges, i.e. the highest values, are about 60 mT higher. These differences could also have occured due to deviations of the magnet strengths, a small change could cover these differences. Both patterns are like a saddle, but the COMSOL pattern increases more gradually from the center to the edges in the z-direction. The measurements show that the values are lower in the middle area and increase faster at the edges.

3.2. The RF coil

When a radio frequency (RF) pulse is sent out, only the spins which have the same frequency are excited. Looking at the strength variation of the field, its shape is like a saddle. This means selecting a frequency will excite spins in two semicircles when the field is interpolated and the 2D center plane (height) is used.

The RF coil is not completely finished. The background information which is used is found in [19].
For the image reconstruction there is something to consider: a very short steep pulse will give a broad frequency bandwidth. A longer, less steep pulse will result with a smaller bandwidth.

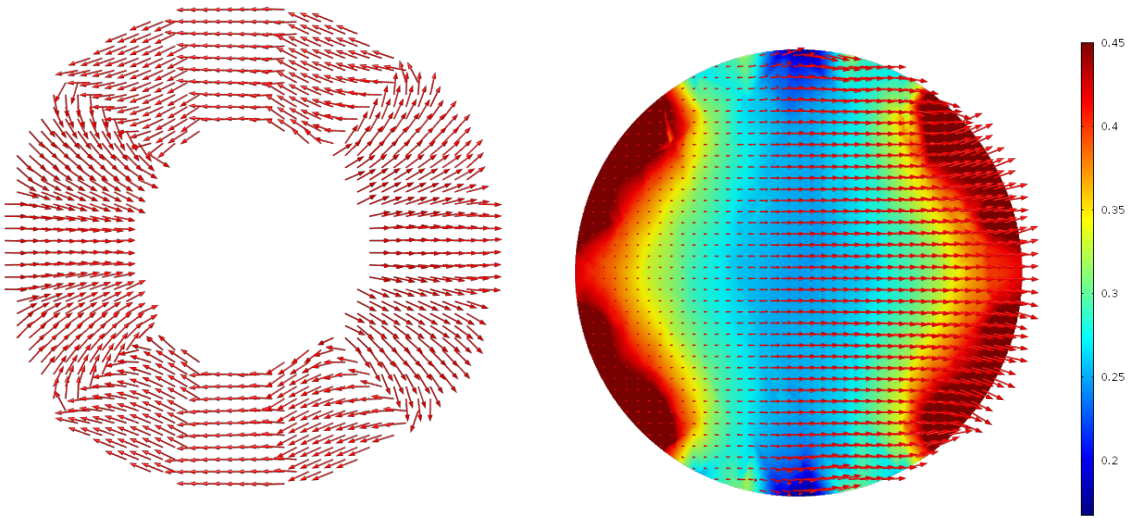

(a) Direction magnetisation vectors of the magnets in (x,z)-plane

(b) Strength magnetic field (T) in (x,z)-plane.

Figure 3.7: The magnetic field of the main magnet modelled in COMSOL.

The challenges that come from the hardware are researched by Jelle Hockx and will be discussed in his report [16].

3.3. Signal generation and detection

In this section a signal will be derived, starting from the very beginning. A connection can be made to some of the equations in Chapter 2, but uses the set-up as described in this chapter. A compact version of this section can be found in [21].

The magnetisation $\mathbf{M}(\mathbf{r},t)$ serves as a source and this vector follows from the Bloch equation. Slow time variations result in the possibility to treat the electromagnetic field as magneto quasi static. The associated basic field equations are

$$\nabla \times \mathbf{H}(\mathbf{r},t) = \mathbf{0}, \quad \mathbf{r} \in \mathbb{R}^3 \tag{3.5}$$

$$\nabla \cdot \mathbf{B}(\mathbf{r},t) = \mathbf{0}, \quad \mathbf{r} \in \mathbb{R}^3 \tag{3.6}$$

where $\mathbf{H}$ is the magnetic field strength and $\mathbf{B}$ the magnetic flux density. For notational convenience, the dependence on position and time will be dropped and reintroduced later on.
The object imaged has a bounded support $\mathbb{D}$, where the magnetisation vector is nonzero. The constitutive relations are

$$\mathbf{B} = \mu_0 \mathbf{H}, \quad \mathbf{r} \notin \mathbb{D} \tag{3.7}$$

$$\mathbf{B} = \mu_0 (\mathbf{H} + \mathbf{M}), \quad \mathbf{r} \in \mathbb{D}. \tag{3.8}$$

Equation (3.6) is satisfied if it is rewritten as $\mathbf{B} = \nabla \times \mathbf{A}$. The vector field $\mathbf{A}$ is the so-called magnetic vector potential. It is required that this potential satisfies the Coulomb gauge $\nabla \cdot \mathbf{A} = 0$. This can be used to solve the constitutive relations for $\mathbf{A}$. Starting with Equation (3.7), we take the rotation of $\mathbf{B}$ and substitute $\mathbf{B} = \nabla \times \mathbf{A}$ which results in

$$\mathbf{B} = \mu_0 \mathbf{H} \tag{3.9}$$

$$\nabla \times \mathbf{B} = \mu_0 \nabla \times \mathbf{H} = \mathbf{0} \tag{3.10}$$

$$\nabla \times (\nabla \times \mathbf{A}) = \mathbf{0} \tag{3.11}$$

$$\nabla \nabla \cdot \mathbf{A} - \nabla^2 \mathbf{A} = \mathbf{0} \tag{3.12}$$

As the resulting equation needs to satisfy the Coulomb gauge, the first term disappears and we need to solve $\nabla^2 \mathbf{A} = \mathbf{0}$ for the outside domain. As for inside the $\mathbb{D}$ domain, we begin with Equation (3.8). Using the same

manipulations it results in solving $\nabla^2\mathbf{A} = -\mu_0\nabla\times\mathbf{M}$. Combining these equations, we have

$$\nabla^2\mathbf{A} = -\mu_0\mathbf{J}^M, \quad \mathbf{r}\in\mathbb{R}^3 \tag{3.13}$$

with

$$\mathbf{J}^M = \begin{cases} \nabla\times\mathbf{M} & \mathbf{r}\in\mathbb{D} \\ \mathbf{0} & \mathbf{r}\notin\mathbb{D}. \end{cases} \tag{3.14}$$

A particular solution to the Poisson equation $-\Delta u = f$ is $u(\mathbf{x}) = \frac{1}{4\pi}\int\int\int_{\mathbb{R}^3}\frac{f(\xi)}{\|\mathbf{x}-\xi\|}d\xi$ so the solution of Equation (3.13) is

$$\mathbf{A}(\mathbf{r},t) = \frac{\mu_0}{4\pi}\int_{\mathbf{r}'\in\mathbb{D}}\frac{\mathbf{J}^M(\mathbf{r}',t)}{|\mathbf{r}-\mathbf{r}'|}dV, \quad \mathbf{r}\in\mathbb{R}^3 \tag{3.15}$$

This can be written as

$$\mathbf{A}(\mathbf{r},t) = \frac{\mu_0}{4\pi}\int_{\mathbf{r}'\in\mathbb{D}}\nabla'\frac{1}{|\mathbf{r}-\mathbf{r}'|}\times\mathbf{M}(\mathbf{r}',t)dV, \quad \mathbf{r}\in\mathbb{R}^3 \tag{3.16}$$

Now next we turn to Faraday's law of induction. It makes use of the magnetic flux Φ_B through a hypothetical surface Σ whose boundary is a wire loop. Since the wire loop may be moving, the surface Σ may be time dependent. The magnetic flux is defined as

$$\Phi_B = \int\int_{\Sigma(t)}\mathbf{B}(\mathbf{r},t)\cdot d\tilde{\mathbf{A}} \tag{3.17}$$

where $d\tilde{\mathbf{A}}$ is an element of the surface area of the moving surface Σ.
When the flux changes, because $\mathbf{B}$ changes or because the wire loop is moved/deformed, Faraday's law of induction states that the wire loop acquires an electromotive force, $\mathscr{E}$. It is defined by the rate of change of the magnetic flux

$$\mathscr{E}(t) = -\frac{d\Phi_B}{dt}. \tag{3.18}$$

Using Stokes's integral theorem, we can write

$$\mathscr{E}(t) = -\frac{d}{dt}\int_{\mathbf{r}\in\Sigma}(\nabla\times\mathbf{A})\cdot d\tilde{\mathbf{A}} = -\frac{d}{dt}\int_{\mathbf{r}\in\alpha}\mathbf{A}\cdot\tau\,dl \tag{3.19}$$

Substitution of Equation (3.16) in Equation (3.19) results in the electromotive force as measured by the receiver coil in MRI

$$\mathscr{E}(t) = -\frac{d}{dt}\int_{\mathbf{r}'\in\mathbb{D}}\mathbf{M}(\mathbf{r}',t)\cdot\mathbf{W}(\mathbf{r}')dV, \tag{3.20}$$

where

$$\mathbf{W}(\mathbf{r}') = \frac{\mu_0}{4\pi}\nabla'\times\int_{\mathbf{r}\in\alpha}\frac{1}{|\mathbf{r}-\mathbf{r}'|}\cdot\tau\,dl \tag{3.21}$$

Note that $\mathbf{W}(\mathbf{r})$ is a weighting vector and is often referred to as the receive field, since it can be interpeted as the magnetic flux density generated by the receive coil carrying a unit current. $\mathbf{M}(\mathbf{r},t)$ is the magnetisation in the sample domain $\mathbb{D}$. This derived equation is the same as the given Equation (2.9).

The static magnetic flux density field inside the ring magnet is directed predominantly from 'left to right'. The reference frame will be such that this direction coincides with the positive z-direction. As we assume it is only *predominantly* in the z-direction, the total magnetic flux density will also have x and y components. The strength of the field will also vary in the z component.

$$\mathbf{B}^{\text{tot}}(\mathbf{r}) = \Delta B_x(\mathbf{r})\mathbf{i}_x + \Delta B_y(\mathbf{r})\mathbf{i}_y + \Delta B_z(\mathbf{r})\mathbf{i}_z + B_0\mathbf{i}_z. \tag{3.22}$$

The above equation is such that B_0 is a constant and the perturbations $\Delta B_k(\mathbf{r})$ are small with respect to B_0. This means we assume that

$$\left|\frac{\Delta B_k(\mathbf{r})}{B_0}\right| < 1, \quad \text{for } k = x, y, z \text{ and } \mathbf{r} \in \mathbb{D} \tag{3.23}$$

The Bloch equation is an empirical equation (justified using quantum mechanics) which describes the behaviour of the magnetisation $\mathbf{M}$ for a given magnetic field $\mathbf{B}$. For the above static magnetic field, the z-directed Bloch equations hold

$$\partial_t \mathbf{M} + \gamma \mathbf{B} \times \mathbf{M} + T_1^{-1} M_z \mathbf{i}_z + T_2^{-1} \mathbf{M}_\perp = T_1^{-1} M^{\text{eq}} \mathbf{i}_z \tag{3.24}$$

where T_1 is the longitudinal relaxation time and T_2 the transverse relaxation time. This equation is similar to Equation (2.7) for the normal MRI scanner. In most human tissue, the relaxation times range from tens to thousands of milliseconds and it holds that $T_2 < T_1$. The equation holds for $t > 0$ and is supplemented by the initial condition $\mathbf{M}(t = 0) = \mathbf{M}^0$, where $\mathbf{M}^0$ is a given magnetisation vector. Furthermore, $\mathbf{M}_\perp = M_x \mathbf{i}_x + M_y \mathbf{i}_y$ is the magnetisation in the transverse plane and M^{eq} is the equilibrium magnetisation.
Written out in components, the Bloch equation becomes

$$\begin{aligned} \partial_t M_x + \gamma(M_z B_y - M_y B_z) + T_2^{-1} M_x &= 0 \\ \partial_t M_y + \gamma(M_x B_z - M_z B_x) + T_2^{-1} M_y &= 0 \\ \partial_t M_z + \gamma(M_y B_x - M_x B_y) + T_1^{-1} M_z &= T_1^{-1} M^{\text{eq}}. \end{aligned} \tag{3.25}$$

Arranging the components of the magnetisation in the vector

$$\mathbf{m} = \begin{bmatrix} M_x(\mathbf{r}, t) \\ M_y(\mathbf{r}, t) \\ M_z(\mathbf{r}, t) \end{bmatrix} \tag{3.26}$$

and introducing a *Bloch matrix* as

$$B(t) = B^{\text{rel}} + B_z^\infty(t) + B_\perp^\infty(t) \tag{3.27}$$

where in our case holds $\left(\text{with } \omega_0 = \gamma B^{\text{tot}} = \gamma \left|\mathbf{B}^{\text{tot}}\right|\right)$ that

$$B^{\text{rel}} = \begin{bmatrix} T_2^{-1} & 0 & 0 \\ 0 & T_2^{-1} & 0 \\ 0 & 0 & T_1^{-1} \end{bmatrix}, \quad B_z^\infty(t) = \omega_0 \begin{bmatrix} 0 & -\frac{(B_0+\Delta B_z)}{|B^{\text{tot}}|} & 0 \\ \frac{(B_0+\Delta B_z)}{|B^{\text{tot}}|} & 0 & 0 \\ 0 & 0 & 0 \end{bmatrix} \tag{3.28}$$

$$B_\perp^\infty = \omega_0 \begin{bmatrix} 0 & 0 & \frac{(\Delta B_y)}{|B^{\text{tot}}|} \\ 0 & 0 & -\frac{(\Delta B_x)}{|B^{\text{tot}}|} \\ -\frac{(\Delta B_y)}{|B^{\text{tot}}|} & \frac{(\Delta B_x)}{|B^{\text{tot}}|} & 0 \end{bmatrix}. \tag{3.29}$$

The Bloch equation can now be written as

$$\partial_t \mathbf{m} + \mathbf{B}(t)\mathbf{m} = \mathbf{q} \tag{3.30}$$

with the source vector and initial magnetisation vector respectively given by

$$\mathbf{q} = T_1^{-1}[0, 0, M^{\text{eq}}]^T, \quad \mathbf{m}^0 = [M_x^0, M_y^0, M_z^0]^T \tag{3.31}$$

The Bloch matrix is nonsingular for positive and finite relaxation times T_1 and T_2 and for any magnetic flux density. The solution of the Bloch system of Equation (3.30) can be written in terms of the matrix exponential function as

$$\mathbf{m}(t) = \int_0^t e^{-B(t-\tau)} d\tau \mathbf{q} + e^{-Bt} \mathbf{m}^0, \quad \text{for } t > 0 \tag{3.32}$$

Evaluating the integral, the magnetisation vector can be rewritten

$$\begin{aligned}\mathbf{m}(t) &= e^{-Bt}\int_0^t e^{B\tau}d\tau\mathbf{q} + e^{-Bt}\mathbf{m}^0 \\ &= e^{-Bt}\left(\left(B^{-1}e^{B\tau}\right)\Big|_0^t\right)\mathbf{q} + e^{-Bt}\mathbf{m}^0 \\ &= e^{-Bt}\left(B^{-1}e^{Bt} - B^{-1}\right)\mathbf{q} + e^{-Bt}\mathbf{m}^0 \\ &= B^{-1}\left(I - e^{-Bt}\right)\mathbf{q} + e^{-Bt}\mathbf{m}^0\end{aligned} \tag{3.33}$$

for any magnetic flux density such that the z-directed Bloch equations hold. At this point we assume a special case: the perturbed field has no transversal components. This simplifies the calculations for e^{-Bt} tremendously.
In this case it holds that $\Delta B_x = \Delta B_y = 0$ and therefore $B = B^{\text{rel}} + B_z^\infty$ since $B_\perp^\infty$ vanishes. An important note in this case is that the matrices B^{rel} and B_z^∞ commute, i.e. $B^{\text{rel}}B_z^\infty = B_z^\infty B^{\text{rel}}$. Furthermore, B consists of two blocks:

$$B = \left[\begin{array}{cc|c} T_2^{-1} & -\omega_0 B_z/B^{\text{tot}} & 0 \\ \omega_0 B_z/B^{\text{tot}} & T_2^{-1} & 0 \\ \hline 0 & 0 & T_1^{-1} \end{array}\right] \tag{3.34}$$

therefore it is easy to see that $B\mathbf{e}_3 = T_1^{-1}\mathbf{e}_3$ or rewritten as $B^{-1}\mathbf{e}_3 = T_1\mathbf{e}_3$ and $e^{-Bt}\mathbf{e}_3 = e^{-t/T_1}\mathbf{e}_3$. Evaluating the magnetisation vector in Equation 3.33 with the above relations, it becomes

$$\begin{aligned}\mathbf{m}(t) &= B^{-1}\left(I - e^{-Bt}\right)\mathbf{q} + e^{-Bt}\mathbf{m}^0 \\ &= B^{-1}\left(I - e^{-Bt}\right)T_1^{-1}M^{\text{eq}}\mathbf{e}_3 + e^{-Bt}\mathbf{m}^0 \\ &= T_1\left(I - e^{-Bt}\right)T_1^{-1}M^{\text{eq}}\mathbf{e}_3 + e^{-Bt}\mathbf{m}^0 \\ &= \left(I - e^{-Bt}\right)M^{\text{eq}}\mathbf{e}_3 + e^{-Bt}\mathbf{m}^0 \\ &= \left(I - e^{-t/T_1}\right)M^{\text{eq}}\mathbf{e}_3 + e^{-Bt}\mathbf{m}^0\end{aligned} \tag{3.35}$$

for $t > 0$. Now remember that we want to find the expression for $\mathscr{E}$ in Equation (3.20). Introducing the vector

$$\mathbf{w}(\mathbf{r}) = \begin{bmatrix} B_x^{\text{rec}}(\mathbf{r}) \\ B_y^{\text{rec}}(\mathbf{r}) \\ B_z^{\text{rec}}(\mathbf{r}) \end{bmatrix} \tag{3.36}$$

the electromotive force can be written as

$$\mathscr{E}(t) = -\int_{\mathbf{r}\in\mathbb{D}} \mathbf{w}^T(\mathbf{r})\partial_t\mathbf{m}(\mathbf{r},t)dV. \tag{3.37}$$

The derivative of the magnetisation vector follows as

$$\partial_t\mathbf{m}(t) = T_1^{-1}M^{\text{eq}}e^{-t/T_1}\mathbf{e}_3 - Be^{-Bt}\mathbf{m}^0. \tag{3.38}$$

The eigenvalue decomposition of matrix B_z^∞ is given by

$$B_z^\infty Q = Q\Lambda, \quad Q^*Q = QQ^* = I \tag{3.39}$$

where

$$\Lambda = \begin{bmatrix} i\omega_0 & 0 & 0 \\ 0 & -i\omega_0 & 0 \\ 0 & 0 & 0 \end{bmatrix} \text{ and } Q = \frac{1}{\sqrt{2}}\begin{bmatrix} 1 & 1 & 0 \\ -i & i & 0 \\ 0 & 0 & \sqrt{2} \end{bmatrix}. \tag{3.40}$$

With the eigendecomposition, the second expression in Equation (3.38) can be rewritten as

$$\begin{aligned} Be^{-Bt}\mathbf{m}^0 &= \left(B^{\text{rel}} + B_z^{\infty}\right) e^{-B_z^{\infty} t} e^{-B^{\text{rel}} t}\mathbf{m}^0 \\ &= \left(B^{\text{rel}} + Q\Lambda Q^*\right) Q e^{-\Lambda t} Q^* e^{-B^{\text{rel}} t}\mathbf{m}^0 \\ &= \left(B^{\text{rel}} + Q\Lambda Q^*\right) Q e^{-\Lambda t} Q^* e^{-B^{\text{rel}} t}\mathbf{m}^0 \\ &= Q\left(B^{\text{rel}} + \Lambda\right) e^{-\Lambda t} Q^* e^{-B^{\text{rel}} t}\mathbf{m}^0. \end{aligned} \tag{3.41}$$

Observe that

$$Q^* e^{-B^{\text{rel}} t}\mathbf{m}^0 = \begin{bmatrix} \frac{1}{\sqrt{2}} e^{-t/T_2} M_+^0 \\ \frac{1}{\sqrt{2}} e^{-t/T_2} \overline{M_+^0} \\ e^{-t/T_1} M_z^0 \end{bmatrix}. \tag{3.42}$$

with $M_+^0 = M_x^0 + \mathrm{i}M_y^0$ (the workout of this equation can be found in Appendix B).

Substituting Equation (3.42) into Equation (3.41), an expression can be found for $\partial_t \mathbf{m}(t)$ using Equation (3.38)

$$\partial_t \mathbf{m}(t) = T_1^{-1} e^{-t/T_1}\left(M^{\text{eq}} - M_z^0\right)\mathbf{e}_3 - \sqrt{2} e^{-t/T_2}\,\text{Re}\left[\left(T_2^{-1} + \mathrm{i}\omega_0\right) e^{-\mathrm{i}\omega_0 t} M_+^0 \mathbf{q}_1\right]. \tag{3.43}$$

Since $\omega_0 >> 1/T_{1,2}$ the equation simplifies to

$$\partial_t \mathbf{m}(t) \approx -\sqrt{2} e^{-t/T_2}\,\text{Re}\left[\mathrm{i}\omega_0 e^{-\mathrm{i}\omega_0 t} M_+^0 \mathbf{q}_1\right]. \tag{3.44}$$

Writing M_+^0 in polar form, i.e.

$$M_+^0 = \left|M_+^0\right| e^{\mathrm{i}\varphi_0}, \tag{3.45}$$

Equation (3.44) is equal to

$$\partial_t \mathbf{m}(t) \approx -\sqrt{2} e^{-t/T_2}\left|M_+^0\right|\text{Re}\left[\mathrm{i}\omega_0 e^{-\mathrm{i}(\omega_0 t - \varphi_0)}\mathbf{q}_1\right]. \tag{3.46}$$

Working towards the expression for the electromotive force, this vector is projected onto the receiver vector $\mathbf{w}$,

$$\mathbf{w}^T \partial_t \mathbf{m}(t) \approx -\sqrt{2} e^{-t/T_2}\left|M_+^0\right|\text{Re}\left[\mathrm{i}\omega_0 e^{-\mathrm{i}(\omega_0 t - \varphi_0)}\mathbf{w}^T\mathbf{q}_1\right] \tag{3.47}$$

where

$$\mathbf{w}^T\mathbf{q}_1 = \begin{bmatrix} B_x^{\text{rec}} & B_y^{\text{rec}} & B_z^{\text{rec}} \end{bmatrix} \begin{bmatrix} \frac{1}{\sqrt{2}} \\ -\frac{1}{\sqrt{2}}\mathrm{i} \\ 0 \end{bmatrix} = \frac{1}{\sqrt{2}}\left(B_x^{\text{rec}} - \mathrm{i}B_y^{\text{rec}}\right). \tag{3.48}$$

It is convenient if this expression is an exponential function. Then the real part of only an exponential function needs to be found. Therefore write $B_x^{\text{rec}} = B_\perp \cos(\theta_B)$ and $B_y^{\text{rec}} = B_\perp \sin(\theta_B)$ since then

$$\mathbf{w}^T\mathbf{q}_1 = \frac{1}{\sqrt{2}} B_\perp e^{-\mathrm{i}\theta_B} \tag{3.49}$$

and thus

$$\mathbf{w}^T \partial_t \mathbf{m}(t) = -\omega_0 e^{-t/T_2}\left|M_+^0\right| B_\perp \sin\left(\omega_0 t - \varphi_0 + \theta_B\right). \tag{3.50}$$

The electromotive force is now the integral over all points in the domain $\mathbb{D}$

$$\begin{aligned} \mathscr{E}(t) &= -\int_{\mathbf{r}\in\mathbb{D}} \mathbf{w}^T \partial_t \mathbf{m}(t)\, dV \\ &= \int_{\mathbf{r}\in\mathbb{D}} \omega_0(\mathbf{r}) e^{-t/T_2(\mathbf{r})}\left|M_+^0(\mathbf{r})\right| B_\perp(\mathbf{r}) \sin\left(\omega_0(\mathbf{r})\, t - \varphi_0(\mathbf{r}) + \theta_B(\mathbf{r})\right) dV. \end{aligned} \tag{3.51}$$

Note that this equation is similar to Equation (2.12) which is used for the normal MRI scanners. For notational convenience, assume that the sample is homogeneous with volume V_s. The dependence on the location is also dropped for notational convenience. Then

$$\mathscr{E}(t) = \omega_0 e^{-t/T_2} \left|M_+^0\right| B_\perp \sin\left(\omega_0 t - \varphi_0 + \theta_B\right) V_s. \tag{3.52}$$

Before imaging takes place, the electromotive force is processed by modulation (low-noise amplification) and demodulation.
The low-noise amplification is done by multiplying the expression for the electromotive force by a factor $C > 0$

$$S_a(t) = C\mathscr{E}(t) = C\omega_0 e^{-t/T_2} \left|M_+^0\right| B_\perp V_s \sin\left(\omega_0 t + \zeta\right), \quad \text{where } \zeta = \theta_B - \varphi_0, \quad t > 0. \tag{3.53}$$

The low-noise amplified signal $S_a(t)$ is demodulated in the next equation. This is done by multiplying $S_a(t)$ by $-\mathrm{i}e^{\mathrm{i}\Omega t}$, where $\Omega = \omega_0 + \delta\omega$ and $\delta\omega$ is called the frequency offset, and results in

$$\begin{aligned} S_{demod}(t) &= -\mathrm{i}e^{\mathrm{i}\Omega t} s_a(t) \\ &= -\mathrm{i}\omega_0 C e^{-t/T_2} \left|M_+^0\right| B_\perp V_s \left(\frac{1}{2\mathrm{i}}\left(e^{\mathrm{i}(\omega_0 t+\zeta)} - e^{-\mathrm{i}(\omega_0 t+\zeta)}\right)\right) e^{\mathrm{i}t(\omega_0+\delta\omega)} \\ &= -\mathrm{i}\omega_0 C e^{-t/T_2} \left|M_+^0\right| B_\perp V_s \left(\frac{1}{2\mathrm{i}}\left(e^{\mathrm{i}(2\omega_0 t+\delta\omega t+\zeta)} - e^{\mathrm{i}(\delta\omega t+\zeta)}\right)\right). \end{aligned} \tag{3.54}$$

The high frequency component at $2\omega_0$ is filtered out, which results in the signal used for imaging as

$$S(t) = \frac{1}{2}\omega_0 C e^{-t/T_2} \left|M_+^0\right| B_\perp V_s e^{\mathrm{i}\zeta} e^{\mathrm{i}(\Omega-\omega_0)t}. \tag{3.55}$$

Remember that $\Delta B_x = \Delta B_y = 0$, so that $\omega_0 = \gamma B_0 + \gamma \Delta B_z$. With $\Omega = \gamma B_0$, we obtain

$$S(t) = \frac{1}{2}\omega_0 C e^{-t/T_2} \left|M_+^0\right| B_\perp V_s e^{\mathrm{i}\zeta} e^{-\mathrm{i}\gamma\Delta B_z t}. \tag{3.56}$$

Taking away the assumption of a homogeneous sample, we have the actual signal as

$$S(t) = \int_{\mathbf{r}\in\mathbb{D}} \frac{1}{2} C\omega_0(\mathbf{r}) e^{-t/T_2(\mathbf{r})} \left|M_+^0(\mathbf{r})\right| B_\perp(\mathbf{r}) e^{\mathrm{i}\zeta(\mathbf{r})} e^{-\mathrm{i}\gamma\Delta B_z t} d\mathbf{r}. \tag{3.57}$$

This equation is similar to Equation (2.14). However, in this derivation several assumptions have been made. If this had not been the case this could result in a far more complicated expression for the signal that is not as similar. Note that an RF pulse is needed to be able to receive this signal.

3.4. Measurement model

The signal was found to be

$$S(t) = \int_{\mathbf{r}\in\mathbb{D}} \frac{1}{2} C\omega_0(\mathbf{r}) e^{-t/T_2(\mathbf{r})} \left|M_+^0(\mathbf{r})\right| B_\perp(\mathbf{r}) e^{\mathrm{i}\zeta(\mathbf{r})} e^{-\mathrm{i}\gamma\Delta B_z t} d\mathbf{r} \tag{3.58}$$

where $\Delta B_z(\mathbf{r})$ is the perturbation in the z direction. Remember $\left|M_0^+\right| = \left|M_x^0 + \mathrm{i}M_y^0\right|$, where M_k^0 is the magnetisation vector in the k direction at time $t = 0$. Also $B_\perp$ originates from: $B_x^{\text{rec}} = B_\perp \cos(\theta_B)$ and $B_y^{\text{rec}} = B_\perp \sin(\theta_B)$.

Let $c(\mathbf{r})$ denote the sensitivity (response pattern) of the coil [10]. This yields the following general forward model for the MRI signal

$$S(t) = \int_{\mathbf{r}\in\mathbb{D}} c(\mathbf{r})\omega_0(\mathbf{r}) f(\mathbf{r}) e^{-t/T_2(\mathbf{r})} e^{-\mathrm{i}\phi(\mathbf{r},t)} d\mathbf{r} \tag{3.59}$$

where the space- and time-varying phase is

$$\phi(\mathbf{r}, t) = \gamma \Delta B_z(\mathbf{r})\, t \tag{3.60}$$

and $f(\mathbf{r})$ the desired image. For simplicity the focus lies on the case where the object is static so that $f(\mathbf{r})$ is not a function of time t. Then the desired image is defined as

$$f(\mathbf{r}) = \frac{1}{2} C \left|M_+^0(\mathbf{r})\right| B_\perp(\mathbf{r}) e^{\mathrm{i}\zeta(\mathbf{r})}. \tag{3.61}$$

The recorded measurements in an MRI scan consist of noisy samples of the MRI signal Equation (3.59)

$$y_i = S(t_i) + n_i, \quad i = 1, ..., N \tag{3.62}$$

where y_i denotes the i-th sample of the signal at time t_i. The t_i values are equally spaced. The measurement errors n_i are modelled by complex, zero-mean, white gaussian noise.
Using the measurement model in Equation (3.62) and the signal model in Equation (3.59), the typical image reconstruction problem in MRI is to estimate the object $f(\mathbf{r})$ from the measurement vector $\mathbf{y} = (y_1, ..., y_N)^T$. This is an ill-posed problem because the given measurements $\mathbf{y}$ are discrete whereas the object $f(\mathbf{r})$ is an unknown continuous-space function. We approximate $f(\mathbf{r})$ by writing it as a linear combination of basis functions

$$f(\mathbf{r}) = \sum_{j=1}^{n_p} f_j b(\mathbf{r} - \mathbf{r}_j) \tag{3.63}$$

where b denotes the object basis function, $\mathbf{r}_j$ denotes the center of the j-th translated basis function, and n_p the number of parameters. For simplicity, we use rectangular basis functions

$$b(\mathbf{r}) = \text{rect}(\mathbf{r}/\Delta) \tag{3.64}$$

i.e. square pixels of dimension Δ, so that n_p is the number of pixels, or voxels in 3D scans. Many other possible basis function choices can be considered, all of which are imperfect because the true object never satisfies the parametric model in Equation (3.63) [27].

Substituting the expansion in Equation (3.63) into the signal model in Equation (3.59) and simplifying leads to the discrete forward model

$$s(t_i) = \sum_{j=1}^{n_p} a_{ij} f_j \tag{3.65}$$

where the elements $\{a_{ij}\}$ of the matrix A are given by

$$a_{ij} = \int b(\mathbf{r} - \mathbf{r}_j) c(\mathbf{r}) \omega_0(\mathbf{r}) e^{-t_i/T_2(\mathbf{r})} e^{-\mathrm{i}\phi(\mathbf{r}, t_i)} d\mathbf{r}. \tag{3.66}$$

As the basis functions are usually highly localized (e.g. pixels/voxels), a 'center of pixel' approximation is used. This implies

$$a_{ij} = c(\mathbf{r}_j) \omega_0(\mathbf{r}_j) e^{-t_i/T_2(\mathbf{r}_j)} e^{-\mathrm{i}\phi(\mathbf{r}_j, t_i)}, \quad \phi(\mathbf{r}_j, t_i) = \gamma \Delta B_z(\mathbf{r}_j) t_i. \tag{3.67}$$

Combining Equations (3.62), (3.65) and (3.67) in matrix-vector form yields

$$\mathbf{y} = A\mathbf{f} + \mathbf{n} \tag{3.68}$$

where $\mathbf{f} = (f_1, ..., f_{n_p})$ is the vector of parameters (pixel values) that we wish to estimate from the data $\mathbf{y}$.

If rotation is used as an encoding method, an extra step has to be taken. After rotating the magnet to the wanted position, the magnetic field changes relative to the image/patient and hence matrix A is different for every (unique) rotation. Rotating the magnet therefore adds equations to the system in Equation (3.68). Let n_r be the number of rotations, then Equation (3.68) becomes

$$\begin{bmatrix} \mathbf{y}_1 \\ \vdots \\ \mathbf{y}_{n_r} \end{bmatrix} = \begin{bmatrix} A_1 \\ \vdots \\ A_{n_r} \end{bmatrix} \mathbf{f} + \begin{bmatrix} \mathbf{n}_1 \\ \vdots \\ \mathbf{n}_{n_r} \end{bmatrix} \tag{3.69}$$

or $\mathbf{y} = A\mathbf{f} + \mathbf{n}$ where $\mathbf{y} \in \mathbb{C}^{Nn_r \times 1}$, $A \in \mathbb{C}^{Nn_r \times n_p}$, $\mathbf{f} \in \mathbb{C}^{n_p \times 1}$ and $\mathbf{n} \in \mathbb{C}^{Nn_r \times 1}$. When the matrix A is found and the signal data $\mathbf{y}$ is given, the next step is to recover $\mathbf{f}$ from the system of equations, but first some theory is given about T_2 relaxation.

3.5. T_2 and T_2^* relaxation

In theory, the signal expression in equation (2.14) looks fine. However, in reality T_2-weighted imaging needs a homogeneous field. As this is not the case, the so called T_2^* plays a big role.

In Equation (2.7), T_2 is briefly introduced together with T_1 as the characterisation of the relaxation process of a spin system. The mentioned echo signal and the acquisition methods are closely related to the relaxation times. Therefore it is necessary to take a look at the spin echo, the multiple spin echo or turbo spin echo (TSE) and gradient echo (GRE).

3.5.1. Gradient echo and spin echo pulse sequence

A single RF pulse generates the FID signal, as mentioned in Section 2.3. This single pulse is used in gradient echo (GRE) sequences. When two successive pulses are generated it produces a *spin echo* [5].

The spin echo pulse sequence is composed of a 90° radiofrequency pulse, a 180° pulse and an echo signal. It is depicted in Figure 3.8a. The time between the middle of the first pulse (90°) and the peak of the spin echo is called the *echo time (TE)*. The time at which the pulse sequence repeats is called the *repetition time (TR)*. The 180° pulse is usually applied at $\frac{1}{2}TE$ which is the same as τ.

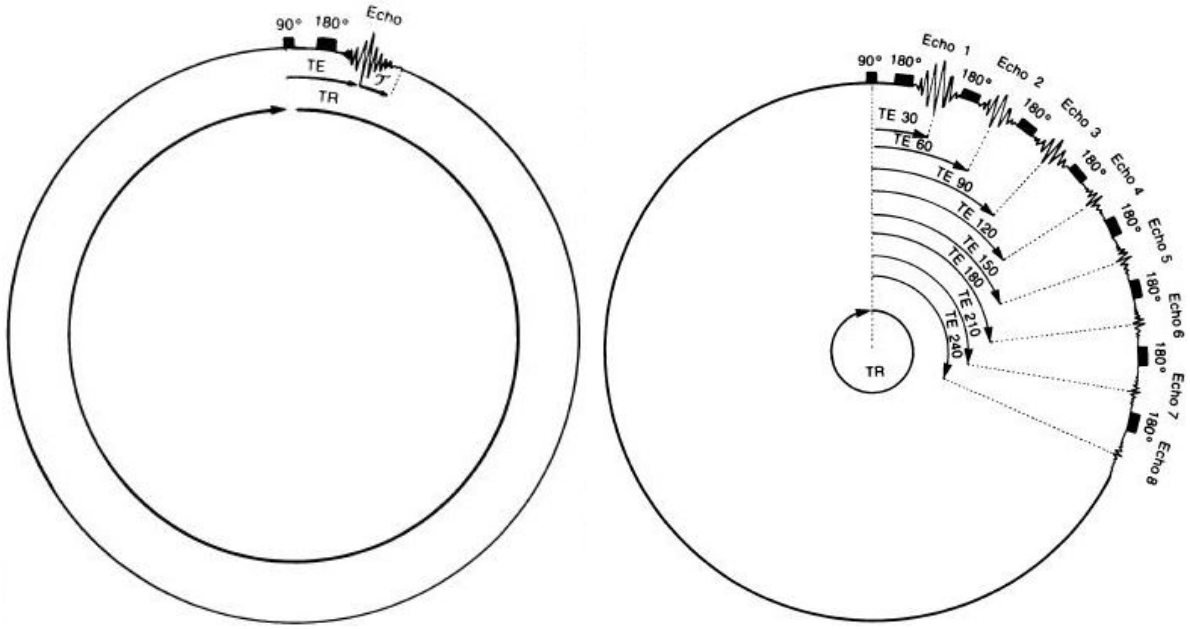

(a) Spin echo pulse sequence.

(b) Multiple spin echo pulse sequence.

Figure 3.8: Illustrative examples of a (multiple) spin echo pulse sequence [15].

During the FID decay (after the 90° pulse), spin phase information is lost because the phases have been scattered by field inhomogeneities and external constant field distortions. The spin echo represents the regeneration of that information: the 180° pulse refocusses the out-of-phase spins.

The pulse does not correct for T_1 or T_2 effects. This is due to random processes at the atomic/molecular level. So when the spins are exposed to something of, for example, iron or to inhomogeneities in the main magnetic field, the 180° pulse will correct this. However, phase shifts due to movement, flow or chemical exchanges are not corrected for [5].

3.5.2. Multiple spin echo pulse sequence

The multiple spin echo pulse sequence is similar to the spin echo pulse sequence except that there is no limitation to a single echo signal (therefore the word 'multiple'). Therefore it consists of a 90° pulse and multiple

180° pulses which are all followed by an echo.The effective echo time is now the time from the initiating 90° pulse until the peak of the last echo.

Again this is depicted in Figure 3.8b. Here, for example, the effective echo time is 'TE 240'.

3.5.3. Relation T_2 and T_2^*

Transverse magnetisation is formed by tilting the longitudinal magnetisation into the transverse plane using a radiofrequency (RF) pulse. The magnetisation then rotates at Larmor frequency and produces a signal [8]. Immediately after the RF pulse is switched off, the protons are in phase but soon go out of phase again as soon as the magnitude of the transverse magnetisation decreases. Protons precess with a frequency which is determined by the magnetic field strength they are in. As the field is not homogeneous the precession frequencies differ. Also, each proton is influenced by the small magnetic fields from neighbouring nuclei. These internal magnetic field variations are characteristic for a tissue. When the transversal magnetisation is plotted versus time, the curve decays to 0: the spins go back to their original state. The time constant describing how fast the transversal magnetisation vanishes is called the transversal relaxation time T_2.

The amount of T_2 decay a tissue experiences depends on multiple factors as explained above. Each tissue has an inherent T_2 value, but external factors (such as magnetic field inhomogeneity) can influence the T_2 relaxation time. This additional effect is captured in T_2^*. The 180° pulse(s) in spin-echo sequences help(s) to eliminate the dephasing effects on the T_2 relaxation time. This results in T_2 weighted images rather than T_2^* weighted images [20].

Therefore, in gradient echo sequences, the transverse relaxation (T_2^*) is a combination of the 'true' T_2 relaxation (which depends on the tissue) and the relaxation caused by magnetic field inhomogeneities.

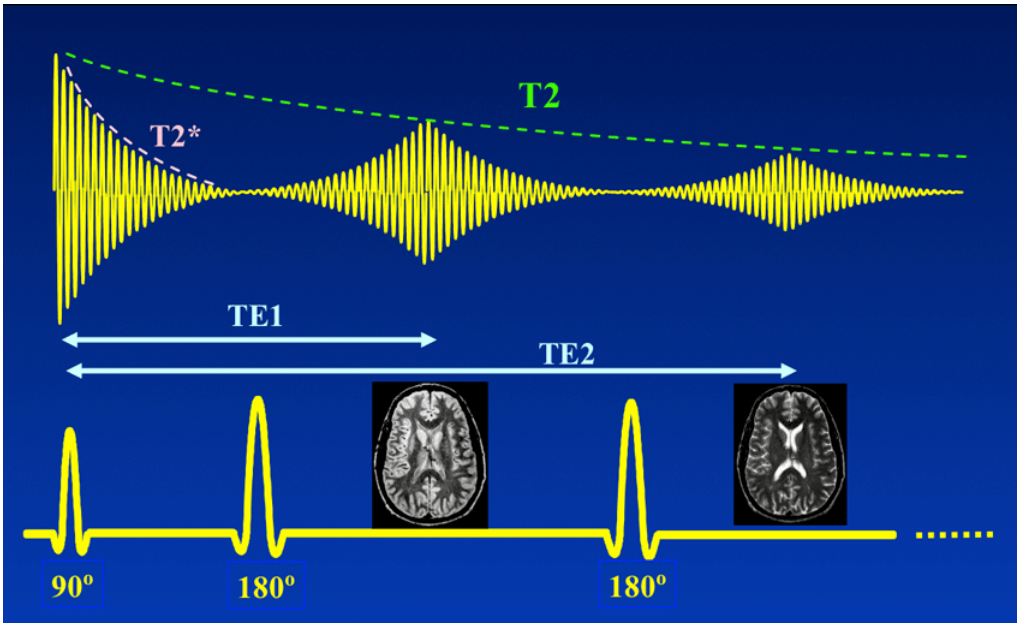

Figure 3.9: Illustration of the effect of T_2 and T_2^* in a multiple spin echo sequence (see *http://mri-q.com/se-vs-multi-se-vs-fse.html*).

Figure 3.9 summarises the above findings:

- The T_2^* decay can be found in the signal after the 90° pulse, before additional pulses are sent out.
- The 180° pulses do not correct for the T_2 relaxation. This means that the additional pulses can give information as long as the T_2 relaxation has not completely destroyed the signal. The more 180° pulses are added, the lower the amplitude of the echo signal due to T_2 decay.
- T_2^* weighted images occur with GRE sequences.
- T_2 weighted images occur with single/multiple spin echo pulse sequences.

Next it is important to remember the goal of the low-cost, portable MRI. It should not cost too much energy as well as that the multiple spin echo is not preferred in the imaging of the head. Therefore T_2 weighted imaging might not be the right option in the end. Note it is still considered because the implementation is simpler. That brings us back to the T_2^* weighted imaging. Which essentially also makes sense because of the extremely inhomogeneous field of the main magnet.

For finding an expression for T_2^*, remember that

the transverse relaxation (T_2^*) is a combination of the 'true' T_2 relaxation (which depends on the tissue) and the relaxation caused by magnetic field inhomogeneities.

In terms of equations this translates to

$$\frac{1}{T_2^*} = \frac{1}{T_2} + \frac{1}{T_2'}. \tag{3.70}$$

From this point on, literature jumps straight to the fact that

$$\frac{1}{T_2'} = \gamma \Delta B_{\text{inhom}} \tag{3.71}$$

and ΔB_{inhom} the magnetic field inhomogeneity across a voxel [6]. Mitchell and Cohen have tried to describe why equality in Equation (3.71) holds in [6] and is explained next.

Assume an object has a Lorentzian spin density

$$\rho(x) = N_0 \frac{2b}{b^2 + 4\pi^2 x^2}, \quad b = 2\pi\Delta x \tag{3.72}$$

where $2\Delta x$ is the FWHM (full width at half maximum) of the distribution and N_0 the total number of spins. This means the object has a spatially smeared spin density, with most of the spins being contained within a voxel of size Δx. Assuming a background gradient G_x' exists over all space, the signal is

$$\tilde{\rho}(T_E) = \int_{-\infty}^{\infty} \rho(x) e^{-i\gamma G_x' x T_E} dx. \tag{3.73}$$

The right hand side is a Fourier integral for ρ in Equation (3.72). Estimating this Fourier integral gives

$$\tilde{\rho}(T_E) = N_0 e^{-T_E/T_2'}, \quad \text{where } T_2' = 1/\left(\gamma b \left|G_x'\right|/2\pi\right). \tag{3.74}$$

In terms of an average field inhomogeneity ΔB_{inhom} defined by the inhomogeneity across a voxel,

$$\Delta B_{\text{inhom}} \equiv G_x' \Delta x = b G_x'/2\pi \tag{3.75}$$

the expression for T_2' is $T_2' = 1/\left(\gamma |\Delta B_{\text{inhom}}|\right)$. This leads to

$$\frac{1}{T_2^*} = \frac{1}{T_2} + \gamma |\Delta B_{\text{inhom}}|. \tag{3.76}$$

Now observe an important fact about the information from the literature: it is assumed that Equation (3.71) holds for only the hypothetical case. There are many other assumptions: the object has a Lorentzian spin density and the background gradient exists over all space. The Fourier integral is estimated and the whole derivation is only valid for a gradient echo. Also the analysis of more realistic models showed that Equation (3.76) is actually

$$\frac{1}{T_2^*} = \frac{1}{T_2} + \kappa\gamma |\Delta B_{\text{inhom}}| \tag{3.77}$$

where κ is not necessarily 1. Also not all models lead to this exponential decay, but some have a Gaussian or other form of decay. κ depends on the field inhomogeneity and the form of the spin density function.

4

Numerical solvers and regularisation

Consider again the linear system

$$A\mathbf{x} = \mathbf{b}, \quad A \in \mathbb{C}^{m\times n}, \quad \mathbf{x} \in \mathbb{R}^n, \quad \mathbf{b} \in \mathbb{C}^m \tag{4.1}$$

and recall the following definitions

Definition 1. *A linear system is called underdetermined if the number of unknown variables exceeds the number of equations ($m < n$).*

Definition 2. *A system is called formally determined if the number of unknowns is the same as the number of equations ($m = n$).*

Definition 3. *A system is called overdetermined if there are more equations than unknowns ($m > n$)[7].*

The matrix A is not necessarily square. It is possible that such a system has zero, one or infinitely many solutions. A formally determined system has exactly one solution under the condition that matrix A is invertible. An underdetermined system has $n - m$ degrees of freedom; the unknowns that cannot be determined.

In order to solve the linear system $A\mathbf{x} = \mathbf{b}$ when A is not square, an equivalent system can be solved

$$A^* A\mathbf{x} = A^*\mathbf{b} \tag{4.2}$$

which is semi hermitian positive definite (semi HPD). This system is known as the system of the *normal equations* associated with the least-squares problem,

$$\text{minimize} \quad ||\mathbf{b} - A\mathbf{x}||_2. \tag{4.3}$$

Note that Equation (4.2) is typically used to solve least-squares problem in Equation (4.3) for *overdetermined* systems. The minimizer is called the *least squares solution* because it minimises the sum of the squares of the components of the residual error $\mathbf{r} = \mathbf{b} - A\mathbf{x}$. If $\text{rank}(A) = n$ then the least squares minimum norm (LSMN) solution is given by

$$\mathbf{x} = (A^* A)^{-1} A^*\mathbf{b}. \tag{4.4}$$

A similar well known alternative sets $\mathbf{x} = A^*\mathbf{u}$ and solves the equation

$$AA^*\mathbf{u} = \mathbf{b} \tag{4.5}$$

for $\mathbf{u}$. Once $\mathbf{u}$ is computed, the original unknown $\mathbf{x}$ is obtained by multiplying $\mathbf{u}$ by A^*.
With this method we minimise the norm of $\mathbf{x}$

$$\text{minimize} \quad ||\mathbf{x}||_2 \tag{4.6}$$

such that $A\mathbf{x} = \mathbf{b}$. The solution is then given by $\mathbf{x} = A^*\mathbf{u}$ with $AA^*\mathbf{u} = \mathbf{b}$. So if rank$(A) = m$ then the minimum norm solution is given by

$$\mathbf{x} = A^*(AA^*)^{-1}\mathbf{b}. \tag{4.7}$$

Note that for this formulation we assume that $A\mathbf{x} = \mathbf{b}$ is consistent and hence has a solution.
The system in Equation (4.2) and methods derived from it are often labeled with NR (N for 'Normal'and R for 'Residual') while the system in Equation (4.5) and derived methods are labeled with NE (N for 'Normal' and E for 'Error')[22].

4.1. Singular Value Decomposition and pseudoinverse

The choice of the best algorithm for solving such equations depend on several factors. In the first phase, naive solving methods have been used. One is called the pseudoinverse. A pseudoinverse is a matrix inverse-like object that may be defined for any complex matrix, even if it is not square. The most used pseudoinverse is the Moore-Penrose inverse [2].

Penrose showed that, for every finite matrix A (square or rectangular) of real or complex elements, there is a unique matrix X satisfying the equations

$$AXA = A, \tag{4.8}$$
$$XAX = X, \tag{4.9}$$
$$(AX)^* = AX, \tag{4.10}$$
$$(XA)^* = XA, \tag{4.11}$$

where A^* denotes the conjugate transpose of A. Recall that the singular value decomposition (SVD) of matrix A can be written as

$$A = UWV^* \tag{4.12}$$

with

- U $(m \times m)$- the columns of U are the eigenvectors of AA^*. The columns are orthogonal if they are real or unitary of they are complex.
- W $(m \times n)$- the singular values of A lie on the diagonal and are the square root of the eigenvalues of AA^* and A^*A.
$$W = \begin{bmatrix} W_r & 0 \\ 0 & 0 \end{bmatrix}, \quad W_r = \text{diag}(\sigma_1, \sigma_2, ..., \sigma_r) \tag{4.13}$$
- V $(n \times n)$- the columns of V are eigenvectors of A^*A. The columns are orthogonal if they are real or unitary of they are complex.

If matrix A has the singular value decomposition $A = UWV^*$ then the Moore-Penrose inverse of A is

$$A^+ = V^*W^+U \tag{4.14}$$

and $x = A^+b$ is corresponding least-squares minimimum norm solution. Note that W^+ is the pseudoinverse of W

$$W^+ = \begin{bmatrix} W_r^+ & 0 \\ 0 & 0 \end{bmatrix}, \quad W_r^+ = \text{diag}(1/\sigma_1, 1/\sigma_2, ..., 1/\sigma_r). \tag{4.15}$$

If A has $m > n$ and has full column rank (n) then

$$A^+ = (A^*A)^{-1}A^* \tag{4.16}$$

giving the least-squares minimum norm solution $\mathbf{x} = A^+\mathbf{b}$. If A has $m < n$ and has full row rank (m) then

$$A^+ = A^*(AA^*)^{-1} \tag{4.17}$$

giving the least norm solution $\mathbf{x}^+ = A^+\mathbf{b}$.

4.1.1. Error analysis

The error analysis below can also be found in [25]. Let $\mathbf{x}^+$ be the solution of the least squares problem, using the SVD method with r singular values. Then the vector $\mathbf{b}$ of the least squares solution

$$\begin{aligned}\mathbf{x}^+ &= A^+\mathbf{b} = VW^+U^*\mathbf{b} \\ &= \sum_{i=1}^{r} \frac{\mathbf{u}_i^*\mathbf{b}}{\sigma_i}\mathbf{v}_i\end{aligned} \tag{4.18}$$

can be with or without noise. Note that $\mathbf{v}_i$ is the i^{th} column of V, $\mathbf{u}_i$ the i^{th} column of U and σ_i the singular value of the ith column of W. Let $V^*\mathbf{x}_{\text{model}} = \alpha$, then

$$\mathbf{b}_{\text{model}} = A\mathbf{x}_{\text{model}} = UWV^*\mathbf{x}_{\text{model}} = UW\alpha. \tag{4.19}$$

If $v_i^*\mathbf{x} = \alpha_i \in \mathbb{R}$, $\mathbf{b}$ can be rewritten as

$$\mathbf{b} = \sum_{i=1}^{m} \sigma_i\alpha_i\mathbf{u}_i = \sum_{i=1}^{r} \sigma_i\alpha_i\mathbf{u}_i. \tag{4.20}$$

Note that the last equality holds as we have r singular values; columns i to m are zero vectors and therefore give zero contribution in the sum.

When $\mathbf{b}$ contains noise a noise vector $\mathbf{n}$ given by

$$\sum_{i=1}^{m} \left(\mathbf{u}_i^*\mathbf{n}\right)\mathbf{u}_i \tag{4.21}$$

is added to $\mathbf{b}$.
Now perturbed vector $\hat{\mathbf{b}}$ can be written as

$$\begin{aligned}\hat{\mathbf{b}} &= \sum_{i=1}^{r} \sigma_i\alpha_i\mathbf{u}_i + \sum_{i=1}^{m} \left(\mathbf{u}_i^*\mathbf{n}\right)\mathbf{u}_i \\ &= \sum_{i=1}^{r} \left(\sigma_i\alpha_i + \mathbf{u}_i^*\mathbf{n}\right)\mathbf{u}_i + \sum_{i=r+1}^{m} \left(\mathbf{u}_i^*\mathbf{n}\right)\mathbf{u}_i\end{aligned} \tag{4.22}$$

and the corresponding solution $\mathbf{x}^+$ as

$$\begin{aligned}\mathbf{x}^+ &= VW^+U^*\hat{\mathbf{b}} \\ &= VW^+U^*\left(\sum_{i=1}^{r} \left(\sigma_i\alpha_i + \mathbf{u}_i^*\mathbf{n}\right)\mathbf{u}_i + \sum_{i=r+1}^{m} \left(\mathbf{u}_i^*\mathbf{n}\right)\mathbf{u}_i\right) \\ &= \sum_{i=1}^{r} \frac{\sigma_i\alpha_i + \mathbf{u}_i^*\mathbf{n}}{\sigma_i}\mathbf{v}_i.\end{aligned} \tag{4.23}$$

Using the fact that U is orthogonal and $\sigma_i^+ = 0$ for $i > r$. Also as $\alpha_i\mathbf{v}_i = \mathbf{v}_i\alpha_i = \mathbf{v}_i\mathbf{v}_i^*\mathbf{x}_{\text{model}}$ it follows that $\sum_{i=1}^{m} \alpha_i\mathbf{v}_i = \mathbf{x}_{\text{model}}$. This results in

$$\mathbf{x}^+ = \mathbf{x}_{\text{model}} + \sum_{i=1}^{r} \frac{\mathbf{u}_i^*\mathbf{n}}{\sigma_i}\mathbf{v}_i + \sum_{i=r+1}^{n} \alpha_i\mathbf{v}_i. \tag{4.24}$$

Bringing the model solution to the left hand side and taking the norm determines the global error

$$\begin{aligned}\left|\left|\mathbf{x}^+ - \mathbf{x}_{\text{model}}\right|\right| &= \left|\left|\sum_{i=1}^{r} \frac{\mathbf{u}_i^*\mathbf{n}}{\sigma_i}\mathbf{v}_i + \sum_{i=r+1}^{n} \alpha_i\mathbf{v}_i\right|\right| \\ &= \sqrt{\sum_{i=1}^{r} \left(\frac{\mathbf{u}_i^*\mathbf{n}}{\sigma_i}\right)^2 + \sum_{i=r+1}^{n} \alpha_i^2}.\end{aligned} \tag{4.25}$$

So when the singular values σ_i are very small, the global error grows very large. To avoid this the singular values close to zero should be ignored. Note that when there is no noise $\mathbf{n} = \mathbf{0}$ the solution still differs from

the pseudo inverse solution. This is because of limited machine precision. When singular values are not too small, this noise term can be neglected.
In conclusion, the best-approximate solution can be computed relatively easy when the singular value decomposition of A is known. However the numerical computation of the singular value decomposition becomes unreliable for large, noisy systems. Therefore we resort to other solvers: iterative solvers.

4.2. (Krylov-subspace) iterative methods

An iterative solver is a procedure that generates a sequence of improving approximate solution vectors $(\mathbf{x}_k)_{k=0}^{\infty}$, starting at some initial guess $\mathbf{x}_0$. The iteration stops when a stopping criterion has been satisfied or, if it is given, a maximum number of iterations is reached. If the problem is consistent, a typical stopping criterion is based on the residual norm

$$\|\mathbf{r}_k\|_2^2 = \|\mathbf{b} - A\mathbf{x}_k\|_2^2. \tag{4.26}$$

When it is reduced below a tolerance level, then the iterative solver is stopped (for least squares problems, the residual norm does not converge to zero).

Consider the following definition

Definition 4. *Given a matrix $A \in \mathbb{R}^{n\times n}$ and a vector $\mathbf{r}_0 \in \mathbb{R}^n$ the Krylov subspace $K^k(A;\mathbf{r}_0)$ is*

$$K^k(A;\mathbf{r}_0) = \text{span}\left\{\mathbf{r}_0, A\mathbf{r}_0, ..., A^{i-1}\mathbf{r}_0\right\}. \tag{4.27}$$

The subspace $K^k(A;\mathbf{r}_0) = \text{span}\left\{\mathbf{r}_0, A\mathbf{r}_0, ..., A^{i-1}\mathbf{r}_0\right\}$ is called the Krylov-space of dimension k corresponding to matrix A and initial residual $\mathbf{r}_0$. It is the subspace spanned by the product of the first $k-1$ powers of A and $\mathbf{r}_0$. Observe that the true solution $\mathbf{x}_* = A^{-1}\mathbf{r}_0 \in K^k(A,\mathbf{r}_0)$ and for natural numbers p and q with $p \le q$ holds that $K^p(A,\mathbf{r}_0) \subseteq K^q(A,\mathbf{r}_0)$.

One of the first Krylov-subspace methods is the so-called *Conjugate Gradient Method* (CG). It is the best iterative method to solve the linear system $A\mathbf{x} = \mathbf{b}$ with A a symmetric positive definite matrix. It finds a solution in the Krylov subspace $\mathbf{x}_k \in \text{span}\{\mathbf{b}, A\mathbf{b}, A^2\mathbf{b}, \cdots, A^k\mathbf{b}\}$ that minimizes $(\mathbf{x}-\mathbf{x}_k)^T A(\mathbf{x}-\mathbf{x}_k)$. So CG is an orthogonal projection method that satisfies a minimality condition. The error has to be minimal in the A-norm (or energy norm) which is defined as

$$\|\mathbf{x}_* - \mathbf{x}\|_A = \|\mathbf{e}\|_A = \sqrt{\mathbf{e}^T A\mathbf{e}} = \sqrt{\langle \mathbf{e}, A\mathbf{e}, \rangle} \tag{4.28}$$

where $\mathbf{x}_*$ is the true solution.

Algorithm 1 Conjugate Gradient method form

procedure CG($A \in \mathbb{R}^{n\times n}, \mathbf{b}$) ▷ Solve $A\mathbf{x} = \mathbf{b}$
Initialize
  $\mathbf{r}_0 = \mathbf{b} - A\mathbf{x}_0$;
  $\mathbf{p}_0 = \mathbf{r}_0$
  for $k = 1, 2, ...$ **do** ▷ until stopping criterion is satisfied
    Compute α_{k-1};
    $\mathbf{x}_k = \mathbf{x}_{k-1} + \alpha_{k-1}\mathbf{p}_{k-1}$;
    $\mathbf{r}_k = \mathbf{r}_{k-1} - \alpha_{k-1}A\mathbf{p}_{k-1}$;
    $\mathbf{r}_k = A^T\mathbf{r}_k$;
    Compute β_{k-1};
    $\mathbf{p}_k = \mathbf{r}_k + \beta_{k-1}\mathbf{p}_{k-1}$;
  end for
end procedure

For CG the standard expressions for α_k and β_k are

$$\alpha_k = \frac{\langle \mathbf{r}_k, \mathbf{r}_k\rangle}{\langle \mathbf{p}_k, A\mathbf{p}_k\rangle}, \quad \beta_k = \frac{\langle \mathbf{r}_{k+1}, \mathbf{r}_{k+1}\rangle}{\langle \mathbf{r}_k, \mathbf{r}_k\rangle}. \tag{4.29}$$

When working with a system in which A is not SPD, one of the variants of CG can be used: A^*A is semi-HPD (hermitian positive definite). The then so called Normal Equations can be solved. There are several CG methods for the Normal Equations and they all minimize different errors, for example the true error $\mathbf{e}_k = \mathbf{x} - \mathbf{x}_k$ and the residual $\mathbf{r}_k = \mathbf{b} - A\mathbf{x}_k$. CGNE denotes the Conjugate Gradient method applied to the system in Equation (4.5) and minimizes the true error $\mathbf{e}_k$ (only for consistent problems). CGLS (or CGNR) is the Conjugate Gradient method applied to the system in Equation (4.2) and minimises the residual $\mathbf{r}_k$.
No further introduction or derivation of the CG method will be presented. For more details about this algorithm, the reader is referred to [22].

4.2.1. Conjugate Gradient Least Squares (CGLS)

Consider the non-square system $A\mathbf{x} = \mathbf{b}$. The CG method was extended to cover a larger class of matrices, of which the CGLS method is one. The Conjugate Gradient method for Least Squares is mathematically equivalent to applying CG to normal equations

$$A^*A\mathbf{x} = A^*\mathbf{b}. \tag{4.30}$$

CGLS solves the problem without actually forming the expensive product A^*A. The matrix A does not have to be square.

As mentioned before, CGLS minimises the residual $\mathbf{r}_k$. This can be shown with the energy norm using equation (4.30):

$$\begin{aligned} \|\mathbf{x}_* - \mathbf{x}_k\|^2_{A^*A} &= \langle (\mathbf{x}_* - \mathbf{x}_k), A^*A(\mathbf{x}_* - \mathbf{x}_k)\rangle \\ &= \langle A(\mathbf{x}_* - \mathbf{x}_k), A(\mathbf{x}_* - \mathbf{x}_k)\rangle \\ &= \langle \mathbf{b} - A\mathbf{x}_k, \mathbf{b} - A\mathbf{x}_k\rangle \\ &= \|\mathbf{b} - A\mathbf{x}_k\|_2^2 = \|\mathbf{r}_k\|_2^2. \end{aligned} \tag{4.31}$$

So the k-th iterate of the CGLS method solves the minimisation problem

$$\mathbf{x}_k = \arg \min_{\mathbf{x}_k \in K^k(A^*A, A^*\mathbf{b})} \|\mathbf{b} - A\mathbf{x}\|_2^2 \tag{4.32}$$

which is the minimisation of the residual norm.

For CGLS the standard expressions for α_k and β_k are

$$\alpha_k = \frac{\langle \mathbf{s}_k, \mathbf{s}_k\rangle}{\langle A\mathbf{p}_k, A\mathbf{p}_k\rangle}, \quad \beta_k = \frac{\langle \mathbf{s}_{k+1}, \mathbf{s}_{k+1}\rangle}{\langle \mathbf{s}_k, \mathbf{s}_k\rangle}, \quad \text{with } \mathbf{s}_k = A^*(\mathbf{b} - A\mathbf{x}_k) \tag{4.33}$$

which results in the following algorithm:

Algorithm 2 Conjugated Gradient Least Squares Algorithm [3]

procedure CGLS($\mathbf{A}, \mathbf{b}$) ▷ Solve $\mathbf{Ax} = \mathbf{b}$
Initialize
  $\mathbf{r}_0 = \mathbf{b} - \mathbf{Ax}_0$;
  $\mathbf{s}_0 = \mathbf{A}^*\mathbf{r}_0$;
  $\mathbf{p}_0 = \mathbf{s}_0$;
  for $k = 1, 2, \ldots$ **do** ▷ until stopping criterion is satisfied
    $\alpha_{k-1} = \frac{\langle \mathbf{s}_{k-1}, \mathbf{s}_{k-1}\rangle}{\langle A\mathbf{p}_{k-1}, A\mathbf{p}_{k-1}\rangle}$
    $\mathbf{x}_k = \mathbf{x}_{k-1} + \alpha_{k-1}\mathbf{p}_{k-1}$;
    $\mathbf{r}_k = \mathbf{r}_{k-1} - \alpha_{k-1}A\mathbf{p}_{k-1}$;
    $\mathbf{s}_k = \mathbf{A}^*\mathbf{r}_k$;
    $\beta_{k-1} = \frac{\langle \mathbf{s}_k, \mathbf{s}_k\rangle}{\langle \mathbf{s}_{k-1}, \mathbf{s}_{k-1}\rangle}$;
    $\mathbf{p}_k = \mathbf{s}_k + \beta_{k-1}\mathbf{p}_{k-1}$;
  end for
end procedure

Note that if $\mathbf{x}_0 = 0$, then all update vectors $\mathbf{p}_k$ are in the rowspace of A by construction. This means that the solution vector $\mathbf{x}_k$ is in the rowspace. Consequently CGLS converges to the least squares minimum norm solution if $\mathbf{x}_0 = 0$.

4.2.2. Conjugate Gradient Normal Error (CGNE)

When CG is applied to the normal equations

$$AA^*\mathbf{u} = \mathbf{b} \tag{4.34}$$

with $A^*\mathbf{u} = \mathbf{x}$ an error-minimising method results. This method is called the Conjugated Gradient Normal Error method (CGNE).
This fact that it is error-minimising can be shown with the energy norm using equation (4.34).

$$\begin{aligned} \|\mathbf{u}_* - \mathbf{u}_k\|^2_{AA^*} &= \langle (\mathbf{u}_* - \mathbf{u}_k), AA^*(\mathbf{u}_* - \mathbf{u}_k)\rangle \\ &= \langle A^*(\mathbf{u}_* - \mathbf{u}_k), A^*(\mathbf{u}_* - \mathbf{u}_k)\rangle \\ &= \langle \mathbf{x}_* - \mathbf{x}_k, \mathbf{x}_* - \mathbf{x}_k\rangle \\ &= \|\mathbf{x}_* - \mathbf{x}_k\|_2^2 = \|\mathbf{e}_k\|_2^2. \end{aligned} \tag{4.35}$$

So the k-th iterate of the CGNE method solves the minimisation problem

$$\mathbf{x}_k = \arg \min_{\mathbf{x}_k \in K^k(AA^*, \mathbf{b})} \|\mathbf{e}_k\|_2^2 \tag{4.36}$$

which is the minimisation of the true error.
For CGNE the standard expressions for α_k and β_k are

$$\alpha_k = \frac{\langle \mathbf{r}_k, \mathbf{r}_k\rangle}{\langle \mathbf{p}_k, \mathbf{p}_k\rangle}, \quad \beta_k = \frac{\langle \mathbf{r}_{k+1}, \mathbf{r}_{k+1}\rangle}{\langle \mathbf{r}_k, \mathbf{r}_k\rangle} \tag{4.37}$$

which results in the following algorithm:

Algorithm 3 Conjugated Gradient Normal Error Algorithm [22]

procedure CGNE($A, \mathbf{b}$) ▷ Solve $A\mathbf{x} = \mathbf{b}$
Initialize
  $\mathbf{r}_0 = \mathbf{b} - A\mathbf{x}_0$;
  $\mathbf{s}_0 = A^*\mathbf{r}_0$;
  $\mathbf{p}_0 = \mathbf{s}_0$;
  for $k = 1, 2, \ldots$ **do** ▷ until stopping criterion is satisfied
    $\alpha_{k-1} = \frac{\langle \mathbf{r}_{k-1}, \mathbf{r}_{k-1}\rangle}{\langle \mathbf{p}_{k-1}, \mathbf{p}_{k-1}\rangle}$
    $\mathbf{x}_k = \mathbf{x}_{k-1} + \alpha_{k-1}\mathbf{p}_{k-1}$;
    $\mathbf{r}_k = \mathbf{r}_{k-1} - \alpha_{k-1}A\mathbf{p}_{k-1}$;
    $\mathbf{s}_k = A^*\mathbf{r}_k$;
    $\beta_{k-1} = \frac{\langle \mathbf{r}_k, \mathbf{r}_k\rangle}{\langle \mathbf{r}_{k-1}, \mathbf{r}_{k-1}\rangle}$;
    $\mathbf{p}_k = \mathbf{s}_k + \beta_{k-1}\mathbf{p}_{k-1}$;
  end for
end procedure

In conclusion, CGLS finds vectors $\mathbf{x}_k$ in the Krylov space $K^k(A^*A, A^*\mathbf{b})$, whereas CGNE finds $\mathbf{u}_k$ in Krylov space $K^k(AA^*, \mathbf{b})$. However, since we have the relation $\mathbf{x}_k = A^*\mathbf{u}_k$, it can be concluded that the Krylov subspace for $\mathbf{u}_k$ is equal to $A^*K^k(AA^*, \mathbf{b}) = K^k(A^*A, A^*\mathbf{b})$.
Both methods, CGLS and CGNE, find approximations in the same subspace which satisfy a different optimality condition;

- CGLS: minimisation of residual $\mathbf{r}_k$,
- CGNE: minimisation of error $\mathbf{e}_k$.

4.2.3. p-norm minimisation

Before discussing the p-norm minimisation, recall the Hölder norm. In some applications it might be more adequate to minimize some other norm than the l_2 norm of the solution $\mathbf{x}$.

Definition 5. *The Hölder vector l_p-norms $||\cdot||_p$ are defined by*

$$\|\mathbf{x}\|_p = \left(\sum_{i=1}^{n} |x_i|^p \right)^{1/p}, \quad 1 \le p < \infty. \tag{4.38}$$

Remember, the Euclidian norm corresponds to $p = 2$. Now to illustrate the effect of a Hölder norm with $p \neq 2$, consider the problem of estimating a scalar γ from m observations $y \in \mathbb{R}^m$. This is equivalent to minimizing $||A\gamma - y||_p$. In this case A is equal to a vector with ones. Now let the observations $\mathbf{y}$ be ordered from largest to smallest, i.e. $y_1 \geq y_2 \geq \cdots \geq y_m$. Then the solutions for $p = 1, 2$ and the limiting case $p \to \infty$ are

$$\begin{aligned} \gamma_1 &= y_{m/2} \quad (m \text{ even}), \\ \gamma_2 &= (y_1 + \cdots + y_m)/m, \\ \gamma_\infty &= (y_1 + y_m)/2. \end{aligned} \tag{4.39}$$

Note that these solutions correspond to respectively the median, mean and midrange. Also, γ_1 is insensitive to extreme values of $\mathbf{y}$. This holds for this small problem but carries over to more general problems as well; a small number of isolated large errors is not likely to change the solution (using the 1-norm). However, for $p = 1$ the solution may not be unique, while for $1 < p < \infty$ there exists exactlyone l_p solution. Therefore it might be desirable to obtain the l_p solution for a noninteger value of p greater than but close to 1 [4].
The approximation problem that is then solved is

$$\psi(x) = \min \|x\|_p^p, \quad 1 < p < 2 \tag{4.40}$$

such that $A\mathbf{x} = \mathbf{b}$. Solving the l_p norm problem with $1 < p < 2$ as follows. The basic idea is reforming the minimisation problem as

$$\min_x \psi(x) \quad \text{s.t. } A\mathbf{x} = \mathbf{b} \tag{4.41}$$

with

$$\begin{aligned} \psi(x) &= \sum_{i=1}^{m} |x_i|^p \\ &= \sum_{i=1}^{m} |x_i|^{p-2} |x_i|^2. \end{aligned} \tag{4.42}$$

Assume that $|x_i| > 0$ for $i = 1, ..., m$ (so $x_i \neq 0$). Let D be a diagonal weight matrix with weights $|x_i|^{(p-2)/2}$ on the (i, i)-th position. Note that it depends on the unknown solution $\mathbf{x}$.

$$D = \text{diag}(|x_i|)^{(p-2)/2}. \tag{4.43}$$

The original problem is reduced to a least squares problem with weights. The minimisation problem can be written as

$$\min_{\mathbf{x}} \|D\mathbf{x}\|_2^2 \quad \text{s.t. } A\mathbf{x} = \mathbf{b} \tag{4.44}$$

which in turn can be solved using the fixed-point iteration

$$\min_{\mathbf{x}_k} \|D_{k-1}\mathbf{x}_k\|_2^2 \quad \text{s.t. } A\mathbf{x}_k = \mathbf{b}. \tag{4.45}$$

4.3. Regularisation

The mathematical term *well-posed* problem stems from a definition given by Jacques Hadamard [24]. He believed that mathematical models of physical phenomena should have the properties that

1. A solution exists
2. The solution is unique
3. The solution's behavior changes continuously with the initial conditions.

If one or more of these properties do not hold, then the problem is called *ill-posed*. Consider the system of equations

$$A\mathbf{x} = \mathbf{b}. \tag{4.46}$$

Such discrete problems inherit the ill-posed properties of the inverse problems: the condition number of the matrix A becomes very large. The matrix A is then called ill-conditioned. The problem $A\mathbf{x} = \mathbf{b}$ or $\min \|A\mathbf{x} - \mathbf{b}\|$ are discrete ill-posed problems if the matrix A is ill conditioned and all its singular values decay to zero in

such a way that there is no particular gap in the singular value spectrum.

Solving ill-conditioned problems is hard because solutions become very sensitive to small perturbations in the right-hand side **b**. Therefore one has to add additional information about the solution **x** in order to produce feasible solutions. This is called regularization of the solution. Also, the high condition number may make the use of direct solving methods useless. Hence we need to consider more advanced solvers that can produce good solutions.
The information in this section originates from [10].

Remember the linear model $A\mathbf{f} = \mathbf{y}$ in Equation (3.68), we now turn to solution methods (for now ignore the ε). In MRI measurements, the noise is gaussian, therefore a natural approach is to estimate **f** by minimizing a regularised least-squares cost function

$$\arg\min_{\mathbf{f}} ||\mathbf{y} - A\mathbf{f}||^2 + \lambda^2 R(\mathbf{f}) \tag{4.47}$$

where λ is the regularisation parameter and $R(\mathbf{f})$ the regularisation term.
When system matrix A is ill-conditioned, the unregularised least squares solution can lead to undesirable noise amplification. To avoid this problem, some form of regularisation is needed.

4.3.1. Tikhonov Regularisation

One of the best known regularisation methods is the 'Tikhonov regularisation'. The general form of the Tikhonov regularisation solution $\mathbf{x}_\lambda$ is defined as

$$\mathbf{x}_\lambda = \min_{\mathbf{x}} \left\{ \|A\mathbf{x} - \mathbf{b}\|^2 + \lambda^2 \|L\mathbf{x}\|^2 \right\}. \tag{4.48}$$

The matrix $L \in \mathbb{R}^{q \times n}$ is called the regularisation matrix. It is a matrix with full row rank, typically a discrete finite difference approximation of a derivative operator Then $L = L_k$ with k the order of the derivative. For example matrices L_1 and L_2 are respectively

$$L_1 = \begin{bmatrix} 0 & -1 & & & 0 \\ 1 & 0 & -1 & & \\ & 1 & \ddots & \ddots & \\ & & \ddots & & -1 \\ 0 & & & 1 & 0 \end{bmatrix}, \quad L_2 = \begin{bmatrix} 2 & -1 & & & 0 \\ -1 & 2 & -1 & & \\ & -1 & \ddots & \ddots & \\ & & \ddots & & -1 \\ 0 & & & -1 & 2 \end{bmatrix}. \tag{4.49}$$

It also contains a-priori information about the solution of the system. In our case, there is one obvious piece of a-priori information: the air pixels should have value 0. In other words, every location within the main magnet that does not contain tissue is air and this cannot change to tissue in the reconstruction.

So the dimension q of L depends on the size of the system, the order of the derivative and the boundary conditions of the problem. In the case that L is an approximation of a derivative operator, Tikhonov does not allow sharp edges. Each choice of L has a different smoothing effect.

The regularisation parameter λ controls the weight given to the minimisation of $\|L\mathbf{x}\|$ relative to the minimisation of the residual norm $\|A\mathbf{x} - \mathbf{b}\|$. Small values of λ imply that the solution has a small residual, the solution satisfies the data well. With this, the a priori information in L is not as important and is filtered away. On the other hand, using large values of λ results in a solution that satisfies the a priori information more. This is useful when the vector **b** is noisy; finding a solution with minimal residual results in a solution closer to the noise than to the solution of the problem itself. Therefore it is important to find a good balance between the two terms by finding the optimal regularisation parameter λ.

To illustrate this consider Figure 4.1 and let $\zeta(\lambda) = \|\mathbf{b} - A\mathbf{x}_\lambda\|_2^2$ and $\eta(\lambda) = \|L\mathbf{x}_\lambda\|_2^2$. The function $\zeta(\lambda)$ will increase monotonically when λ increases and the function $\eta(\lambda)$ will decrease monotonically when λ increases. When these functions are plotted against each other as $\Gamma(\lambda) = \left(\log_{10}\zeta(\lambda), \log_{10}\eta(\lambda)\right)$, one can often observe a 'corner point' in the so called *L-curve*. This is where the optimal value of λ is said to be. Proofs and further

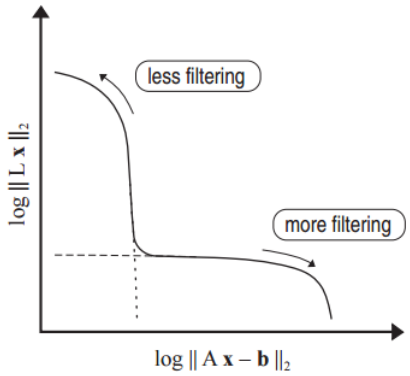

Figure 4.1: Generic illustration of the theoretical L-curve [12].

information on the L-curve will not be included here. The reader is referred to [13] and [14].

In the case that regularisation matrix L is the identity matrix I, then the minimisation problem is

$$\min_{\mathbf{x}} \|A\mathbf{x}-\mathbf{b}\|_2^2 + \lambda^2 \|\mathbf{x}\|_2^2. \tag{4.50}$$

This is equivalent to solving the least squares problem for $\mathbf{x}$:

$$(A^*A+\lambda^2 I)\mathbf{x} = A^*\mathbf{b}. \tag{4.51}$$

Using the pseudo-inverse and substituting the singular value decomposition $A = UWV^*$ it holds that

$$\begin{aligned}
\mathbf{x} &= (A^*A+\lambda^2 I)^{-1}A^*\mathbf{b} \\
&= (VW^*WV^*+\lambda^2 I)^{-1}VW^*U^*\mathbf{b} \\
&= (V(W^*W+\lambda^2 I)V^*)^{-1}VW^*U^*\mathbf{b} \\
&= V(W^*W+\lambda^2 I)^{-1}W^*U^*\mathbf{b} \\
&= \sum_{i=1}^{r} \frac{\sigma_i}{\sigma_i^2+\lambda^2}\mathbf{u}_i^*\mathbf{b}\mathbf{v}_i \\
&= \sum_{i=1}^{r} \left(\frac{\sigma_i^2}{\sigma_i^2+\lambda^2}\right)\frac{\mathbf{u}_i^*\mathbf{b}}{\sigma_i}\mathbf{v}_i.
\end{aligned} \tag{4.52}$$

Now we can see how the regularisation parameter λ influences the solution. The factor in between the brackets are called *filter factors* and if this factor is 1 we have back our initial naive solution as in Equation (4.18). So

$$\varphi_i = \frac{\sigma_i^2}{\sigma_i^2+\lambda^2} \approx \begin{cases} 1 & \text{if } \sigma_i \gg \lambda \\ \sigma_i^2/\lambda^2 & \text{if } \sigma_i \ll \lambda. \end{cases} \tag{4.53}$$

The filter factors filter the singular values. When dealing with large singular values, which implies that λ is much smaller compared to the singular value, then it does not have much influence on the solution. When the singular values become very small, λ will be large compared to it and the filter factor will actually filter out that singular value. Hence the noisy smaller singular values get filtered out, resulting in a better solution.

5

Matlab program for image reconstruction

This section will briefly go over the most important parts of the code.
The programme consists of two Matlab files, the main file 'MRI' and a complementary file 'Imagesignal'.

5.1. Phantom image

'Imagesignal' constructs signal **y** by **y** = A**f** where matrix A is based on Equation (3.67). The image **f** is chosen to be the Shepp-Logan phantom. It is an image of a slice of the head and consists of one large ellipse representing the brain, containing several smaller ellipses representing features in the brain. The amount of features depends on the image quality (i.e. the number of pixels used). Figure 5.1 illustrates examples of the phantom image using 30 × 30 and 128 × 128 pixels.

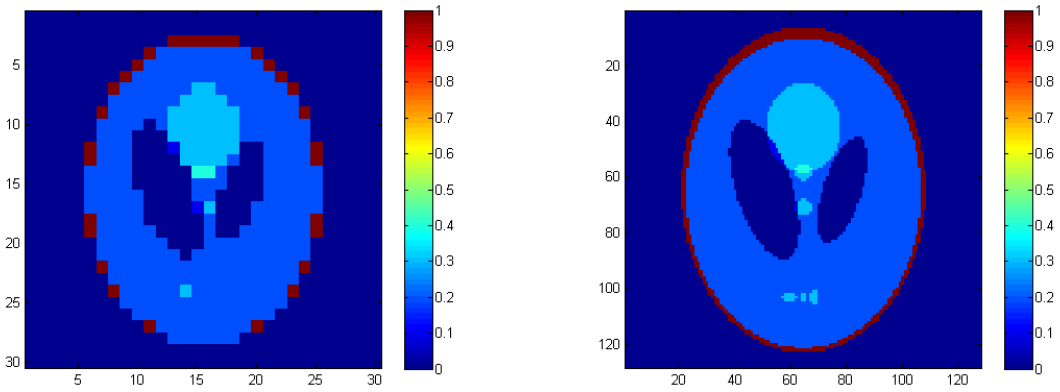

(a) Phantom image using 30 × 30 pixels.

(b) Phantom image using 128 × 128 pixels.

Figure 5.1: Examples of the Shepp-Logan phantom image of sizes 30 × 30 and 128 × 128

The Shepp-Logan phantom image is not only used for creating the signal, but also for comparing the result after the image reconstruction. The values T_2 appointed to the phantom should be realistic. They are given in Table 5.1 [1].

Figure 5.2 puts the values in Table 5.1 in perspective. Note that 250 × 250 pixels are used, so this phantom image is slightly different (and more accurate) to the 30 × 30 pixels phantom image.

Tissue	ρ(%)	T_2(msec)
Scalp	80	70
Bone	12	50
CSF	98	500
Gray Matter	74.5	100
White Matter	61.7	80
Tumor	95	120

Table 5.1: Spin density and relaxation time for the Shepp-Logan phantom [1].

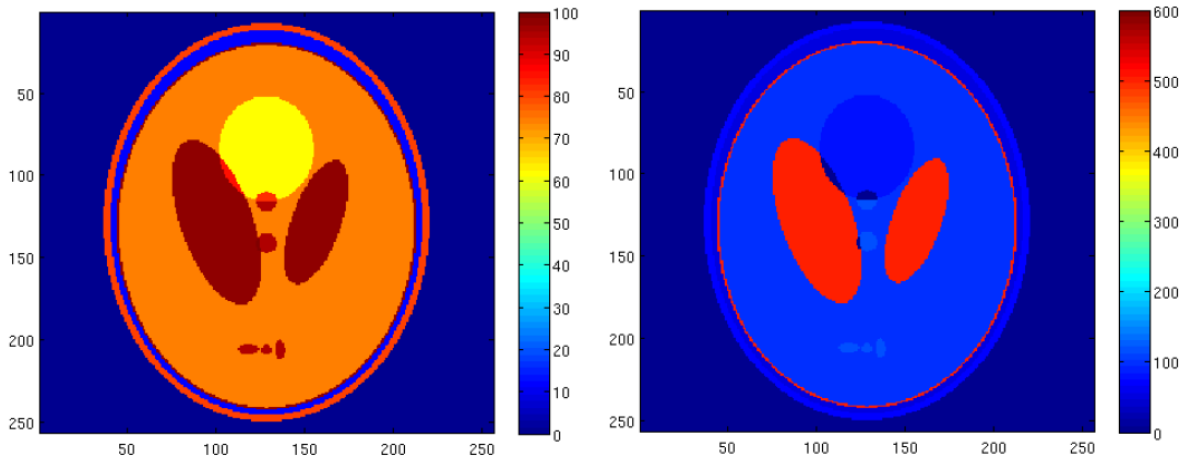

(a) Spin density Shepp-Logan phantom image.

(b) T_2 values Shepp-Logan phantom image.

Figure 5.2: T_2 relaxation time and spin density Shepp-Logan[1].

5.2. Initiation and menu

'Imagesignal' needs more specific information such as the angle between rotations, the number of pixels, the frequency and bandwidth to excite certain spins, the noise, etc. When the program 'MRI' is run, a menu opens. It allows the user to enter the following parameters:

- `noise`; the number entered is a decimal number corresponding to the percentage of noise that should be added to the signal **y**.
- `freq`; the center frequency of the pulse in megahertz. This frequency corresponds to the magnetic flux density field strenght of the total field.
- `bw`; the complete frequency bandwidth in megahertz. So the selected bandwidth ranges from 'freq-bw/2' to 'freq+bw/2'.
- `angles`; the number of degrees the magnet is turned before recording another signal. This is repeated until the magnet is turned 360°.
- `nrofpixels`; the resolution of the phantom image. This image has the same number of pixels in height and width, hence only one value is entered.
- `N`; the total number of (time)steps per rotation. The real total number of timesteps is $N*$(number of rotations).
- `t`; the total time per rotation.
- `lambda`; parameter as in Equation (4.48).
- `epsilon`; a stopping criterion in CGLS, CGNE and 1-norm minimalisation: $\epsilon = 10^{-8}$.

- `m_iter`; maximum number of iterations of the numerical solver.

The phantom image is created with the size of the number of pixels entered in the menu. Next, the Imagesignal file is run. This file starts with initialisation of vectors used in the file and appointing T_2 values to corresponding parts of the phantom. The remaining part of the complementary file is a loop over every rotation (depending on 'angles'). For every angle/rotation the magnetic flux density field values are calculated using the polyfit function file. This can then be used to calculate ω_0, ΔB_z and when needed T_2^*. These aspects in the complementary file will be explained in Sections 5.3-5.5. Next the selection of the frequency bandwidth is calculated and a temporary matrix A is calculated. After all loop iterations, everything is put together to create the total matrix A and A is used to construct the total signal $\mathbf{y}$. 'MRI' uses these $\mathbf{y}$ and A to find a reconstruction using an iterative solver (which runs a maximum number of iterations `m_iter`) and the regularisation with the regularisation parameter from the menu.

5.3. Magnetic flux density field, $\omega_0(\mathbf{r})$ and $\Delta B_z(\mathbf{r})$

The information available on the strength of the magnetic field from the main magnet are measured and presented in Figure 3.4b. We have used the information from positions in the 7×9 matrix which are not NaN's. The information is very limited and more information needs to be found in between those measurement points. Otherwise the image quality is also limited (to `nrofpixels`$= 5$, $n_p = 25$). In the end, the number of points needs to equal the total number of pixels of the phantom image. This is because we need to know $\omega_0(\mathbf{r})$ and ΔB_z for every pixel.

There are two methods to go about finding these:

1. Interpolation in Matlab
2. Curve fitting tool in Matlab

Note that the area is actually square, meaning that the error from measuring as shown in Figure 3.5c has to be taken into account for both cases. Also note that the y component is neglected: only a slice in the main magnet is used.

In the beginning of the project, interpolation was used to find both ω and ΔB_z. At the final stages interpolation was replaced by method two. The curve fitting tool in Matlab allows the user to import given data (in this case Jelle's measurements) and let the tool fit a polynomial of a given order. The highest possible order that can be entered in this application is 5.

An advantage of using the polynomial from the curve fitting as the magnetic flux density field compared to interpolation, is that interpolation interpolates piecewise. The measurements from Jelle have more influence and interpolation is therefore more prone to measurement errors. The curve fitting does not necessarily include the given data points but fits a smooth polynomial as close as possible to the measurement points. Appendix C will give more information about the polynomial fit.

5.4. Selection $c(\mathbf{r})$

$\mathbf{c}(\mathbf{r})$ contains much information including the receiver coil sensitivity and the accuracy of the sent signal (bandwidth ω_{RF}). However, these two are not yet used in the current model. This is because the receiver coil sensitivity depends on each coil, so this can be measured when the RF coil is made. The accuracy of the frequency bandwidth is programmed in the model, but is not used in the results. Therefore the vector $\mathbf{c}(\mathbf{r})$ only contains the exact selection of the frequency bandwidth.
As for the bandwidth accuracy; if the transmitter is flawless, the excited spins are those with frequencies exactly equal to the frequencies of the chosen bandwidth. The 'sensitivity' at the corresponding pixels is equal to 1 (within the bandwidth) and is equal to zero otherwise (outside the bandwidth) (see Figure 5.3).
In reality, some spins can be excited just outside the bandwidth because of the accuracy of the transmitter. However their contribution is lower and hence a more realistic option is that the sensitivity decreases when further away from the bandwidth as in Figure 5.4.

Using the exact selection method makes the programming easy. When considering a less accurate transmitter extra steps are taken. For ease of programming, we have chosen to look at this in each row before rotating.

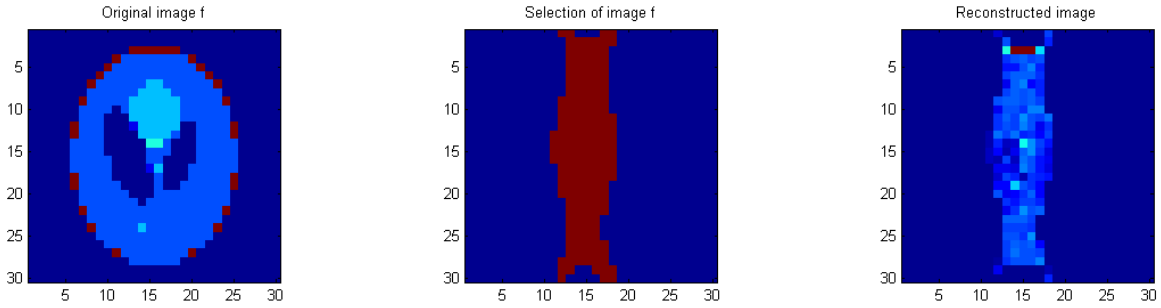

Figure 5.3: Image reconstruction with a *precise* selection using a central frequency 12 MHz and a bandwidth of 0.7 MHz. Maximum number of iterations is 200, no noise is added to the model and T_2 is considered known. This way only the effect of the selection is shown.

The first step is the same as with the exact selection, next the boundary pixels have to be found. These are then used to fit a Gaussian function with `gauss2mf` in Matlab to make a smooth transition from value 1 in the bandwidth to 0 outside the bandwidth. After the rotation this transition will be in all directions (of the chosen angles).

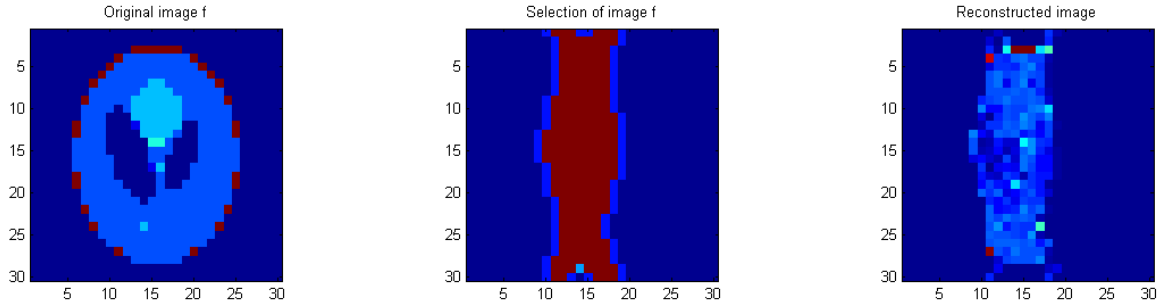

Figure 5.4: Image reconstruction with an *inaccuracy in sent bandwidth*. Again using a central frequency 12 MHz and a bandwidth of 0.7 MHz. Maximum number of iterations is 200, no noise is added to the model and T_2 is considered known. This way only the effect of the selection is shown.

5.5. Rotating and final system matrix A

Note that without rotation, the matrix A in Equation (3.67) has matrix has elements

$$\{a_{ij}\} = c(r_j)\omega_0(r_j)e^{-t_i/T_2(r_j)}e^{-i\gamma\Delta B_z(r_j)t_i}. \tag{5.1}$$

A is a matrix of complex exponentials depending on time (i) and space (j). The columns of A contain all timesteps of a specific location. It will be a full matrix without any obvious patterns when a pulse is sent out which has a bandwidth containing all frequencies of the main magnetic field. When using one of the methods above and selecting a bandwidth not covering all frequencies, many columns will consist of zeros; these are the locations of spins which are not excited.

To create a signal $\mathbf{y} = A\mathbf{f}$ the phantom image needs to be multiplied with the matrix A. To create this matrix A, we need ω_0, c, T_2 and ΔB_z. To make the model fit reality better a different matrix A needs to be used for the reconstruction (A_{rec}): the properties T_2 of the tissue is unknown. This is not done at the moment. For more information see Chapter 8.2.2.

Rotating the interpolated field can be done using the 'imrotate' command in Matlab. With the feature 'crop' the image (or matrix) is rotated and brought back to the original size (rotated and cropped viewed from the center point). The rotation can also be done using a rotation matrix and the result from the curve fitting. More about this can be found in Appendix C.

With rotations, this matrix A needs to be recalculated. These matrices are then stored underneath eachother. The total matrix A is multiplied by the phantom image vector and a signal is created.

5.6. Output

An example of the output of the matlab programme is shown in Figure 5.5. It consists of six subplots of which the lower three have been shown before. From left to right they show the original image **f**, the selection of the first rotation and the reconstructed image.

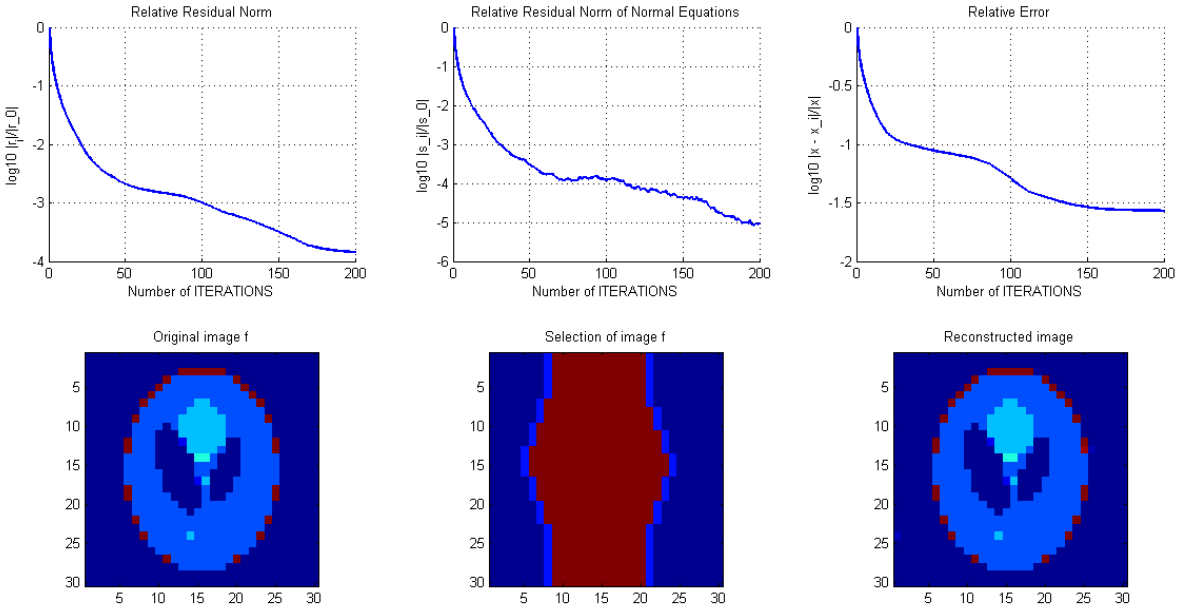

Figure 5.5: Output of the Matlab programme, using freq= 12 MHz, bw= 3 MHz, its= 200, angles= 70°, noise= 0, T_2 considered known.

The top three subplots show, from left to right, the relative residual norm, the reslative residual norm of normal equations and the relative error. The horizontal axes all show the number of iterations. The vertical axes are logarthmic scales of respectively $\|\mathbf{r}_i/\mathbf{r}_0\|$, $\|\mathbf{s}_i/\mathbf{s}_0\|$ and $\|\mathbf{x}_i/\mathbf{x}_0\|$ with i from 1 to k (the number of iterations).Also $\mathbf{x}_0 = \mathbf{0}$, $\mathbf{r}_0 = \mathbf{f}$ and $\mathbf{s}_0 = A^*\mathbf{f}$.

6

Analysis of the model

This chapter will show some implementation considerations of the model, such as the Nyquist rate, the method of rotating and the size of the frequency bandwidth. Also, the sensitivity to errors in the magnetic field measurements are analysed.

6.1. Information in the system

In the signal processing, sampling is used to reduce the continuous signal to a discrete signal. To translate the discrete signal samples back to a continuous signal successfully, some conditions have to be satisfied. One of these is the Nyquist rate.

6.1.1. Nyquist rate

The sample frequency (or sampling rate) is the number of samples obtained in one second. The sampling rate has a lower bound which comes from the Nyquist rate. It is the lowest sampling rate that can represent a bandwidth constrained signal. In other words, it is the lowest sampling rate which allows the original continuous signal to be reconstructed from discrete samples. If a signal is sampled at frequency f_s with highest occuring frequency f_0 then the *Nyquist rate* is $2f_0$. It is a strict lower bound, so $f_s > 2f_0$, hence $2.2f_0$ is used for the minimum sampling rate.
To get an idea of the upper bound for the timesteps, we looked at the extreme values of the measured field. The highest measured magnetic flux density of the main magnet is 426 mT and the lowest is 277 mT. Table 6.1 gives the corresponding upperbound for the timestep.

Field strength	sampling rate (f_0)	Nyquist rate ($2.2f_0$)	upperbound dt
277 mT	$1.1795 \cdot 10^7$ Hz	$2.5948 \cdot 10^7$ Hz	$3.8538 \cdot 10^{-8}$ s
279 mT	$1.1880 \cdot 10^7$ Hz	$2.6136 \cdot 10^7$ Hz	$3.8261 \cdot 10^{-8}$ s
342 mT	$1.4562 \cdot 10^7$ Hz	$3.2037 \cdot 10^7$ Hz	$3.1215 \cdot 10^{-8}$ s
426 mT	18139080 Hz	39905976 Hz	$2.5059 \cdot 10^{-8}$ s

Table 6.1: Magnetic flux density field strength with corresponding upperbound for dt. The highest and lowest values are those from the measurements.

The magnetic flux density varies 149 mT. When downsampling is used, this value will be the highest frequency that can be sampled. Multiplied with γ, this results in a Nyquist frequency of 6344420 Hz. Therefore the minimum sampling frequency (at $2.2f_0$) and the upperbound of the timestep are respectively $1.3958 \cdot 10^7$ Hz and $7.1645 \cdot 10^{-8}$ s. Note that as the maximum value of 426 mT lies in a corner point and when using a more central locations, lower field strengths are used. This allows slightly larger timesteps.

After these initial calculations we used a polynomial fit for the field, which changes the field slightly. This is most visible on the edge of the magnet where the values are slightly higher. Also we started rotating, this

means there can be higher values on all positions close to the edge of the magnet. Therefore the upperbound should be reevaluated.

Using an angle between rotations of 70°, the maximum of the full field is 0.7069 T and the minimum is 0.1846 T. The maximum of the rotated ΔB_z field is 0.4252 T. This maximum is always in a corner pixel, because of the way the field is constructed.

Another way to formulate the Nyquist rate is by the lower bound 2bw (with bw the bandwidth). It is again a strict lower bound, so $f_s > 2\text{bw}$, therefore for the minumum sampling rate, 2.2bw is used.

In the area where the phantom head is present and the selection is made, the maximum frequency of the *full* field is 13.5 MHz and the minimum 10.5 MHz for center frequency of 12 MHz and a bandwidth 3 MHz. Because of downsampling, the size of the bandwidth is then equal to the sampling frequency. With this a similar but more accurate upperbound can be found for our problem (see Table 6.2).

Sampling rate (f_s =bw)	Nyquist rate ($2.2 f_s$ = 2.2bw)	Upperbound dt
1 MHz	2.2 MHz	$4.5455 \cdot 10^{-7}$ s
2 MHz	4.4 MHz	$2.2727 \cdot 10^{-7}$ s
3 MHz	6.6 MHz	$1.5152 \cdot 10^{-7}$ s

Table 6.2: Using downsampling so that the bandwidth is the sampling rate, with corresponding Nyquist rate and upperbound for dt.

So what is the actual upperbound of the current model version? For the total time we keep 10^{-4} s, so we will look at different N (number of time samples per rotation). We choose a maximum number of iterations that does not limit the real maximum number of iterations needed for the numerical solvers and look at the resulting image reconstruction. The information in Table 6.3 shows the qualitative result of the image reconstruction.

N	corresponding timestep dt	number of iterations	image quality
100	$1.0000 \cdot 10^{-6}$ s	450	bad
150	$6.6667 \cdot 10^{-7}$ s	4500	almost perfect
160	$6.2500 \cdot 10^{-7}$ s	2503	almost perfect
161	$6.2112 \cdot 10^{-7}$ s	2283	perfect
162	$6.1728 \cdot 10^{-7}$ s	2082	perfect
165	$6.0606 \cdot 10^{-7}$ s	2021	perfect

Table 6.3: Number of timesteps versus image quality. Number of timesteps together with total time determines an upperbound for dt satisfying Nyquist rate.

Figure 6.1 illustrates the image quality from Table 6.3. It is very clear what a timestep higher than the upperbound does in Figure 6.1a and therefore the importance of satisfying the upperbound.

In conclusion, if the total time is 10^{-4} and the minimum number of total timesteps for a perfect image is 161, then dt= $10^{-4}/161 = 6.2112 \cdot 10^{-7}$. This does not match the upperbound found in Table 6.2. This second approach might be optimistic, because the model is not complete. It is better to satisfy the upperbound given in Table 6.2, choosing dt= 10^{-7} s will cover the highest chosen bandwidth.

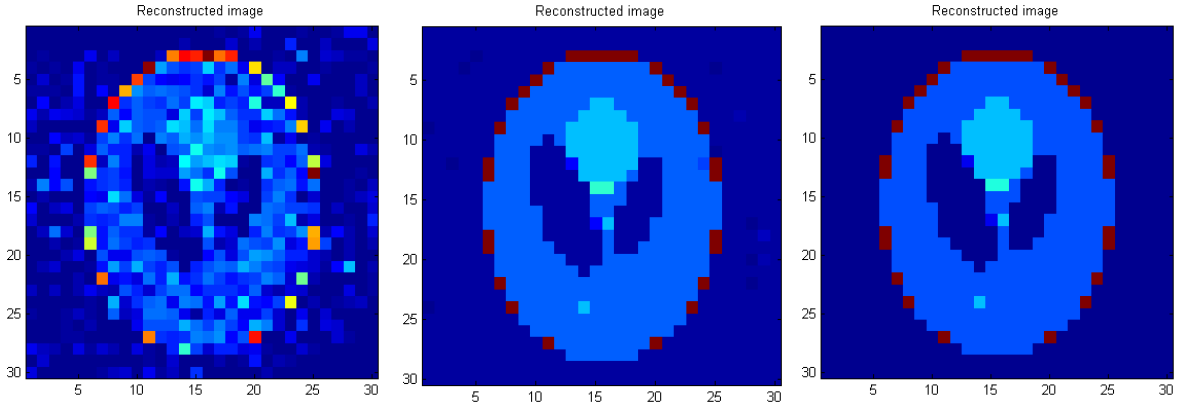

(a) Bad quality at $N = 100$ (dt= $1.0000 \cdot 10^{-6}$)

(b) Almost perfect quality at $N = 150$ (dt= $6.6667 \cdot 10^{-7}$)

(c) Perfect quality at $N = 161$ (dt= $6.2112 \cdot 10^{-7}$)

Figure 6.1: Visual of qualitative measures 'bad', 'almost perfect' and 'perfect'. Using freq= 12 MHz, bw= 3 MHz, noise= 0.

6.1.2. Methods: rotating and size frequency band

Optimising the image reconstruction for this project includes the careful balancing between a few factors. More rotations means a longer MRI scanning time. Therefore, the minimum number of rotations still producing good images needs to be found. In order to do this, we will look at the rank of matrix A. Note that T_2 is taken as known in the image reconstruction and therefore if no noise is included, the reconstruction should be equal to the phantom image.

The number of rows of matrix A depends on the total timesteps per rotation (N) and the number of rotations (n_r), whereas the number of columns solely depends on the number of pixels (n_p). Matrix A is therefore of full rank if it equals the total number of pixels. If nrofpixels= 30 is used, then the matrix is of full rank when the rank equals $n_p = 30 \cdot 30 = 900$. However, the system matrix in this project is rank deficient (its rank is not equal to the lesser of the number of rows and columns). Singular values can be used to determine the so called *effective rank* of a matrix, as rounding errors can lead to small but non-zero singular values. The rank is equal to the number of non-zero singular values. A line needs to be drawn where the small non-zero singular values will be treated as zero.

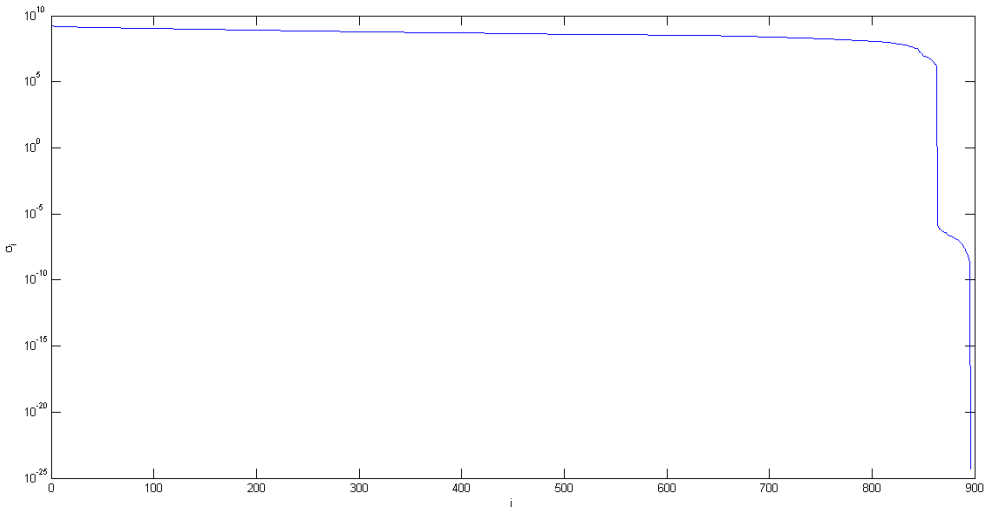

Figure 6.2: The singular values of A, using angles= 70°.

This can be estimated by looking at a plot of singular values in Figure 6.2. The singular values are mostly very

large ($\approx 10^8$) then quickly go down in almost a vertical line to 10^{-7}. From this can be concluded that this boundary can be anywhere between 10^{-7} to 10^4 without the effective rank differing sufficiently.

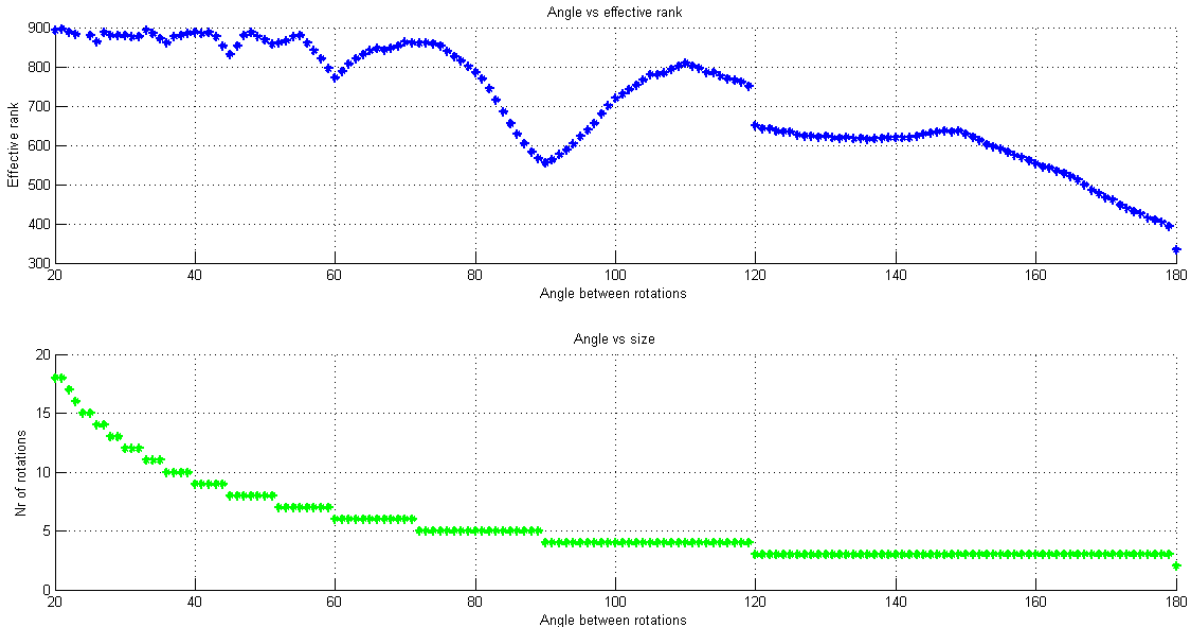

Figure 6.3: Bottom plot showing angle between rotations versus the number of rotations. Top plot showing the angle between rotation versus the first singular value to be lower than 1. Used freq= 12 MHz, bw= 3 MHz, nrofpixels= 30.

.

Figure 6.3 contains much information in two plots. The bottom plot has on the horizontal axis the angle between rotations (`angles`). This is done this way because of the Matlab programming: `angle=1:angles:360` degrees. The number of rotations is shown on the vertical axis. To clear this up: the number of rotations multiplied by $N = 1000$ (number of timesteps per rotation) gives the number of rows of matrix A. The number of rows is at least 1000 and the number of singular values is 900, because the number of pixels is 30. The top plot has the same horizontal axis. The vertical axis shows the number of singular values greater than 1 as the effective rank. This is the initial choice made for the distinction of the effective rank.
The angle between rotations goes up to 180° because at 181° and up, the effective rank has dropped so low that no sufficient reconstruction can be made.

A result that is very noticable is the drop of the effective rank at angles 120°, 90°, 60° and 45°. For every case it corresponds with a drop in the number of rotations and therefore the number of rows. However, not at every drop of the number of rotations the rank decreases. A possible explanation is that at the angles mentioned above are most likely very close to a symmetry in the magnetic field. This then results in multiple equal equations to solve, leading to a lower rank.

There does not seem to be a relation between the angle between rotations, the effective rank and the number of rotations. It is not always the same value for `angles` (the first, second, last, etc after a drop) within a rotation that has the maximum rank. To prove it is not because of the chosen boundary value for the effective rank, we chose two other values of respectively 1 and 2 orders smaller. The results are in Figure 6.4. The only difference is when the angle between rotations is between 110° and 150°, but the pattern remains the same. This effect has been predicted as the drop in singular value is almost vertical in Figure 6.2.

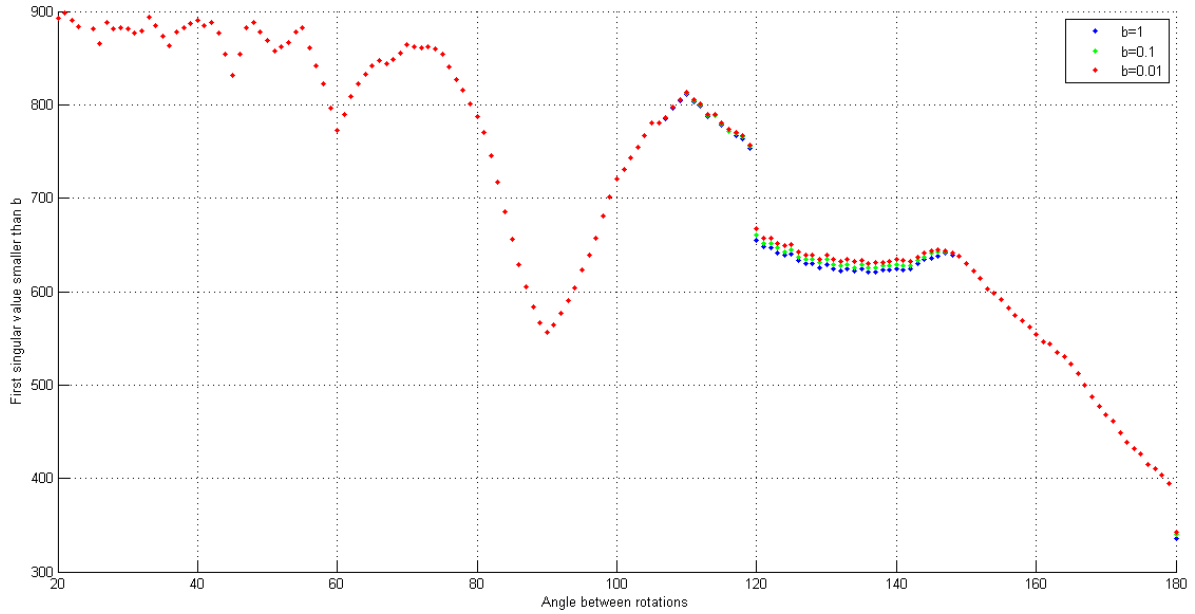

Figure 6.4: The angle between rotation versus the effective rank (first singular value to be lower than b). Used freq= 12 MHz, bw= 3 MHz, nrofpixels= 30.

Secondly, the chosen bandwidth does influence the rank, see Figure 6.5. It shows for three bandwidths what the effective rank is at different angles between rotations. The number of singular value decrease with similar patterns for the three bandwidths.

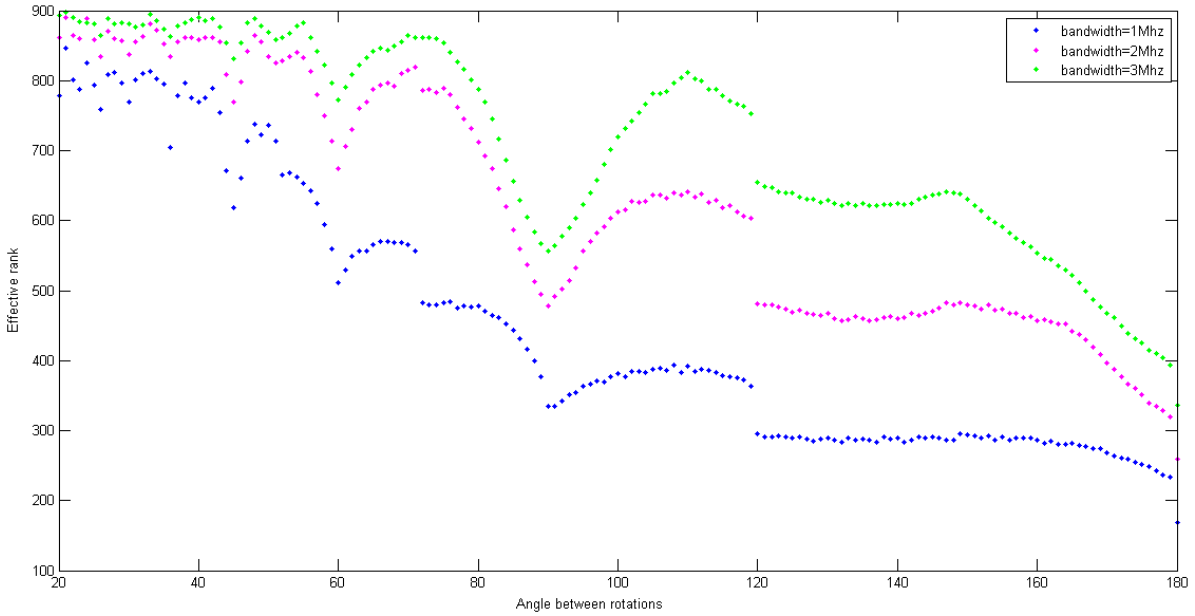

Figure 6.5: For bandwidths of 1, 2, and 3 MHz, the number of angles is plotted against the effective rank (number of non-zero singular values based on $b = 1$). Used freq= 12 MHz, nrofpixels= 30.

A bandwidth of 3 MHz (see Figure 6.6c) covers almost the entire area with a few rotations. For a smaller bandwidth this might not be true and could need more rotations for the same resulting image. This can also be seen in Figure 6.5: as the bandwidth increases so does the effective rank (for all angles between rotations). This is because the number of zero columns in A per rotation will decrease, leading to an increase in effective rank.

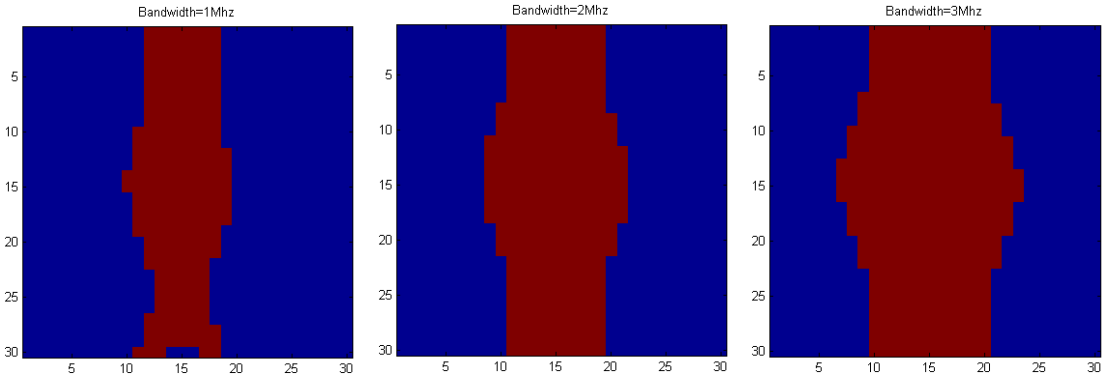

(a) bw= 1 MHz. (b) bw= 2 MHz. (c) bw= 3 MHz.

Figure 6.6: Selection with bandwidths of 1, 2 and 3 MHz

Another way to analyse the optimal number of rotations in the current case is as follows. Consider one single rotation (so `angles`=360), estimate the rank and then divide 900 by that rank to see what value for `angles` could give a full rank. The associated number of rotations will be an option for the optimal number of rotations.

Figure 6.7 shows the first singular value to be lower than b, with b on the horizontal axis. The bandwidth used is 3 MHz. In Figure 6.3 the value b is chosen to be 1, but can certainly be different. Choosing $b = 1$ gives a rank of 198 and $b = 0.01$ gives a rank of 204. Hence, dropping the order of b by 2 only increases the effective rank with 6. Say the effective rank is 200 for one rotation. To get a rank of 900, at least 5 rotations need to be made. That corresponds to the angle between rotations to be at most $(360°/5)$ 89°. From Figure 6.5 it follows that for 5 rotations the optimal value for angles= 72° giving an effective rank of 860.

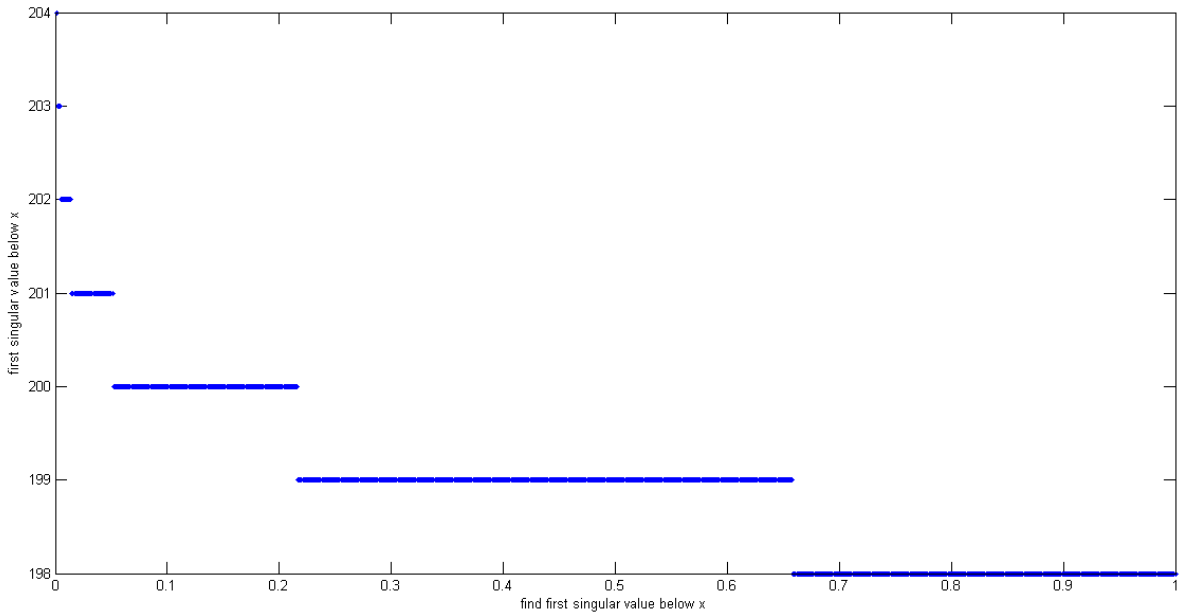

Figure 6.7: One rotation. Horizontal axis is the value b such that we find first singular value to be lower than b. Vertical axis corresponds to the first singular value to be lower than b.

.

With the same approach using the smaller bandwidths of 1 MHz and 2 MHz the rank of 1 rotation is respectively approximately 97 and 148 . To achieve a rank of 900, at least 10 rotations are necessary for bw= 1 MHz and 7 rotation for bw= 2 MHz. This corresponds to the angle between rotation of at most 39° and 59°. For bw= 1 MHz the optimal effective rank is at 33° with value 813. The effective rank for bw= 2 MHz is highest at

angles= 48° with rank 864.

In conclusion, the number of rotations needed for a high effective rank is estimated for three different bandwidths (Table 6.4)

Bandwith `bw`	min. number of rotations	max. `angles`	optimal `angles`	effective rank
3	5	89	72	860
2	7	59	48	864
1	10	39	33	813

Table 6.4: Results analysis of the optimal number of rotations.

From this can be concluded that a bandwidth of 3 MHz will most probably be the best to use. An example of a factor this still depends on is the effect of the different numerical solvers and regularisations. Another factor is whether an extra rotation outweighs the necessary additional time and if the small difference in effective rank eventually has a significant influence or not.

6.2. Perturbing the field strength

At this moment in time, the signal is acquired by multiplying the phantom image with the matrix A. The matrix A contains the field strengths which are acquired from Jelle's measurements. The measurements are subject to errors, even though the measurements have been repeated thrice to minimise the largest errors. The noise is estimated by Jelle to be less than 0.060 mT where the average field strength is about 350 mT.

The possible errors can be due to human errors in the measurements, which is the motivation for a perturbation analysis on the 3rd decimal when working in tesla (e.g. 0.277 T). The accuracy of the measuring tool is also important: with 3 decimals (e.g. 0.277 T) there is an uncertainty in the next decimal(s). Therefore a perturbation analysis on the 4th decimal would be in order. If the analyses show that perturbations in the orders 10^{-3} and 10^{-4} are such that they make a big difference in the outcome, an analysis can be done in an order smaller. The goal is finding the order of the perturbation that still allows a reasonable reconstruction, which can later be improved with the correct choice of iterative solver and regularisation.

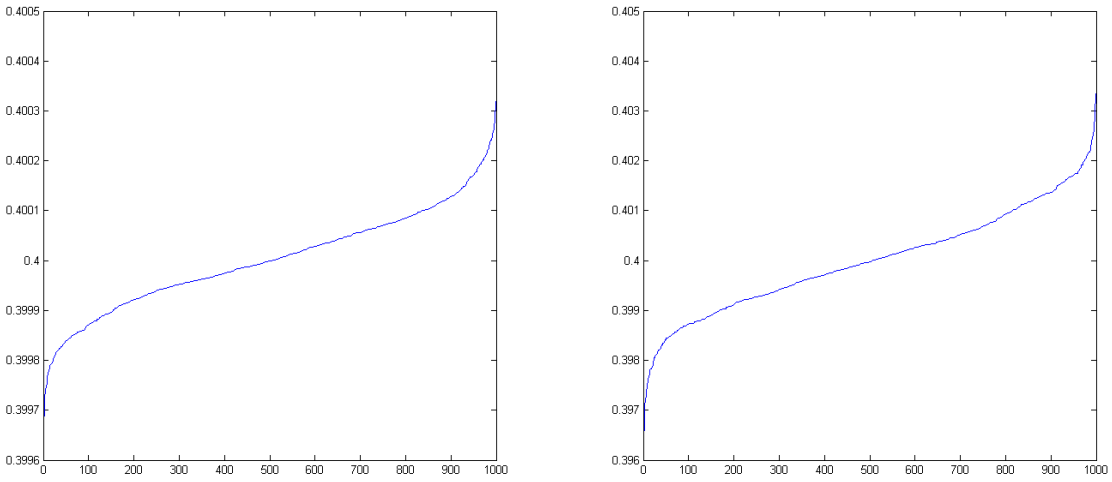

(a) Example of possible values of the perturbation on the accuracy of measurement tool (10^{-4})

(b) Example of possible values of the perturbation on Jelle's measurement error (10^{-3}).

Figure 6.8: Example of possible values of a perturbation on a field strength of 400 mT for two cases.

The actual signal contains the 4th and higher decimals of the magnetic flux density field strengths, which are

neglected by the measuring device. Therefore in producing the artificial signal **y**, the field should contain a perturbation. The field acquired by Jelle should be kept the same for the image reconstruction matrix A.

For illustrative purposes assume that a field strength of 0.400 T is measured. If the measuring tool rounds to the nearest 3rd decimal, then the real value for the field strength could be anywhere between 0.3995000... and 0.4004999.... To simulate this we use 'randn' in Matlab to generate a random number with mean 0.400 and standard deviation 10^{-4}. An example of 1000 generated random numbers (sorted from smalles to largest) is shown in Figure 6.8a. Similarly an example for perturbation 10^{-3} is shown in Figure 6.8b. Note that the values (including the extreme values) can differ slightly when the random number generator is run again.

In the case that Jelle made a measuring error (this could be a slight displacement of the measuring tool in any direction) we are not looking at a rounding error, but an error in a decimal place. Assume that the measuring error can be a few millitesla, Figure 6.8b illustrates an example of 1000 possible values (sorted).

6.2.1. Case 1: 10^{-1} mT accuracy of measuring tool error

When working in tesla, the added perturbation is a random variable from the normal distribution. The mean is equal to Jelle's measurement value (in tesla) and the deviation is equal to 10^{-4} (using millitesla's results in using the deviation of 0.1).

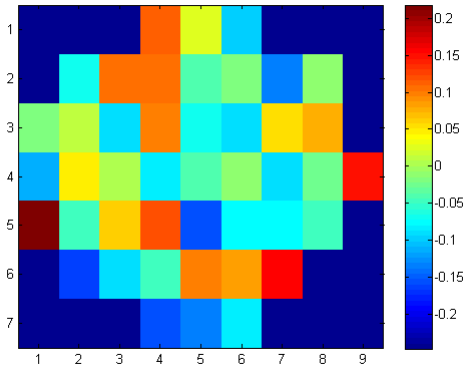

Figure 6.9: Perturbation per data point with which the polynomial is refitted. The values are in millitesla.

Figure 6.9 shows the perturbations per measured point. These are random: running the code again will give a different image. The field including the perturbations is now entered in the curve fitting tool in Matlab to find the new coefficients of the corresponding polynomial. These coefficients can be found in Table 6.5. Note that these coefficients differ only slightly from the original coefficients (in Table C.1).
It *could* be possible that the smooth fitted curve is (almost) the same, because the variations are random so the effect is damped but not necessarily cancelled. Also because the values are still within the confidence bounds of the original fit in Table C.1 and the image quality plays a role (we only consider nrofpixels= 30). The fit could give the same values on a coarser image quality.

The first results are done with the angle between rotation of 70°. This is because the effective rank of matrix A is relatively high for the needed number of rotations (hence the size of A). For the full resulting images the reader is referred to Appendix D.1.

The reconstructed image and the relative error for `angles`= 70° are shown in Figure 6.10a. Both are unuseable results: the constructed image doesn't seem to have any correct pixel and overall it looks like noise. The relative error supports this: it increases to 1.25 on the logarithmic axis. The question is whether increasing the number of rotations will add sufficient information for a useful reconstruction. Figures 6.10b and 6.10c show the results for `angle`= 30° and `angle`= 10° respectively.

For these angles the relative error is semi-convergent: it decreases from 0 (just below 0 on the logarithmic scale), but increases after a few iterations to about −0.038 and −0.112 on the logarithmic scale. Looking at

p00 =	281.8	(278.5, 285.1	p31 =	0.0001361	(-3.921e-05, 0.0003114)
p10 =	0.3446	(-0.2864, 0.9756)	p22 =	0.001779	(0.00158, 0.001979)
p01 =	-0.1033	(-0.8125, 0.6059)	p13 =	-0.0001046	(-0.0002852, 7.593e-05)
p20 =	0.3024	(0.2616, 0.3431)	p04 =	-0.0002549	(-0.0003692, -0.0001406)
p11 =	0.008601	(-0.04226, 0.05946)	p50 =	5.339e-06	(-4.284e-06, 1.496e-05)
p02 =	0.05964	(0.01386, 0.1054)	p41 =	-2.939e-06	(-2.029e-05, 1.441e-05)
p30 =	-0.002805	(-0.007967, 0.002357)	p32 =	1.364e-05	(-1.069e-05, 3.796e-05)
p21 =	0.0003657	(-0.007059, 0.00779)	p23 =	-3.821e-06	(-3.311e-05, 2.547e-05)
p12 =	-0.002467	(-0.01028, 0.005341)	p14 =	3.773e-06	(-1.637e-05, 2.392e-05)
p03 =	9.871e-05	(-0.006764, 0.006961)	p05 =	3.667e-07	(-1.379e-05, 1.452e-05)
p40 =	-6.483e-05	(-0.0001618, 3.211e-05)			

Table 6.5: Coefficients in milli Tesla and their 95% confidence bounds that differ from the original coefficients. When all coefficients are multiplied by 10^{-3} the polynomial represents the values in tesla. Goodness of fit: sum of squared error(SSE): 289.2, R-square: 0.9969, Adjusted R-square: 0.9943, root mean square error (RMSE): 3.471

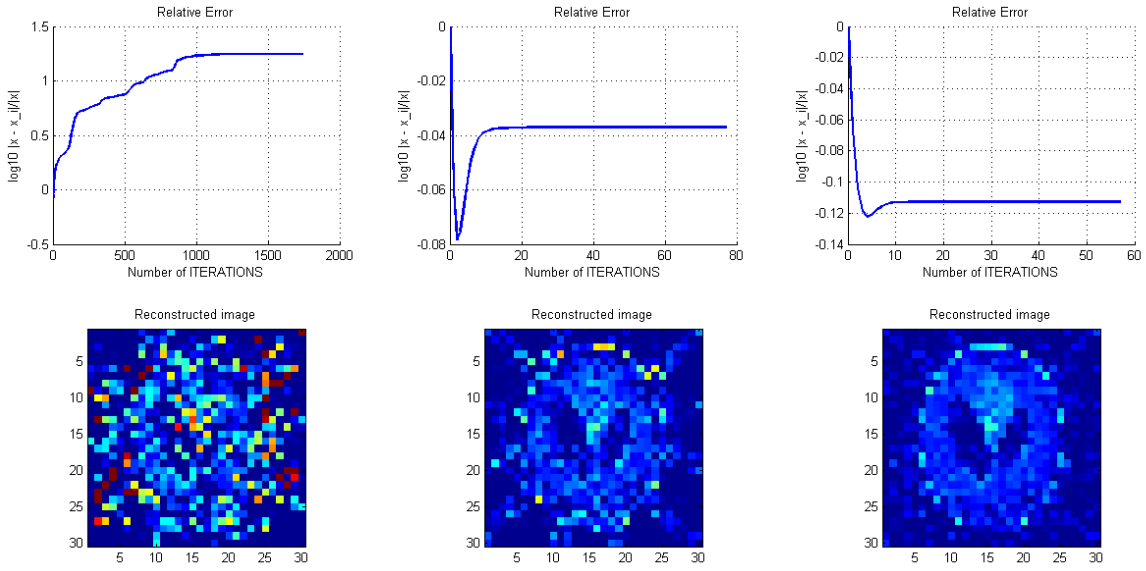

(a) angle= 70° (b) angle= 30° (c) angle= 10°

Figure 6.10: Results with a 0.1 mT perturbation using CGLS, freq= 12 MHz, bw= 3 MHz

the reconstructed images the overal 'head' is visible but lost the smaller necessary details. Also, all the values are lower than they should be: dark blue is 0 and red is 1 (see Figure 5.1).

In conclusion, for the optimal bandwidth of 3 MHz we previously found that with 5 rotations the effective rank was 860 (full rank is 900). With a perturbation the result is in Figure 6.10a, which indicates that the image cannot be reconstructed. Using more rotations is more time consuming but does give an image that might be able to be reconstructed.

6.2.2. Case 2: 1 mT measuring error

In case 1 it is concluded that the image reconstruction with 5 rotations does not suffice. This implies that the same conclusion but with degraded results are expected for case 2. After all, the perturbation is an order larger. However, because of the polynomial fit it is still interesting to see the results.

In Figure 6.11 the used perturbations are shown and Table 6.6 shows the corresponding coefficients. The coefficients differ more from the original than in the previous case, but the goodness of fit has higher error values indicating a larger effect of the smoothing of the polynomial fit.

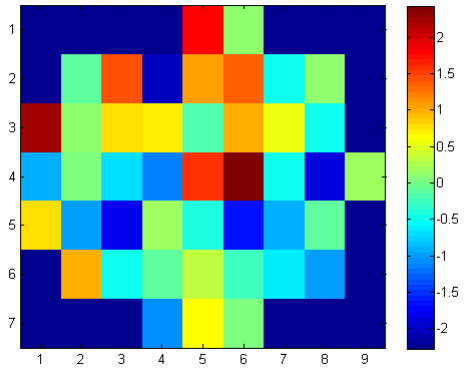

Figure 6.11: Perturbation per data point with which the polynomial is refitted. The values are in milli tesla.

p00 =	281.2	(277.8, 284.5)	p31 =	0.0001265	(-4.899e-05, 0.0003019)
p10 =	0.2358	(-0.3957, 0.8672)	p22 =	0.001741	(0.001541, 0.00194)
p01 =	0.004484	(-0.7052, 0.7142)	p13 =	-8.47e-05	(-0.0002654, 9.598e-05)
p20 =	0.3155	(0.2748, 0.3563)	p04 =	-0.0002579	(-0.0003723, -0.0001436)
p11 =	0.008287	(-0.04261, 0.05918)	p50 =	3.834e-06	(-5.796e-06, 1.346e-05)
p02 =	0.06273	(0.01692, 0.1085)	p41 =	-3.918e-06	(-2.128e-05, 1.344e-05)
p30 =	-0.001935	(-0.0071, 0.00323)	p32 =	1.311e-05	(-1.123e-05, 3.745e-05)
p21 =	0.0007393	(-0.00669, 0.008169)	p23 =	-5.72e-06	(-3.503e-05, 2.359e-05)
p12 =	-0.001747	(-0.009561, 0.006066)	p14 =	1.016e-06	(-1.914e-05, 2.118e-05)
p03 =	-0.0006282	(-0.007495, 0.006239)	p05 =	1.575e-06	(-1.259e-05, 1.574e-05)
p40 =	-9.502e-05	(-0.000192, 1.981e-06)			

Table 6.6: Coefficients in milli Tesla and their 95% confidence bounds that differ from the original coefficients. Goodness of fit: SSE: 289.5, R-square: 0.9969, Adjusted R-square: 0.9943, RMSE: 3.473

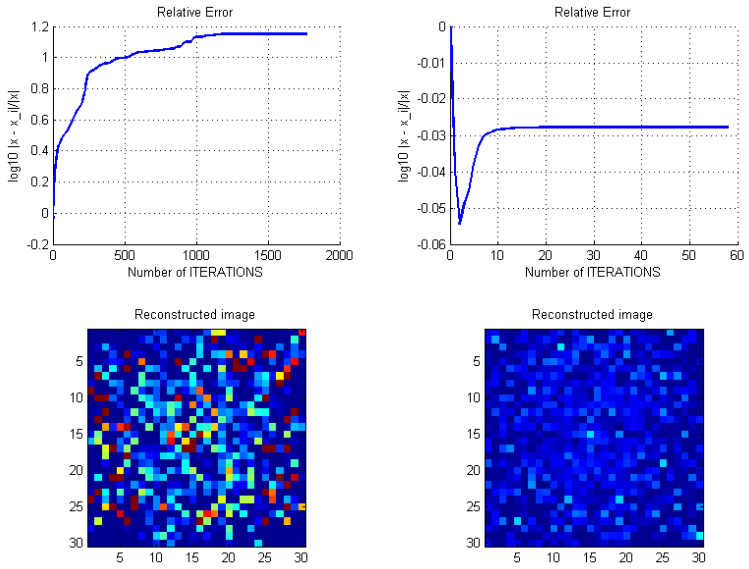

(a) angle= 70° (b) angle= 10°

Figure 6.12: Results with a 1 mT perturbation using CGLS, freq= 12 MHz, bw= 3 MHz.

The result in Figure 6.12a is very similar to the result in Figure 6.10a. The relative error increases quickly only reaches a maximum slightly lower (≈ 1.18) than in the previous case and the image is scattered. Using the

same approach, we ran the programme using angle= 10° and see no result at all (see Figure 6.12b). The relative error does decrease but the original image is lost.

From this it can be concluded that making errors of a few millitesla can destroy the image reconstruction. Therefore, the measurements should be taken with great care. Especially in the current set-up in which we are working with such a small space and few possible measurement points.

6.2.3. Case 3: 10^{-2} mT

Both case 1 and case 2 show that there is no room for error in the order of 1 mT and a miniscule room for error in 10^{-1} mT. This means that with the correct iterative methods and regularisation methods/parameters it might be possible for a reasonable reconstruction. However, this should then be closely examined and researched.
It is interesting to see whether the next smaller order (10^{-2} mT) perturbation will give results with sufficient information. If not, the (size of the) model set-up needs to be reconsidered or a different, more accurate technique needs to be used to acquire the field data.

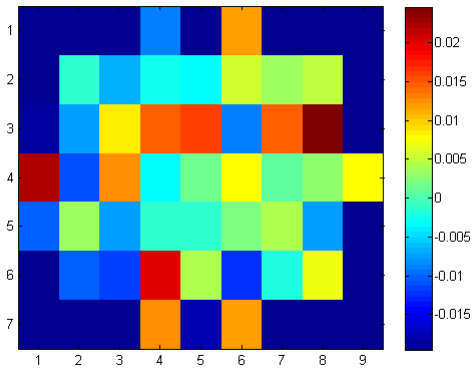

Figure 6.13: Perturbation per data point with which the polynomial is refitted. The values are in milli tesla.

Again the used perturbations and the corresponding polynomial fit coefficients are given (see Figure 6.13 and Table 6.7 respectively). As expected the values of the coefficients are close to the values of the original field coefficients.

p00 =	281.7	(278.4, 285)	p31 =	0.000131	(-4.277e-05, 0.0003048)
p10 =	0.332	(-0.2935, 0.9576)	p22 =	0.001773	(0.001576, 0.001971)
p01 =	-0.1054	(-0.8084, 0.5976)	p13 =	-0.000103	(-0.000282, 7.6e-05)
p20 =	0.3027	(0.2623, 0.343)	p04 =	-0.000258	(-0.0003713, -0.0001448)
p11 =	0.00931	(-0.04111, 0.05973	p50 =	5.21e-06	(-4.329e-06, 1.475e-05)
p02 =	0.06086	(0.01548, 0.1062)	p41 =	-3.022e-06	(-2.022e-05, 1.418e-05)
p30 =	-0.002716	(-0.007832, 0.002401)	p32 =	1.319e-05	(-1.093e-05, 3.73e-05)
p21 =	0.0003805	(-0.006979, 0.00774)	p23 =	-4.006e-06	(-3.304e-05, 2.503e-05)
p12 =	-0.002349	(-0.01009, 0.005391)	p14 =	3.513e-06	(-1.646e-05, 2.348e-05)
p03 =	0.000149	(-0.006653, 0.006951)	p05 =	2.164e-07	(-1.381e-05, 1.425e-05)
p40 =	-6.47e-05	(-0.0001608, 3.139e-05)			

Table 6.7: Coefficients in milli Tesla and their 95% confidence bounds that differ from the original coefficients.

For the final results: Figure 6.14a shows that with angle= 70° the error decreases quickly within a few iterations then it grows again to approximately −0.26 on the logarithmic scale. The behaviour is similar to Figure 6.10c, but the reconstructed image is far better. It is reasonable close to the original image.

With angle = 40° (Figure 6.14b) and angle= 30° (Figure 6.14c) the error decreases up to a certain point. The smaller error when there are more rotations, as expected. The reconstructed image is close to perfect. The 'abnormal tissue' pixels (smaller details) are reconstructed and there is only a slight difference within the larger parts of tissue.

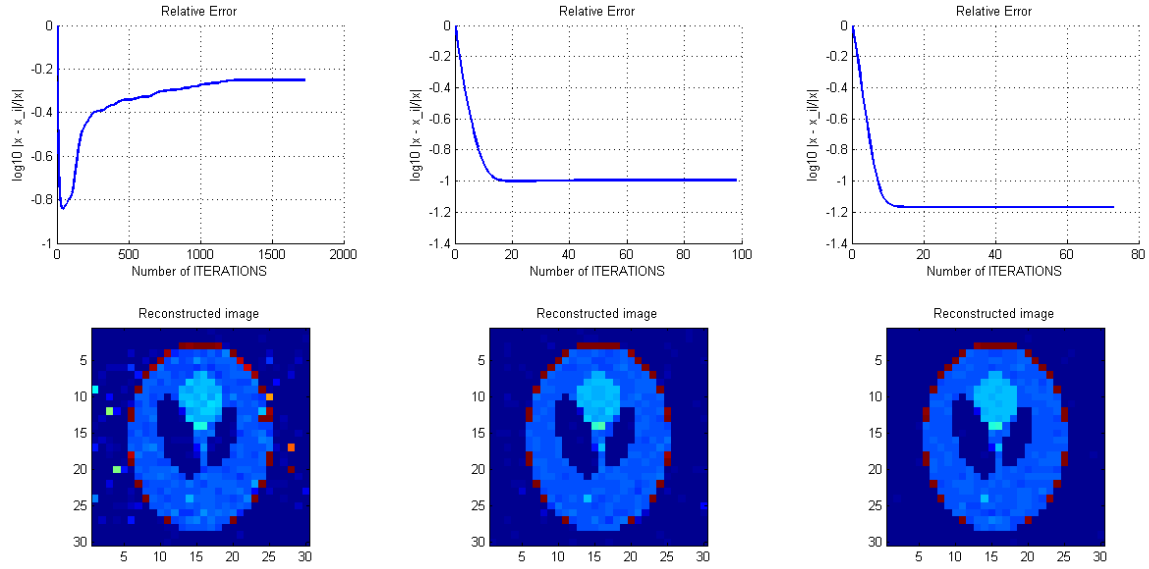

(a) angle= 70 (b) angle= 40° (c) angle= 30°

Figure 6.14: Results with a 0.01 mT perturbation using CGLS,freq= 12 MHz, bw= 3 MHz

In conclusion, an error in the order of 10^{-2} mT can be corrected for. An error in the order of 1 mT cannot. An error in the order of 10^{-1} mT is debatable at this point. It depends strongly on the effects of the iterative solver and regularisation.

A technique should be developed that estimates the field and the image simultaneously. Another option is to use known images to estimate the field/parameters. Also, a measuring tool which measures 4 decimal places (0.4000 T) is preferred so that the number of rotations is minimised.

6.3. T_2 and T_2^* relaxation in the model

Considering all information in Subsection 3.5.3 leads to the conclusion that the equality in Equation (3.71) cannot be guaranteed to hold in this project. There is still the question of how to define ΔB_{inhom}, which will be an interesting point for future research.

6.3.1. The 'true' T_2 relaxation vs field inhomogeneities

The order of size of the 'true' T_2 relaxation and the T_2^* relaxation will be discussed to show that this model is definitely subject to large field inhomogeneities.

The true T_2 relaxation in milliseconds ranges from 50 to 500. Therefore $1/T_2$ lies between 2 and 20 Hz. The T_2' depends on ΔB_{inhom} which is not properly defined yet in this model. If it is defined as the average field strength difference between the pixel and its neighbouring pixels, then ΔB_{inhom} ranges from approximately $4.8873 \cdot 10^{-4}$ to $4.6135 \cdot 10^{-2}$ T, implying that $1/T_2'$ is between $2.0810 \cdot 10^4$ and $1.9644 \cdot 10^6$ Hz. A difference of 2 to 5 orders is the result. Therefore adding $1/T_2$ to $1/T_2'$ for T_2^* will not make much of a difference. This shows that the inhomogeneities in the field play a considerable large part that cannot be ignored when the model is updated to fit reality closer.

One of the problems with using T_2^* is that, because of the fast signal decay, there are very few time samples large enough for use (about 15 time samples). Hence, there is little amount of information in the system.

7

Results

Chapter 6 discussed some issues concerning the model's Matlab program. No further changes are made to the model, even though the Matlab program can still be improved in many ways. In this chapter the iterative solvers from Chapter 4 are used on the model and the results are discussed.

7.1. Comparison of iterative solvers CGLS and CGNE without noise

As described in Chapter 4 CGLS should minimise the residual norm and CGNE should minimise the error. In this section this will be explored. For the runs in this section we kept the following variables the same:

noise	0	bw	3	epsilon	1e-8	N	1000	lambda	0
nrofpixels	30	angles	70	t	1e-4	freq	12	dt	1e-7

Figure 7.1 consists of three plots and three images. The plots show (from left to right) the relative residual norm, relative residual norm of the normal equations and the relative error for CGLS (blue) and CGNE (red). The images show (from left to right) the original image, the image acquired using CGLS and the image acquired using CGNE.

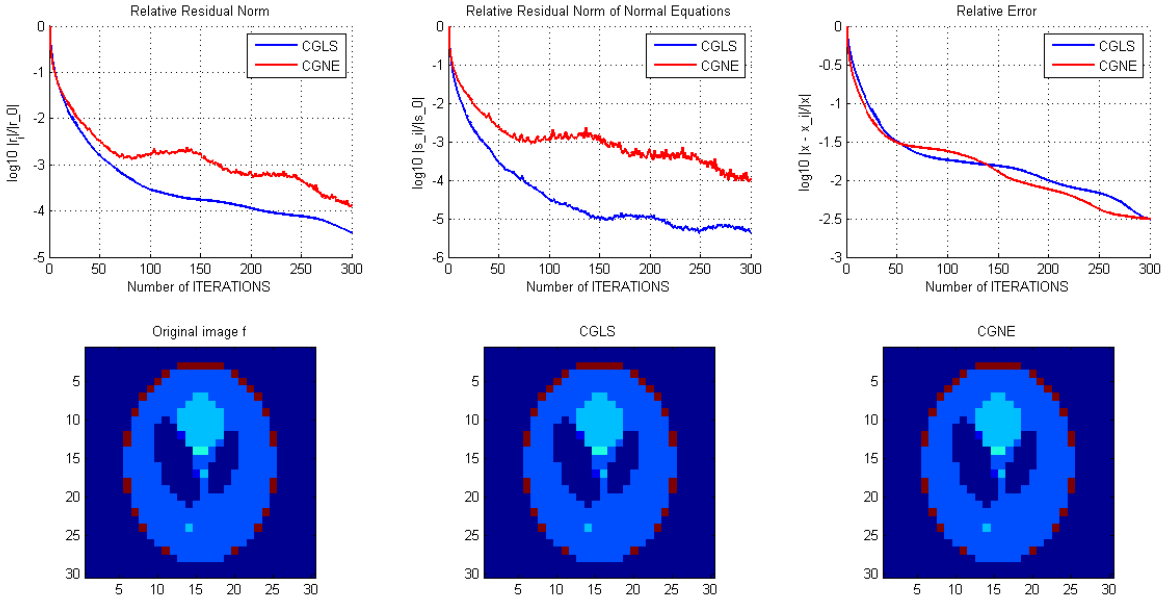

Figure 7.1: Comparison of CGLS and CGNE without noise, using 300 iterations and the variables stated above.

A limiting maximum number of iterations of 300 is used, but observe that the images from CGLS and CGNE are both a perfect reconstruction of the original image. The relative residual norm show convergent behaviour

for both CGLS and CGNE, but CGLS has a lower relative residual norm at all iterations as expected.

The relative error plot shows that CGNE has a lower relative error than CGLS until about 50 iterations. Then, until approximately 140 iterations, CGLS performs better but after 140 iterations CGNE does again. At 300 iterations the relative errors are roughly the same. We expect CGNE to have a lower relative error at every number of iterations. An explanation for the behaviour in this case is that it is the error compared to the model solution which is not necessarily the minumum norm solution.
From the middle plot it is visible that the stopping criterion of $\varepsilon = 10^{-8}$ has not been reached yet, therefore the program is run again with more iterations. It is then expected that the relative error will be lower for CGNE. Also, the relative residual norm of CGLS should stay lower than CGNE.

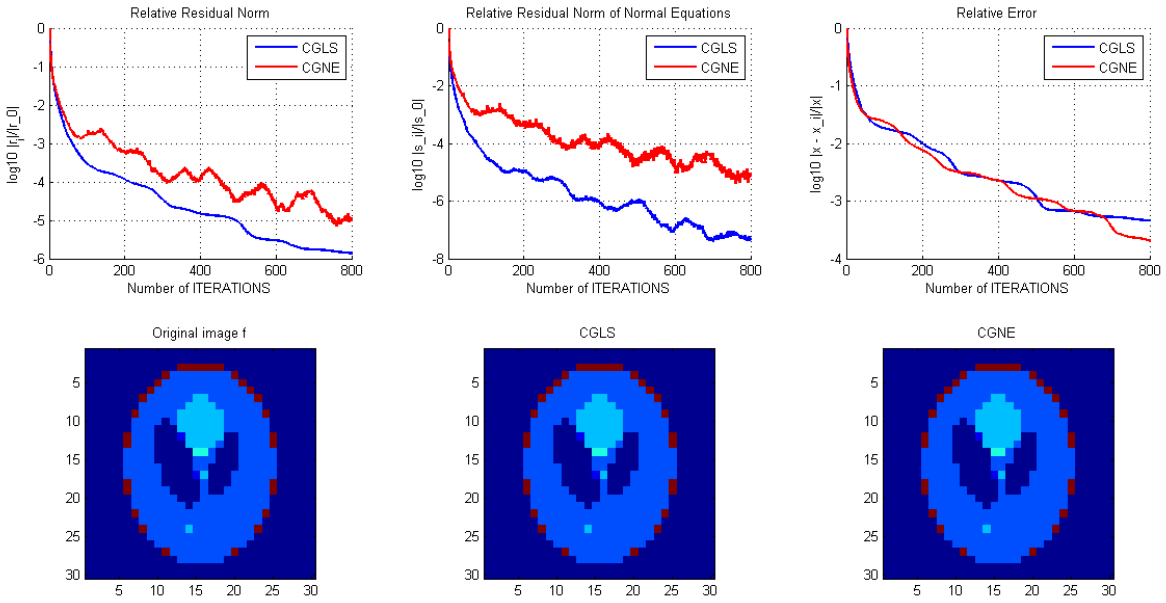

Figure 7.2: Comparison of CGLS and CGNE without noise, using 800 iterations and the variables stated above.

The results for 800 iterations are shown in Figure 7.2. From approximately 700 iterations, CGNE does have a lower relative error. Furthermore, if we put no limitation to the number of iterations CGNE needs more iterations (1586 compared to 922 of CGLS), the final relative error is much lower (see Appendix D.2). CGNE has a relative error of $0.3201 \cdot 10^{-5}$ (or -5.4947 on the logarithmic scale) compared to 0.0023 (or at -2.6332 on the logarithmic scale) of CGLS.
In conclusion, when no noise is present in the model, CGLS performs better with respect to the relative residual norm but CGNE performs better with respect to the relative error.

7.2. Comparison of iterative solvers CGLS and CGNE with noise

For the next comparison between the reconstructive algorithms we include noise. The noise is complex white noise and practically speaking a noise level of approximately 5% on top of the signal is realistic. Therefore the cases of 1%, 5% and 10% are discussed. For the runs in this section we kept the following variables the same:

`noise*`	0.01/0.05/0.1	`bw`	3	`epsilon`	1e-8	`N`	1000	`lambda`	0
`nrofpixels`	30	`angles`	70	`t`	1e-4	`freq`	12	`dt`	1e-7

*The noise variable is kept the same *in* each subsection, but is different *for* each subsection.

7.2.1. Noise level of 1%

Figure 7.3 shows the results for 800 iterations. Note that the stopping criterion of $\varepsilon = 10^{-8}$ has not yet been reached. Nevertheless, the relative residual norm of CGLS seems to converge to -2.0356 on the logarithmic

scale, which is equal to 0.0092. The relative error of CGLS shows semiconvergent behaviour. The corresponding image has a few pixels with a slightly wrong value, but the overal reconstructed image still resembles the original image.

For CGNE the reconstruction fails completely. This is backed by the fact that the relative error explodes and the relative residual norm also still increases after 800 iterations.

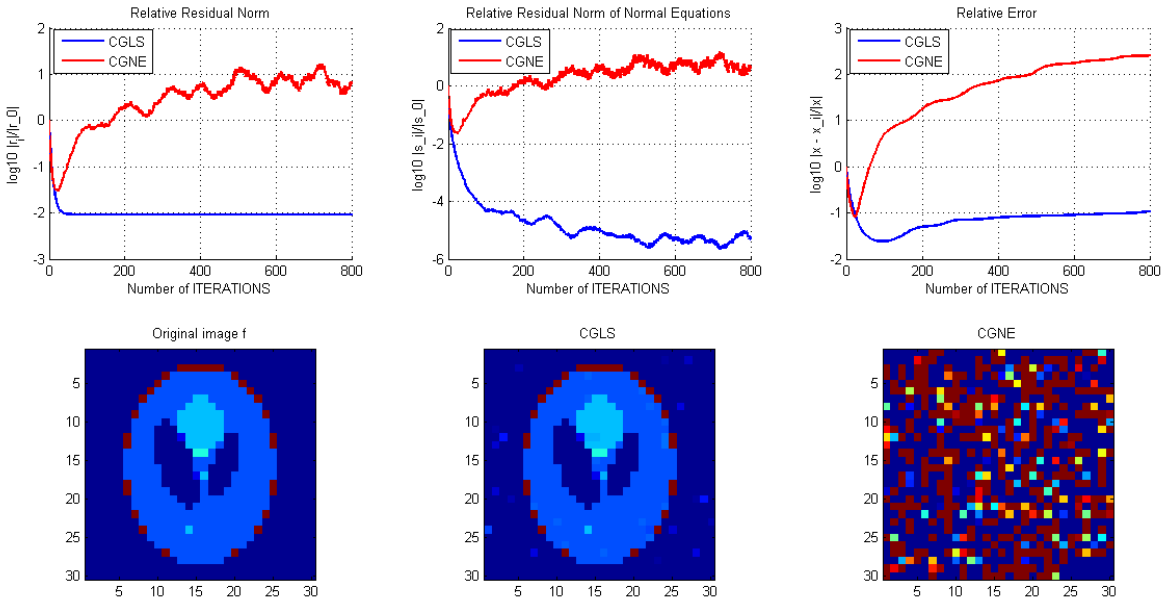

Figure 7.3: Comparison of CGLS and CGNE with 1% noise, using 800 iterations and the variables stated above.

At approximately 25 iterations, CGNE seems to have the 'best' solution. At this point the image still resembles the original image, but because of the divergent behaviour this is eventually lost. The reason we do not want CGNE to be used at 25 iterations is because of the divergent behavious as well as the fact that CGLS still has a decreasing relative residual norm, relative residual norm on normal equations and decreasing relative error. Therefore CGLS with slightly more iterations is preferred.

7.2.2. Noise level of 5%

The results for the noise level of 5% are given in Figure 7.4 for 300 iterations. The two main observations are that CGLS still works and, as can expected with a *higher noise level*, CGNE fails. The relative residual norm of CGLS still converges, but now to -1.3373 on the logarithmic scale, which equals 0.0460.

The relative residual norm has already converged at about 25 iterations for CGLS, the lowest relative error seems to be at 50 iterations. Even though the relative residual norm of the normal equations is not as low at 50 iterations, it is an interesting point to look at. The results at 50 iterations are shown in Figure 7.5.

Now compare the reconstructed image using CGLS for 50 and 300 iterations (Figures 7.5 and 7.4). At 300 iterations several pixels have a very different value than they should, especially outside the 'head'. At 50 iterations these very different values are gone, however there are more pixels that are slightly off the correct value.

Note that for the first 6 iterations the relative residual norm of CGNE is lower than that of CGLS. We have not yet found an explanation for this unexpected behaviour.

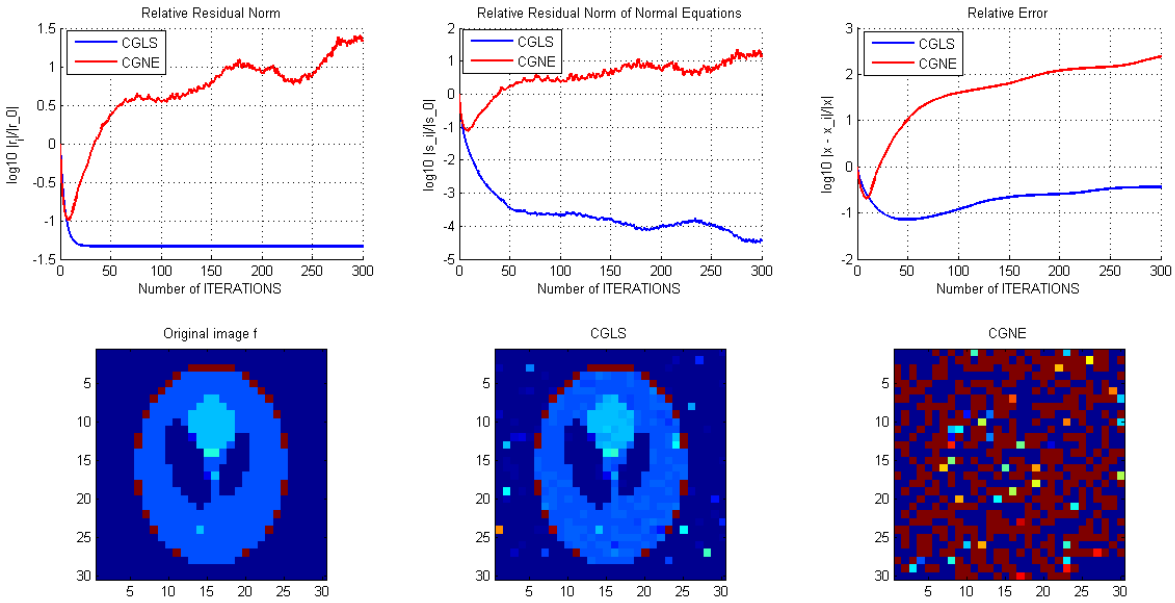

Figure 7.4: Comparison of CGLS and CGNE with 5% noise, using 300 iterations and the variables stated above.

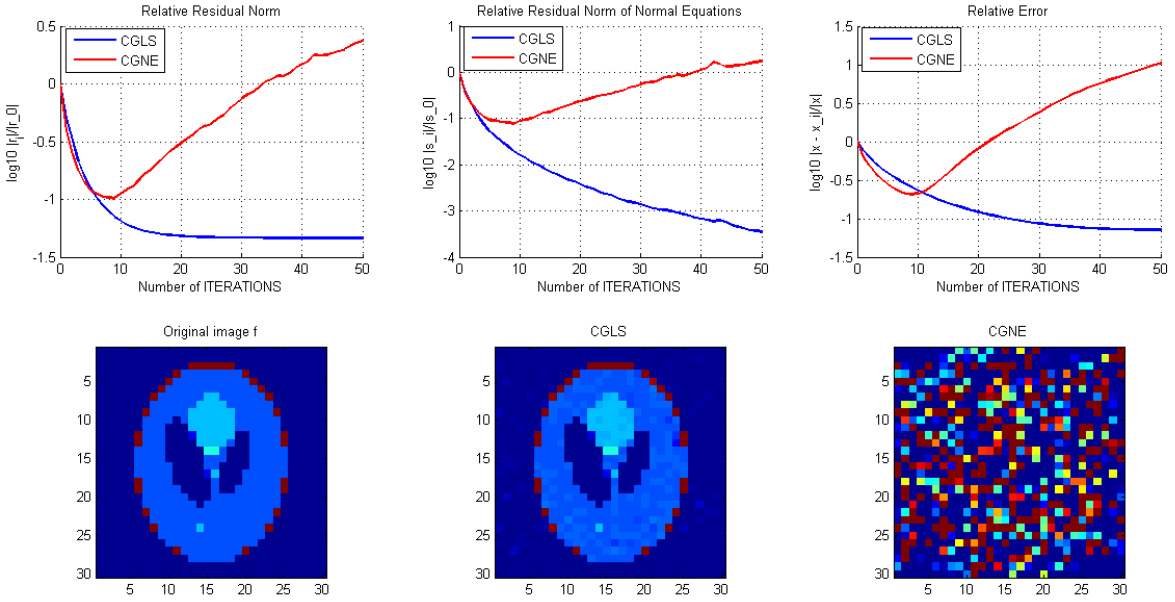

Figure 7.5: Comparison of CGLS and CGNE with 5% noise, using 50 iterations and the variables stated above.

7.2.3. Noise level of 10%

In Figure 7.6 the results are given for 10% noise. The same conclusions can be made as in for the noise level of 5%:

- CGLS still seems to converge looking at the relative error and the reconstructed image.
- CGNE fails on both accounts.
- The relative residual norm of CGLS still converges, but now to -1.0380 on the log scale, which equals 0.0916.
- Again the results for about 50 iterations are shown (see Figure 7.7), which show a minimum in relative error for CGLS.

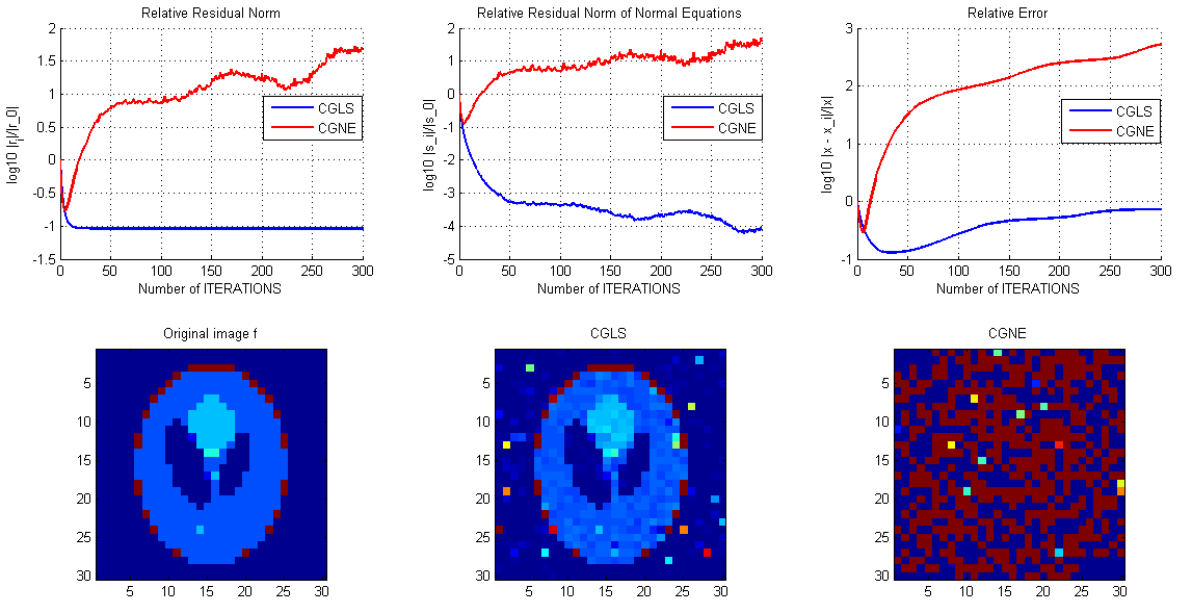

Figure 7.6: Comparison of CGLS and CGNE with 10% noise, using 300 iterations and the variables stated above.

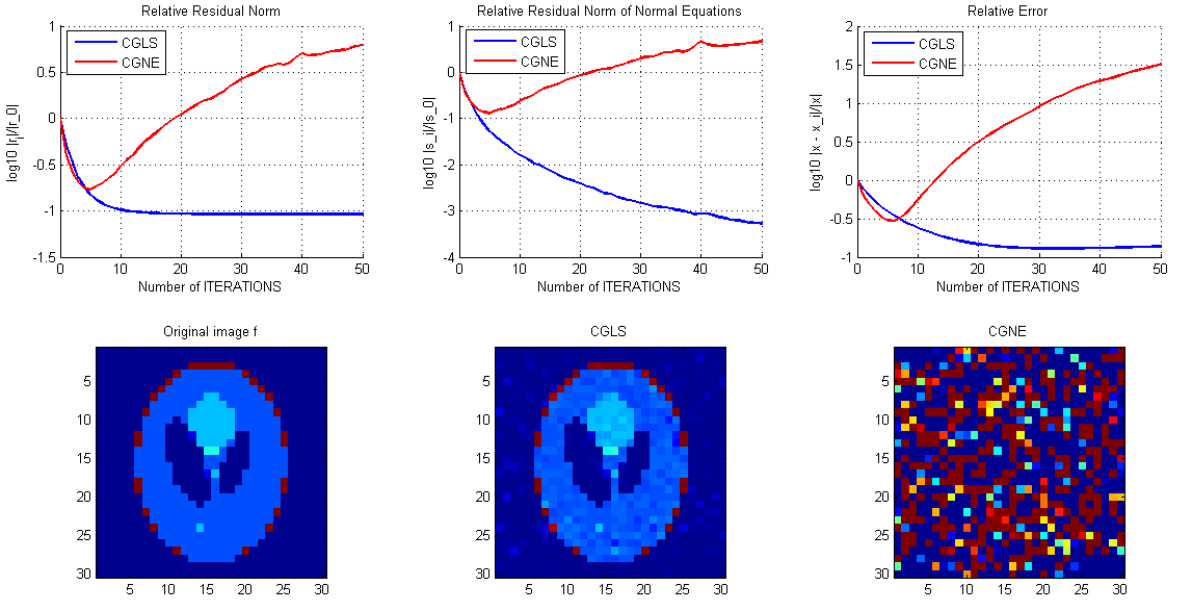

Figure 7.7: Comparison of CGLS and CGNE with 10% noise, using 500 iterations and the variables stated above.

Overall, we can conclude that CGNE does not work and we will not be considering CGNE in future research. Also CGLS shows semi-convergent behaviour for the chosen noise levels. This means at a few iterations the error is minimal then it increases again. The relative residual norm converges quickly as well
and an interesting observation is that the relative residal norm and the percentage of noise seem to be linear, see Figure 7.8.

7.3. Regularisation

Consider the three noise levels (1%, 5% and 10%) of the previous section again and consider CGLS only. It was concluded that for CGLS the relative error showed semi-convergent behaviour. This means that the most accurate picture (compared to the model solution and not the minimum norm solution) is at a low number

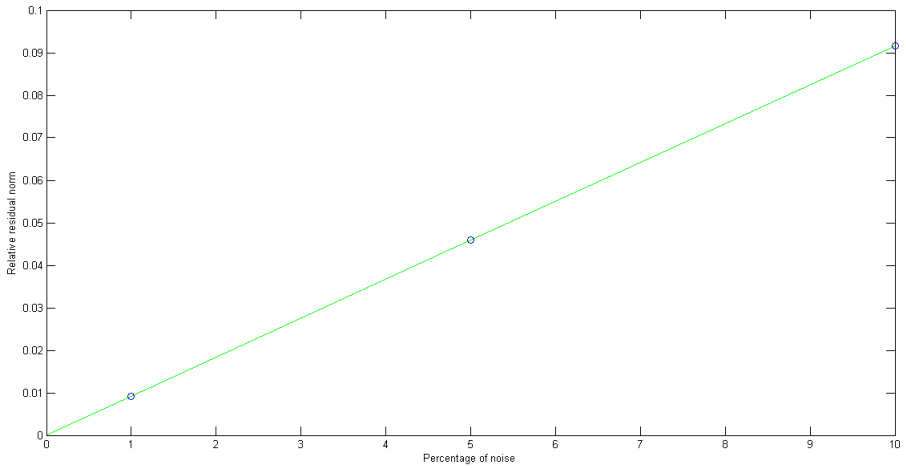

Figure 7.8: The relation between the percentage noise and the relative residual norm. The blue points are at 1% 0.0092, at 5% 0.0460 and at 10% 0.0916.

of iterations where the relative error is lowest before it increases again. In Figure 7.9 the relative errors for the three noise levels are plotted.

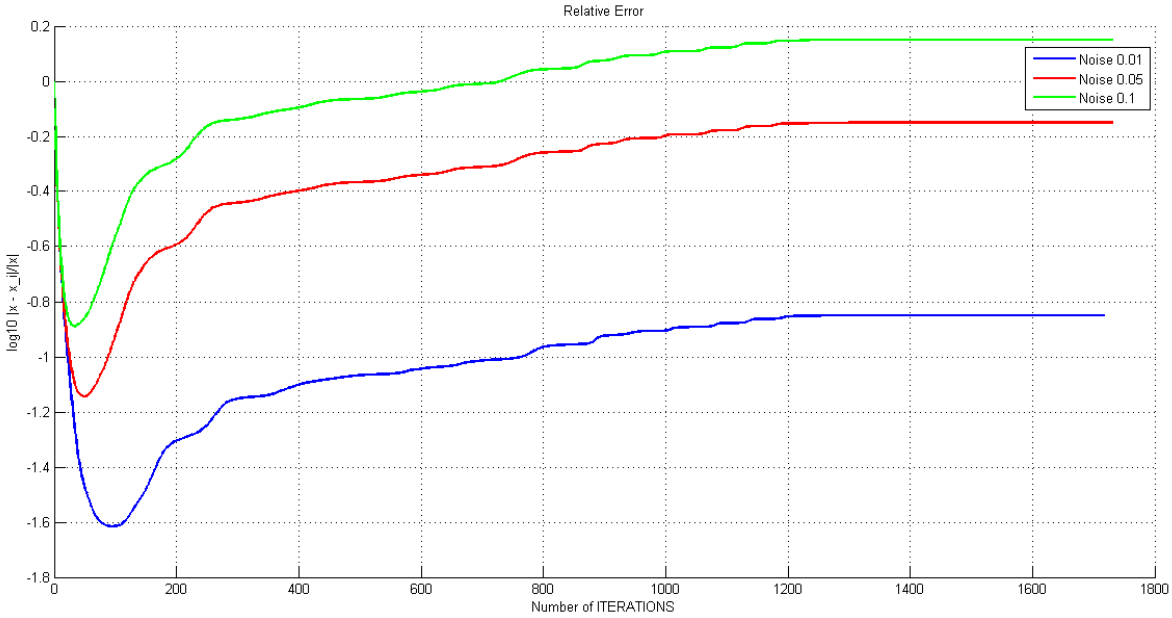

Figure 7.9: Relative errors with different percentages noise

It can not be read directly from this plot, but when zoomed in we find that the lowest relative errors for the different noise levels are:

Noise	iterations
1%	94
5%	49
10%	33

Table 7.1: The number of iterations with the lowest relative error for noise levels 1%, 5% and 10%.

The reconstructed images corresponding to these noise levels and number of iterations could be seen as a very simple sort of regularisation. The corresponding images are shown in Figure 7.10. The semi-convergent behaviour still exists but can change with regularisation. The difference between the images in Figure 7.10 and images at say 1600 iterations, is that with less iterations the images are more blurred and many pixels are slightly off the correct initial value, whereas at 1600 iterations there are a few pixels which are more off the correct initial value.

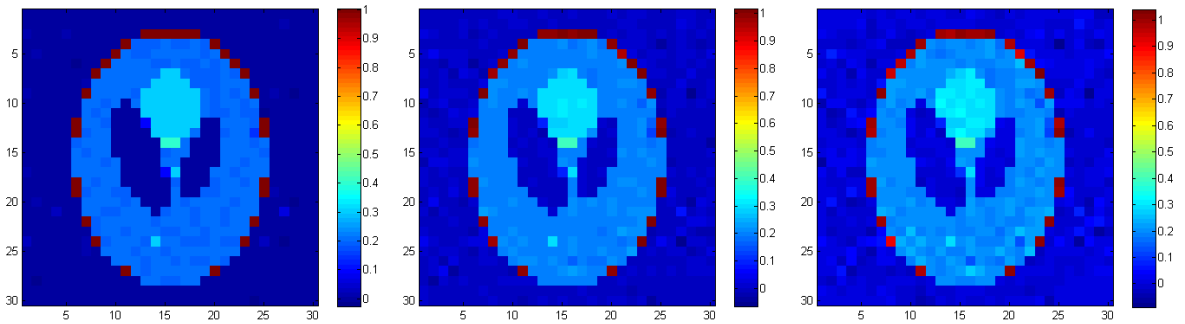

(a) Image using CGLS with 1% noise and 94 iterations.

(b) Image using CGLS with 5% noise and 49 iterations.

(c) Image using CGLS with 10% noise and 33 iterations.

Figure 7.10: Resulting images with 1%, 5% and 10% noise using CGLS and the number of iterations corresponding to the minimum relative error.

7.3.1. L-curve

As explained in Subsection 4.3.1, the optimal regularisation parameter λ needs to be found for the correct balance between the residual norm and the regularisaton matrix term norm. We will consider the case that the noise level is 5%. Because it is already quite accurate and we want to visualise the differences, lower numbers of rotations are used. Starting of with `angles` $= 140°$ (two rotations less than with `angles` $= 70°$) we have plotted the results for four different cases:

1. regularisation type 0: $L = I$,
2. regularisation type 0 with air constraint: $L = \begin{bmatrix} I & \text{constraint} \end{bmatrix}^T$,
3. regularisation type 1 with air constraint: $L = \begin{bmatrix} L_1 & \text{constraint} \end{bmatrix}^T$,
4. regularisation type 2 with air constraint: $L = \begin{bmatrix} L_2 & \text{constraint} \end{bmatrix}^T$,

where the air constraint is the a-priori information that the air pixels should have value 0. In other words, every location within the main magnet that does not contain tissue is air and this cannot change to tissue in the reconstruction.

Case 1 and 2 can be compared to see the effect of the extra constraint and case 2, 3, 4 can be compared to see the effect of different regularisation matrices. Let case 0 be the case without regularisation. The L-curve for the four cases above are shown in Figure 7.11. The norm $\|L\mathbf{x}_i\|_2$ is plotted against the residual norm $\|\mathbf{r}_i\|_2$ for 100 values of λ^2, logarithmically spaced between 10^{-2} and 10^{19}. The specific points of those λ^2 are not clear in this figure, because the scale is too large. This figure is merely to illustrate the shape of the L-curve for comparison to the theoretical L-curve in Figure 4.1.

The 'corner' of the L-curve is at approximately $\log_{10}(\|\mathbf{r}_i\|_2) = 8.25$ for all four cases. This is approximately the value which we we are interested in. The reason that the values of $\|L\mathbf{x}_i\|_2$ start of largest for case 4 and smallest for case 1 can be due to the fact that it is not the solution norm but the solution is multiplied by the regularisation matrix L. Figure 7.12 shows the zoomed in corner of the L-curve for all four cases. The spacing of λ^2 is now linear between 10^{13} and 10^{15} for 100 values. These are at every circle, star, square and diamond in the respective subplots.

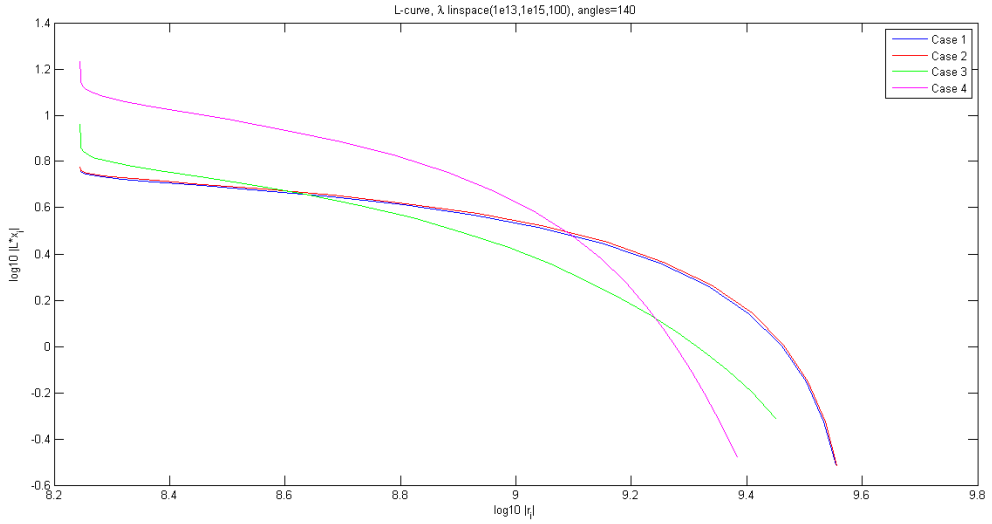

Figure 7.11: L-curve of cases 1 to 4, using angles= 140°, logspace(-2,19,100).

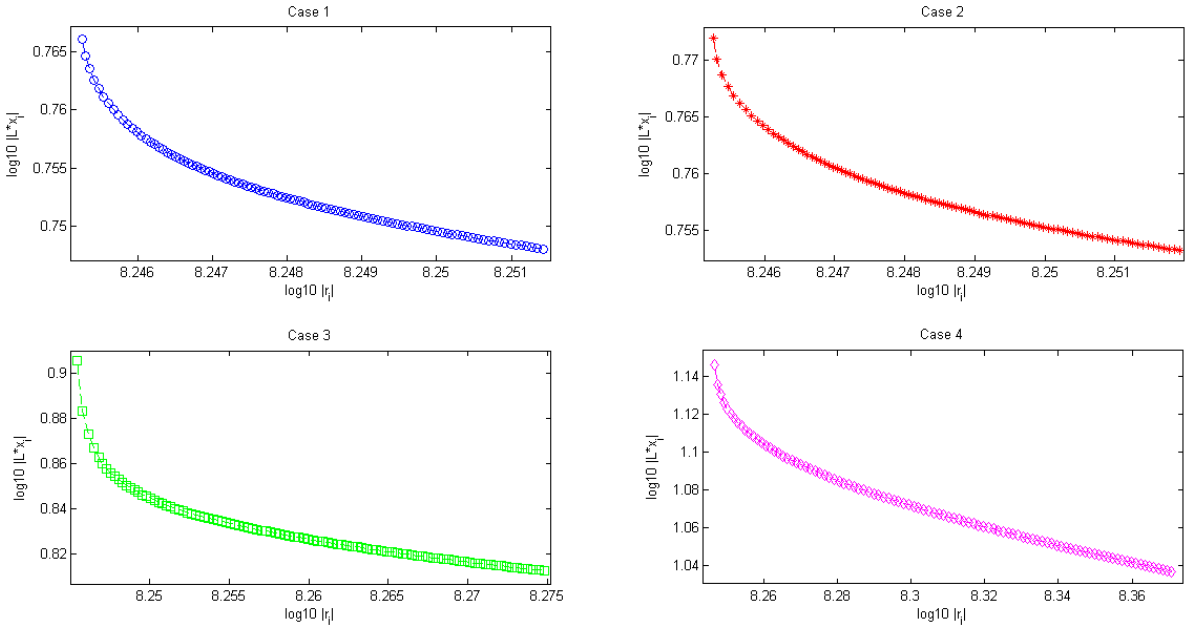

Figure 7.12: L-curve of cases 1 to 4, using angles= 140°, linspace(1e13,1e15,100).

The conclusion we have to make is that in many cases the results in practise do not match the theoretical expectation. The results do not show an L-curve shape and therefore no unique *optimal* value for regularisation parameter λ^2.
To compare results, parameter λ^2 has to be chosen. Choosing λ^2 the same for all cases can be the wrong approach as the L-curves all curve slightly different (even when zoomed to λ^2 between 10^{13} and 10^{15}). Therefore we will look at the λ^2 which belongs to the point where the decrease of $\|L\mathbf{x}_i\|_2$ is equal to the increase of the residual norm. For the angle between rotation of 140°, the λ^2's for cases 1 to 4 are

Case	λ^2
1	$9.604 \cdot 10^{14}$
2	$9.208 \cdot 10^{14}$
3	$6.931 \cdot 10^{14}$
4	$2.080 \cdot 10^{14}$

Table 7.2: The suboptimal regularisation parameter λ^2 for cases 1, 2, 3 and 4.

In Figure 7.13 the results for case 0, 1 and 2 are compared. Remember case 0 to be the model without regularisation, case 1 the model with regularisation without the extra constraint (so $L = I$) and case 2 the model with regularisation with the extra constraint (that states that the 'air' pixels should be zero).

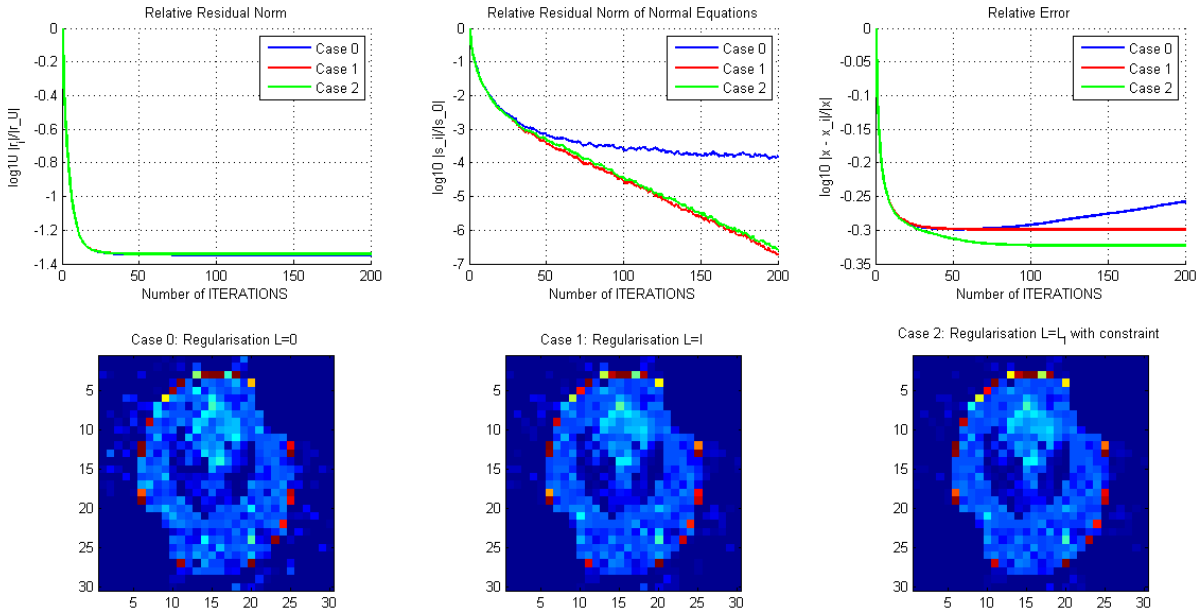

Figure 7.13: Result comparison for case 0, 1 and 2, using angles= 140°

First of all, adding regularisation results in a convergent behaviour of the relative error compared to the semi-convergent behaviour before. Secondly, even though it is not directly visible in the images for case 1 and case 2, we can conclude from the graph that adding the extra constraint results in a lower relative error. The relative errors are respectively $-2.9898 \cdot 10^{-1}$ and $-3.2298 \cdot 10^{-1}$. From the images can be seen that adding regularisation shows improvement. Especially the 'air' pixels show a more smoothed out background even though there are still some pixels with a lighter blue colour (rainbow colourbar, see Figure 5.1a).

For the second part we are comparing case 2, 3 and 4. Remember that for case 2 $\lambda^2 = 9.208 \cdot 10^{14}$, for case 3 it is $\lambda^2 = 6.931 \cdot 10^{14}$ and for case 4 it is $\lambda^2 = 2.080 \cdot 10^{14}$. Figure shows the results of the model for these cases and λ^2's.

The relative residual norm shows almost no differences. The relative error on the other hand shows that case 2 is more favourable than case 3 and 4 (which show similar relative errors with a semi-convergent behaviour). This behaviour could be due to a wrong choice of λ^2. In terms of the images we first note that in the image of case 2 the areas where there is no imaging information are visible (bottom left and top right). Using approximations of differential operators ($L = L_k$) seems to add information as these areas are less visible in the other two images. Case 3 shows blurring compared to case 2 which has more distinct pixels with values much different than should. In case 4 the blurring is because the transition from pixel to pixel is smoothed. Both case 3 and 4 show loss of image quality in important areas.

The information above as well as the results for the possible regularisation parameter λ^2 for `angles` 140° and 110° (one rotation more compared to the above) are summarised in Table 7.3.

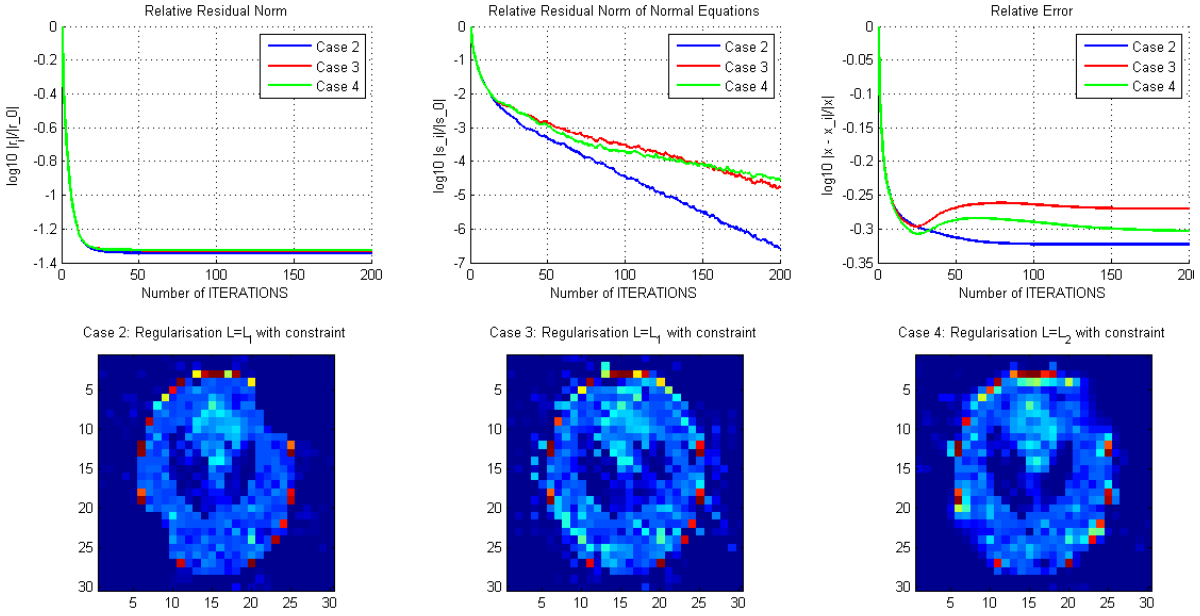

Figure 7.14: Result comparison for case 2, 3 and 4, using angles= 140°

Angle	λ^2 for Reg type 0	λ^2 for Reg type 0 with air constraint	λ^2 for Reg type 1 with air constraint	λ^2 for Reg type 2 with air constraint
110	$1.2988 \cdot 10^{15}$	$1.1989 \cdot 10^{15}$	$7.6240 \cdot 10^{14}$	$2.0800 \cdot 10^{14}$
140	$9.6040 \cdot 10^{14}$	$9.2080 \cdot 10^{14}$	$6.9310 \cdot 10^{14}$	$2.0800 \cdot 10^{14}$

Table 7.3: Guess to optimal λ^2 for angles= 110° and 140° for cases 1 to 4: type 0 ($L = I$), type 0 with air constraint, type 1($L = L_1$), type 2($L = L_2$). Number of iterations is 200 and number of pixels is 30, freq= 12 MHz, bw= 3 MHz.

7.4. p norm minimalisation

Subsection 4.2.3 discusses the idea behind using the p-norm. The system of equation $A\mathbf{x} = \mathbf{b}$ can be solved using the fixed-point iteration

$$\min_{\mathbf{x}_k} \|D_{k-1}\mathbf{x}_k\|_2^2 \quad \text{s.t. } A\mathbf{x}_k = \mathbf{b}. \tag{7.1}$$

Figure 7.15 shows the relative residual norm, relative residual norm of normal equations and the relative error for $p = 1, 1.1, 1.5$ and 1.7. The bottom row of Figure 7.15 shows the images corresponding to $p = 1, 1.1$ and 1.7. The relative error graph shows that the relative error is highest for $p = 1.7$ and lowest for $p = 1$ The relative error decreases when p decreases. On the other hand, the relative residual norm increases as p decreases. Observe that the images look more accurate as p decreases. This can be seen in both the air pixels and the scalp (turning more red on the colorbar when p decreases).
Note that choosing $p = 2$ results in CGLS. In combination with the results in Figure 7.15 it is clear that using a p between 1 and 2 can have better results. Therefore, let this short analysis serve for a starting point for a deeper analysis of the p-norm. In particular the 1-norm in combination with regularisation, which is not used in this analysis.

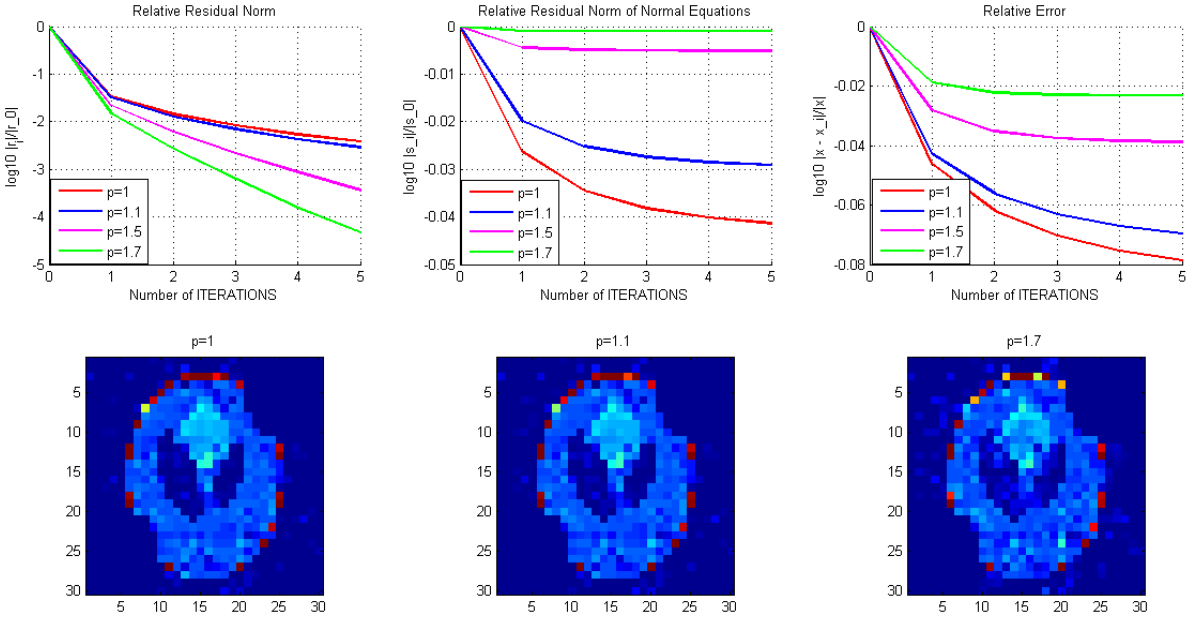

Figure 7.15: Results for different values of p, using angles= 140°, freq= 12 MHz, bw=3 MHz, noise= 5%, $\lambda = 0$, m_iter= 100, m_outer= 6.

8

Conclusions and future research

8.1. Conclusion

The goal of this project was to develop a sufficiently accurate image reconstruction algorithm that is able to effectively process signals produced by a low-cost portable MRI scanner. This goal has been partially achieved: We have derived a formula for the signal, turned it into a linear set of equations to solve. We have developed an image reconstruction technique (in 2D) using rotation of the main magnet and a broader frequency bandwidth.

The project posed a few challenges such as the Nyquist rate, the optimal number of rotations, the size of the frequency bandwidth and the influence of perturbations of the field.

The Nyquist rate has to be satisfied in order to correctly switch between a continuous and discrete signal. The difficulty lies in the fact that the Nyquist rate depends on the background field, but there were doubts about the accuracy of it. A stepsize of 10^{-7} has been used which covers the highest chosen frequency bandwidth of 3 MHz.

Using the effective rank the number of rotations has been analysed. Within a certain number of rotations, a few different angles between rotations can be chosen, however no distinct pattern has been found to select the optimal value of `angles`. Only the fact that using a divider of 360 as the angle between rotation has the lowest effective rank and should therefore be avoided. For 6 rotations `angles`= 70 is the best, for 5 rotations `angles` = 74, for 4 rotations `angles`= 110 and for 3 rotations `angles`= 147. Comparing the effective rank with the size of the bandwidth resulted in the use of a bandwidth of 3 MHz. With this bandiwdth and 3 rotations not the whole phantom image is covered. Also, the effective rank of 5 and 6 rotationsare both very high and differ only slightly, favouring 5 rotations because of MRI scanning time. A different approach showed that for this bandwidth the minimum number of rotations is 5, but in practice 4 rotations seemed to cover the phantom image as well. Therefore 4 or 5 rotations should be used with bandwidth 3 MHz. However, there are other factors to consider which could cause the result to differ from the results above because the model is not yet complete.

The measured values for the background field of the main model could contain errors because of the accuracy of the tool (order 10^{-1} mT) and human errors (order 1 mT). The first can be corrected for, but the latter can not be corrected for. Hence, perturbations in the field have a significant effect on the results. They can be slightly corrected with the use of a polynomial fit of higher order, but great care needs to be taken when measuring the field (or finding another technique to do so more accurately).

Because of the inhomogeinity of the field we have to deal with the so called T_2^* relatxation. Using T_2 or T_2^* also depends on the type of pulse sequence used. When using single of multiple spin echo pulse sequences, T_2 is considered and with GRE T_2^* is considered. Using T_2^* also has the downside of a fast decay which results in much less information in the system. A previous version of the model showed that only about 15 time samples out of 1000 were still usefull. Many open questions remain that are left for future research.

In the analysis for the iterative solvers it can be concluded that without noise CGLS and CGNE both work very well. When adding noise CGNE fails to work (even with 1%), where a noise level of 5% is realistic. In that case CGLS is semi-convergent and CGNE fails. The relative residual norm of CGLS still converges. The relative residual norm and the percentage of noise seem linear.

Introducing regularisation we have analysed the method Tikhonov with $L = I$ (case 1 without and case 2 with air constraint), $L = L_1$ (case 3), $L = L_2$ (case 4) and looked at the effect of the air constraint. An L-curve analysis resulted in no optimal λ as there is no clear L shape in the L-curve. The point where the decrease of $\|L\mathbf{x}_i\|_2$ is equal to the increase of $\|\mathbf{r}_i\|_2$ is considered for a suboptimal λ for comparison of the results of Tikhonov. For case 1 to 4 they were $9.604 \cdot 10^{14}$, $9.208 \cdot 10^{14}$, $6.931 \cdot 10^{14}$ and $2.080 \cdot 10^{14}$ respectively. The relative error (and relative residual norm) is lowest with $L = I$ and the extra air constraint and hence the best combination to use up to this point.

8.2. Recommendations for future research

In this thesis the focus was on setting up the program for the model. Throughout the months the model kept improving, but it is not yet finished. Therefore the results are intermediate results and more improvements still have to be made for it to fit reality. In this section some recommendations are given.

8.2.1. Analysis of selection methods

As mentioned in the research question 2, a combination of the method of rotating and the method of selecting different frequencies and/or bandwidths can be used. In this thesis only rotation is used and therefore the latter can still be research (in combination with rotation). Also the coil sensitivity can be implemented to give more information.

The frequency bandwidth selection is done with the TR (transmitter receiver) coil. In practical cases one can imagine that the accuracy of the TR coil is not perfect. This means that the selection in Figure 8.1a might not be realistic. The sensitivity/accuracy is equal to 1 within the bandwidth and zero outside the bandwidth. A more realistic option is that the sensitivity decreases gradually when further away from the bandwidth (see Figure 8.1b).

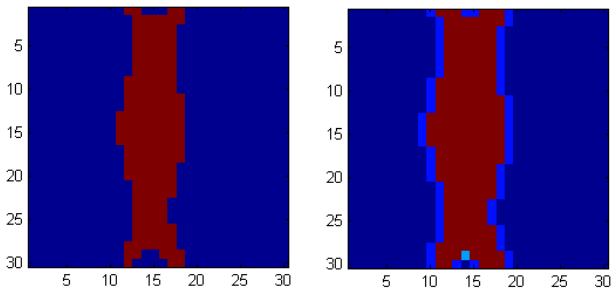

(a) Image reconstruction considering a perfectly accurate TR coil.

(b) Selection considering a more realistic accuracy of the TR coil.

Figure 8.1: Two selection methods showing the difference between perfect accuracy and a more realistic accuracy of the TR coil, using freq= 12 MHz, bw= 0.7 MHz.

In Subsection 6.1.2 it could be concluded that using a larger bandwidth resulted in a higher rank of the matrix and therefore the system contains more information. However, if the gradually decreasing accuracy is method 2 and the precise selection is method one, a question is which method results in more information in the system. Do let the selection from method one and the selection *plus* the gradually decreasing accuracy of method two select the same pixels.

There are definitely some advantages of using a smaller bandwidth. There is less amount of noise which is sampled due to the smaller frequency range, resulting in a higher SNR (signal to noise ratio). For more information see [11].

Another unanswered question is part of research question 2. There the option of combining two selection methods is described. It combines the current method of rotation with the method of selecting different frequency bandwidths. With the rotating method, one frequency band is selected at approximately the center of the magnet, but there are many other options.

8.2.2. Implementing a method with T_2

If for intermediate results the T_2 relaxation has to be used, or it turns out that the pulse sequence of T_2 is preferred, some changes need to be made to the model. T_2 is present in the signal, but is unknown in the image reconstruction (known in A, but unknown in say A_{rec}). However, T_2 is considered known in this thesis. To include T_2 in the model a loop can be inserted around the program and smartly let the computer appoint the T_2 values. This way we iterate over T_2 and it should be getting closer to reality.
This can be done as follows

1. Run reconstruction programme with T_2 a vector of ones.
2. Appoint T_2 values corresponding to the pixel value of the solution.
3. Re-evaluate matrix A_{rec} with the above values for T_2.
4. Repeat until reconstructed image is acceptable.

8.2.3. From 2D to 3D

In this thesis the object that is imaged is considered 2D, however when the model works in 2D the step to 3D has to be made. This research step has already been started and was presented at a conference. article conference 2D to 3D (Portable Imaging with Rotating Inhomogeneous Magnetic Fields by Clarissa Zimmerman Cooley):
“For 3D imaging, encoding is needed along the axis of the cylinder as well. Transmit Array Spatial Encoding (TRASE) is a complementary, $\mathbf{B}_1$ imaging method, that can be used for 1D encoding in the Y- direction of the described scanner. To enable TRASE encoding in the inhomogeneous magnetic field, broadband WURST pulses were used. The combination of the rotating SEM method for 2D encoding and the TRASE method for 3rd axis encoding, enables a 3D imaging method in the portable scanner" [9].

8.2.4. Other suggestions for future work

Other suggestions for future work are stated below.

- Fit the COMSOL model better to reality and use for validation.
- Research if rotating up to 180° is more favourable compared to rotating up to 360° because of the symmetry found in the inhomogeneous background field.
- Implement T_2^*.
- When it comes to experiments, the measured field has to be as accurate as possible to use it to the Matlab model. A technique to do this can be developed.
- The ratio of the size of the head versus the magnet can be researched. Right now the TR coil fits roughly around a humans little finger. This is a small area compared to the magnet. What is a realistic ratio considering the variations in the background field?

A

Glossary

A.1. Acronyms

Abbreviation	Abbreviation meaning
CG	Conjugate Gradient
CGLS	Conjugate Gradient Least Squares
CGNE	Conjugate Gradient Normal Error
CGNR	Conjugate Gradient Normal Residual
CSF	Cerebrospinal Fluid
CT	Computer Tomography
FFT	Fast Fourier Transform
FID	Free Induction Decay
GRE	Gradient Echo
HPD	Hermitian Positive Definite
LUMC	Leiden University Medical Center
MRI	Magnetic Resonance Imaging
NaN	Not a Number
RF	Radio Frequency
RMSE	Root Mean Square Error
SNR	Signal to Noise Ratio
SPD	Symmetric Positive Definite
SSE	Sum of Squared Error
SVD	Singular Value Decomposition
TE	Echo time
TR	Receiving time
TR coil	Transmitter Receiver coil
TSE	Turbo Spin Echo

A.2. List of symbols

Symbol	Units	Quantity
$\mathbf{A}$	Vsm^{-1}	magnetic vector potential
$\mathbf{B}$	T	magnetic flux density field
$\mathbf{B}_1$	T	oscillating field (i.e. RF pulse)
$\mathbf{H}$	A/m	magnetic field intensity
$\mathbf{J}$	T	angular momentum
$\mathbf{M}$	A/m	magnetisation field
$\mathbf{f}$	1	image vector
$\mathbf{p}$	1	update vector
$\mathbf{r}$	1	residual vector
$\mathbf{r}$	1	spatial location (x, y, z)
$\mathbf{x}_*$	1	real solution
$\mathbf{y}$	1	discrete signal vector
A / A_{rec}	1	system matrix for image reconstruction
B_0	T	constant background magnetic field strength
B_k	T	magnetic field in the k-direction.
$B_{r,xy}$	T	detection sensitivity of the receiver coil (* implies polar form)
D	1	weightmatrix p-normalisation
I	1	image from standard MRI reconstruction
L	1	regularisation matrix Tikhonov
M_z^0	T	thermal equilibrium
M_+^0	T	$M_x^0 + \mathrm{i}M_y^0$
M_{eq}	T	equilibrium magnetisation
M_{xy}	T	magnetisation in transverse plane standard MRI
$M_\perp$	T	magnetisation in transverse plane
$S(t)$	s	continuous signal
T_1	s	spin-lattice (longitudinal) relaxation time
T_2	s	spin-spin (transversal) relaxation time
T_2^*	s	effective relaxation time
U	1	eigenvectors of AA^*
V	1	eigenvectors of A^*A
W	1	matrix with singular values of A on diagonal

Symbol	Units	Quantity
angles	°	angle between rotations
bw	MHz	frequency bandwidth
f_s	Hz	sample frequency
f_0	Hz	highest frequency
freq	MHz	center frequency Matlab
m_iter	1	number of iterations
nrofpixels	1	number of pixels high/wide
n_p	1	total number of pixels
n_r	1	number of rotations
N	1	number of timesteps
ΔB_k	T	main magnetic field in the k direction
ΔB_{inhom}	T	magnetic field inhomogeneity across a voxel
$\Delta\omega$	Hz	precession frequency in rotating frame
$\mathbb{D}$	1	domain (inside magnet)
$\delta\omega$	Hz	frequency offset
$\mathscr{E}$	V	electromotive force
ϵ	1	stopping criterion
γ	Hz/T	gyromagnetic ratio
λ	1	regularisation parameter
m_I	1	magnetic quantum number
μ	Am^2	magnetic moment
μ_0	H/m	permeability
ω_0	rad/s	angular frequency
ϕ_e	°	initial phase shift caused by RF excitation
ϕ_r	°	reception phase angle
φ_0	1	angle when writing M_+^0 in polar form
σ_i	1	singular value i
t	s	time

B

Derivations in Chapter 3

B.1. Derivation of Equation (3.41)

$$\mathsf{Q} = \frac{1}{\sqrt{2}}\begin{bmatrix} 1 & 1 & 0 \\ -\mathrm{i} & \mathrm{i} & 0 \\ 0 & 0 & \sqrt{2} \end{bmatrix} \quad \Rightarrow \mathsf{Q}^* = \frac{1}{\sqrt{2}}\begin{bmatrix} 1 & \mathrm{i} & 0 \\ 1 & -\mathrm{i} & 0 \\ 0 & 0 & \sqrt{2} \end{bmatrix} \tag{B.1}$$

then

$$\begin{aligned} \mathsf{Q}^* e^{-\mathsf{B}^{\mathrm{rel}} t}\mathsf{m}^0 &= \frac{1}{\sqrt{2}}\begin{bmatrix} 1 & \mathrm{i} & 0 \\ 1 & -\mathrm{i} & 0 \\ 0 & 0 & \sqrt{2} \end{bmatrix}\begin{bmatrix} e^{-t/T_2} & 0 & 0 \\ 0 & e^{-t/T_2} & 0 \\ 0 & 0 & e^{-t/T_1} \end{bmatrix}\begin{bmatrix} M_x^0 \\ M_y^0 \\ M_z^0 \end{bmatrix} \\ &= \frac{1}{\sqrt{2}}\begin{bmatrix} e^{-t/T_2} & \mathrm{i}e^{-t/T_2} & 0 \\ e^{-t/T_2} & -\mathrm{i}e^{-t/T_2} & 0 \\ 0 & 0 & \sqrt{2}e^{-t/T_1} \end{bmatrix}\begin{bmatrix} M_x^0 \\ M_y^0 \\ M_z^0 \end{bmatrix} \\ &= \begin{bmatrix} \frac{1}{\sqrt{2}}e^{-t/T_2}\left(M_x^0 + \mathrm{i}M_y^0\right) \\ \frac{1}{\sqrt{2}}e^{-t/T_2}\left(M_x^0 - \mathrm{i}M_y^0\right) \\ e^{-t/T_1}M_z^0 \end{bmatrix} = \begin{bmatrix} \frac{1}{\sqrt{2}}e^{-t/T_2}M_+^0 \\ \frac{1}{\sqrt{2}}e^{-t/T_2}\overline{M_+^0} \\ e^{-t/T_1}M_z^0 \end{bmatrix} \end{aligned} \tag{B.2}$$

$$\begin{aligned} \mathsf{Q}\left(\mathsf{B}^{\mathrm{rel}} + \Lambda\right) &= \frac{1}{\sqrt{2}}\begin{bmatrix} 1 & 1 & 0 \\ -\mathrm{i} & \mathrm{i} & 0 \\ 0 & 0 & \sqrt{2} \end{bmatrix}\begin{bmatrix} \mathrm{i}\omega_0 + T_2^{-1} & 0 & 0 \\ 0 & -\mathrm{i}\omega_0 + T_2^{-1} & 0 \\ 0 & 0 & T_1^{-1} \end{bmatrix} \\ &= \begin{bmatrix} \frac{1}{\sqrt{2}}(T_2^{-1} + \mathrm{i}\omega_0) & \frac{1}{\sqrt{2}}(T_2^{-1} - \mathrm{i}\omega_0) & 0 \\ -\mathrm{i}\frac{1}{\sqrt{2}}(T_2^{-1} + \mathrm{i}\omega_0) & \mathrm{i}\frac{1}{\sqrt{2}}(T_2^{-1} - \mathrm{i}\omega_0) & 0 \\ 0 & 0 & T_1^{-1} \end{bmatrix} \end{aligned} \tag{B.3}$$

$$\begin{aligned} \mathsf{B}e^{-\mathsf{B}t}\mathsf{m}^0 &= \mathsf{Q}\left(\mathsf{B}^{\mathrm{rel}} + \Lambda\right)\begin{bmatrix} e^{-\mathrm{i}\omega_0 t} & 0 & 0 \\ 0 & e^{\mathrm{i}\omega_0 t} & 0 \\ 0 & 0 & 1 \end{bmatrix}\begin{bmatrix} \frac{1}{\sqrt{2}}e^{-t/T_2}M_+^0 \\ \frac{1}{\sqrt{2}}e^{-t/T_2}\overline{M_+^0} \\ e^{-t/T_1}M_z^0 \end{bmatrix} \\ &= \begin{bmatrix} \frac{1}{\sqrt{2}}e^{-\mathrm{i}\omega_0 t}(T_2^{-1} + \mathrm{i}\omega_0) & \frac{1}{\sqrt{2}}e^{\mathrm{i}\omega_0 t}(T_2^{-1} - \mathrm{i}\omega_0) & 0 \\ -\mathrm{i}\frac{1}{\sqrt{2}}e^{-\mathrm{i}\omega_0 t}(T_2^{-1} + \mathrm{i}\omega_0) & \mathrm{i}\frac{1}{\sqrt{2}}e^{\mathrm{i}\omega_0 t}(T_2^{-1} - \mathrm{i}\omega_0) & 0 \\ 0 & 0 & T_1^{-1} \end{bmatrix}\begin{bmatrix} \frac{1}{\sqrt{2}}e^{-t/T_2}M_+^0 \\ \frac{1}{\sqrt{2}}e^{-t/T_2}\overline{M_+^0} \\ e^{-t/T_1}M_z^0 \end{bmatrix} \\ &= \begin{bmatrix} \frac{1}{2}e^{-\mathrm{i}\omega_0 t}e^{-t/T_2}(T_2^{-1} + \mathrm{i}\omega_0)M_+^0 + \frac{1}{2}e^{\mathrm{i}\omega_0 t}e^{-t/T_2}(T_2^{-1} - \mathrm{i}\omega_0)\overline{M_+^0} \\ -\mathrm{i}\frac{1}{2}e^{-\mathrm{i}\omega_0 t}e^{-t/T_2}(T_2^{-1} + \mathrm{i}\omega_0)M_+^0 + \mathrm{i}\frac{1}{2}e^{\mathrm{i}\omega_0 t}e^{-t/T_2}(T_2^{-1} - \mathrm{i}\omega_0)\overline{M_+^0} \\ e^{-t/T_1}T_1^{-1}M_z^0 \end{bmatrix} \end{aligned} \tag{B.4}$$

Now using the rule $\mathrm{Re}(z) = \frac{z+\bar{z}}{2}$ and $\mathrm{Im}(z) = \frac{z-\bar{z}}{2\mathrm{i}}$, Equation B.4 can be rewritten to a simpler form

$$\begin{bmatrix} \mathrm{Re}\left(e^{-\mathrm{i}\omega_0 t} e^{-t/T_2}(T_2^{-1}+\mathrm{i}\omega_0)M_+^0\right) \\ \mathrm{Im}\left(e^{-\mathrm{i}\omega_0 t} e^{-t/T_2}(T_2^{-1}+\mathrm{i}\omega_0)M_+^0\right) \\ e^{-t/T_1} T_1^{-1} M_z^0 \end{bmatrix} \tag{B.5}$$

B.2. Derivation of Equation (3.38) resulting in Equation (3.43)

Substitution gives

$$\partial_t \mathsf{m}(t) = \begin{bmatrix} -\mathrm{Re}\left(e^{-\mathrm{i}\omega_0 t} e^{-t/T_2}(T_2^{-1}+\mathrm{i}\omega_0)M_+^0\right) \\ -\mathrm{Im}\left(e^{-\mathrm{i}\omega_0 t} e^{-t/T_2}(T_2^{-1}+\mathrm{i}\omega_0)M_+^0\right) \\ T_1^{-1} e^{-t/T_1}\left(M^{eq} - M_0^z\right) \end{bmatrix} \tag{B.6}$$

and since $\omega_0 >> 1/T_1, 1/T_2$, the above simplifies to

$$\partial_t \mathsf{m}(t) = \begin{bmatrix} -\omega_0 e^{-t/T_2}\mathrm{Re}\left(\mathrm{i}e^{-\mathrm{i}\omega_0 t} M_+^0\right) \\ -\omega_0 e^{-t/T_2}\mathrm{Im}\left(\mathrm{i}e^{-\mathrm{i}\omega_0 t} M_+^0\right) \\ 0 \end{bmatrix} \tag{B.7}$$

Before rewriting further, note that $\mathsf{e}_1^T\mathsf{q}_1 = 1/\sqrt{2}$, $\mathsf{e}_2^T\mathsf{q}_1 = -\mathrm{i}/\sqrt{2}$ and $\mathsf{e}_3^T\mathsf{q}_1 = 0$. Also that $-\mathrm{Im}(z) = \mathrm{Re}(\mathrm{i}z)$. Then

$$\begin{aligned} \partial_t \mathsf{m}(t) &= \begin{bmatrix} -\omega_0 e^{-t/T_2}\mathrm{Re}\left(\mathrm{i}e^{-\mathrm{i}\omega_0 t} M_+^0\right) \\ \omega_0 e^{-t/T_2}\mathrm{Re}\left(\mathrm{i}\left(\mathrm{i}e^{-\mathrm{i}\omega_0 t} M_+^0\right)\right) \\ 0 \end{bmatrix} \\ &= \begin{bmatrix} -\omega_0 e^{-t/T_2}\mathrm{Re}\left(\left(\mathrm{i}e^{-\mathrm{i}\omega_0 t} M_+^0\right)\mathsf{e}_1^T\mathsf{q}_1\sqrt{2}\right) \\ \omega_0 e^{-t/T_2}\mathrm{Re}\left(-\mathsf{e}_2^T\mathsf{q}_1\sqrt{2}\left(\mathrm{i}e^{-\mathrm{i}\omega_0 t} M_+^0\right)\right) \\ 0 \end{bmatrix} \\ &= \begin{bmatrix} -\sqrt{2}\omega_0 e^{-t/T_2}\mathrm{Re}\left(\left(\mathrm{i}e^{-\mathrm{i}\omega_0 t} M_+^0\right)\mathsf{e}_1^T\mathsf{q}_1\right) \\ -\sqrt{2}\omega_0 e^{-t/T_2}\mathrm{Re}\left(\left(\mathrm{i}e^{-\mathrm{i}\omega_0 t} M_+^0\right)\mathsf{e}_2^T\mathsf{q}_1\right) \\ 0 \end{bmatrix} \\ &= \begin{bmatrix} -\sqrt{2}\omega_0 e^{-t/T_2}\mathrm{Re}\left(\mathrm{i}e^{-\mathrm{i}\omega_0 t} M_+^0\mathsf{e}_1^T\mathsf{q}_1\right) \\ -\sqrt{2}\omega_0 e^{-t/T_2}\mathrm{Re}\left(\left(\mathrm{i}e^{-\mathrm{i}\omega_0 t} M_+^0\right)\mathsf{e}_2^T\mathsf{q}_1\right) \\ -\sqrt{2}\omega_0 e^{-t/T_2}\mathrm{Re}\left(\left(\mathrm{i}e^{-\mathrm{i}\omega_0 t} M_+^0\right)\mathsf{e}_3^T\mathsf{q}_1\right) \end{bmatrix} \\ &= -\sqrt{2}\omega_0 e^{-t/T_2}\mathrm{Re}\left(\left(\mathrm{i}e^{-\mathrm{i}\omega_0 t} M_+^0\right)\mathsf{q}_1\right) \end{aligned} \tag{B.8}$$

B.3. Derivation of $\mathsf{w}^T\partial_t\mathsf{m}(t)$ resulting in Equation (3.50)

$$\begin{aligned} \mathsf{w}^T\partial_t\mathsf{m}(t) &\approx -\sqrt{2}e^{-t/T_2}|M_+^0|\mathrm{Re}\left[\mathrm{i}\omega_0 e^{-\mathrm{i}(\omega_0 t-\varphi_0)}\mathsf{w}^T\mathsf{q}_1\right] \\ &= -e^{-t/T_2}|M_+^0|\mathrm{Re}\left[\mathrm{i}\omega_0 e^{-\mathrm{i}(\omega_0 t-\varphi_0)} B_\perp e^{-\mathrm{i}\theta_B}\right] \\ &= -e^{-t/T_2}|M_+^0|\omega_0 B_\perp \mathrm{Re}\left[\mathrm{i}e^{-\mathrm{i}(\omega_0 t-\varphi_0+\theta_B)}\right] \end{aligned} \tag{B.9}$$

Now let $\theta_B - \varphi_0 = \zeta$ and rewrite the exponential to sinusoids to be able to distinguish the real and imaginary parts more easily.

$$\begin{aligned} \mathsf{w}^T\partial_t\mathsf{m}(t) &= -e^{-t/T_2}|M_+^0|\omega_0 B_\perp \mathrm{Re}\left[\mathrm{i}e^{-\mathrm{i}(\omega_0 t+\zeta)}\right] \\ &= -e^{-t/T_2}|M_+^0|\omega_0 B_\perp \mathrm{Re}\left[\mathrm{i}\left(\cos(\omega_0 t+\zeta) - \mathrm{i}\sin(\omega_0 t+\zeta)\right)\right] \\ &= -e^{-t/T_2}|M_+^0|\omega_0 B_\perp \sin(\omega_0 t+\zeta) \end{aligned} \tag{B.10}$$

C

From real measurements of the field to full field in Matlab

In section 1.2.2 it is mentioned that the two methods for finding a full field the size of the chosen number of pixels are interpolation and fitting polynomial. In this chapter the differences and preference are treated.

C.1. Without rotation

In subfigure C.6a the field from interpolation without rotation is given and in subfigure C.5a the field from polynomial fitting.

Fitting a polynomial (using the Apps -> Curve Fitting Tool) can be done to a 5th order in the x and z directions:

$$\begin{aligned} f(z,x) = {} & p_{00} + p_{10}z + p_{01}x + p_{20}z^2 + p_{11}zx + p_{02}x^2 + p_{30}z^3 + p_{21}z^2x + p_{12}zx^2 \\ & + p_{03}x^3 + p_{40}z^4 + p_{31}z^3x + p_{22}z^2x^2 + p_{13}zx^3 + p_{04}x^4 + p_{50}z^5 + p_{41}z^4x \\ & + p_{32}z^3x^2 + p_{23}z^2x^3 + p_{14}zx^4 + p_{05}x^5 \end{aligned} \tag{C.1}$$

This results in the field strengths as depicted in Figure C.2 as a 3d plot. The same field is given as a contour plot in C.1 to show the field distribution and Figures C.4 and C.3 show the residuals in the x and z direction respectively.

The interpolation using Matlab is at most cubic, but is in essence a piecewise interpolation and will include the measured data points. The curve fitting tool fits a smooth polynomial to the measurment points, not necessarily including them. The 5th order curve fitting does work with 95% confidence bounds on the coefficients (see Table C.1). Some confidence bounds values are only about $1-10\%$ of the coefficient itself, however others can be much larger than the value itself (p_{01} has a value in the confidence bound almost 7 times its size). Knowing this, a choice has to be made in how trustworthy and accurate the measurements are. The fields without rotation of the interpolation method and polynomial fitting method are given in C.6a and C.5a respectively.

Some challenges concerning interpolation are as follows. The given measurement points are very few and might not be accurate. Also because of the circular form of the magnet, a square matrix has NaN where the magnet is. When using interpolation in Matlab, the NaNs are treated as 0. Therefore, that interpolated field is not a good model for the full field. Another consideration is then to ignore the outside values and *choose* the largest square area without NaNs. This gives extreme values of 0.28 mT to 0.33 mT (lowest and highest value of the colorbars in Figure C.6). This is very low compared to the extreme values of the field using polynomial curve fitting: 0.24 mT and 0.708 mT (lowest and highest value of the colorbars in Figure C.5). Especially the maximum value is about twice the value of the other. Note that this high value belongs to a part at the boundary and the yellowish green represents a value around 0.5 mT. It is expected that the field strength is

p_{00} =	281.7	(278.4, 285)	p_{31} =	0.0001312	(-4.256e-05, 0.000305)
p_{10} =	0.332	(-0.2934, 0.9574)	p_{22} =	0.001773	(0.001576, 0.001971)
p_{01} =	-0.1062	(-0.809, 0.5967)	p_{13} =	-0.0001029	(-0.0002818, 7.605e-05)
p_{20} =	0.3027	(0.2623, 0.343)	p_{04} =	-0.0002579	(-0.0003712, -0.0001447)
p_{11} =	0.00925	(-0.04116, 0.05966)	p_{50} =	5.205e-06	(-4.332e-06, 1.474e-05)
p_{02} =	0.06082	(0.01545, 0.1062)	p_{41} =	-2.996e-06	(-2.019e-05, 1.42e-05)
p_{30} =	-0.002713	(-0.007829, 0.002402)	p_{32} =	1.321e-05	(-1.09e-05, 3.732e-05)
p_{21} =	0.000373	(-0.006985, 0.007731)	p_{23} =	-4.003e-06	(-3.303e-05, 2.502e-05)
p_{12} =	-0.002354	(-0.01009, 0.005384)	p_{14} =	3.531e-06	(-1.644e-05, 2.35e-05)
p_{03} =	0.0001583	(-0.006642, 0.006959)	p_{05} =	1.99e-07	(-1.383e-05, 1.422e-05)
p_{40} =	-6.47e-05	(-0.0001608, 3.137e-05)			

Table C.1: Coefficients p_{00} to p_{05} in millitesla and their 95% confidence bounds)

more diverse when using the polynomial. The field selected with the interpolation method is already chosen smaller, whereas the polynomial method uses the whole set of measurement points.

C.2. With rotation

Firstly, the rotated fields of both methods are shown in Figure C.5 and C.6. Using the interpolation of a square area without NaNs then faces another challenge. When the field is rotated around its center(which is done with Matlabs imrotate), some outside pixels are set to zero. In Figure C.6 this happens in subfigures C.6b, C.6c, C.6e, C.6f, C.6h, C.6i, C.6k, C.6l. This may cause problems with ΔB_z in the exponential in matrix A: that pixel will result in a $e^{-0} = 1$ instead of a decaying exponential.

To rotate the polynomial fitted field, the rotation matrix is used:

$$R(\theta) = \begin{bmatrix} \cos(\theta) & -\sin(\theta) \\ \sin(\theta) & \cos(\theta) \end{bmatrix} \tag{C.2}$$

So the coordinates (z',x') of the point (z,x) after rotation are

$$\begin{aligned} z' &= z\cos\theta - x\sin\theta \\ x' &= z\sin\theta + x\cos\theta. \end{aligned} \tag{C.3}$$

The field strength at the new coordinate (after rotation)can be found by finding the field corresponding to the old coordinate (before rotation). With this technique no pixel in a rotated frame will become 0 (unless the field strength itself is 0).

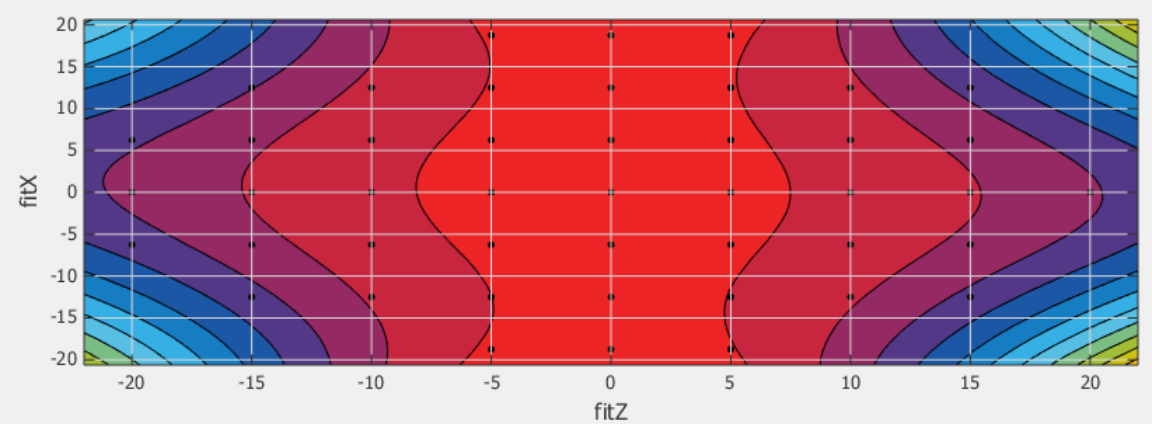

Figure C.1: Contour plot of the fitted polynomial

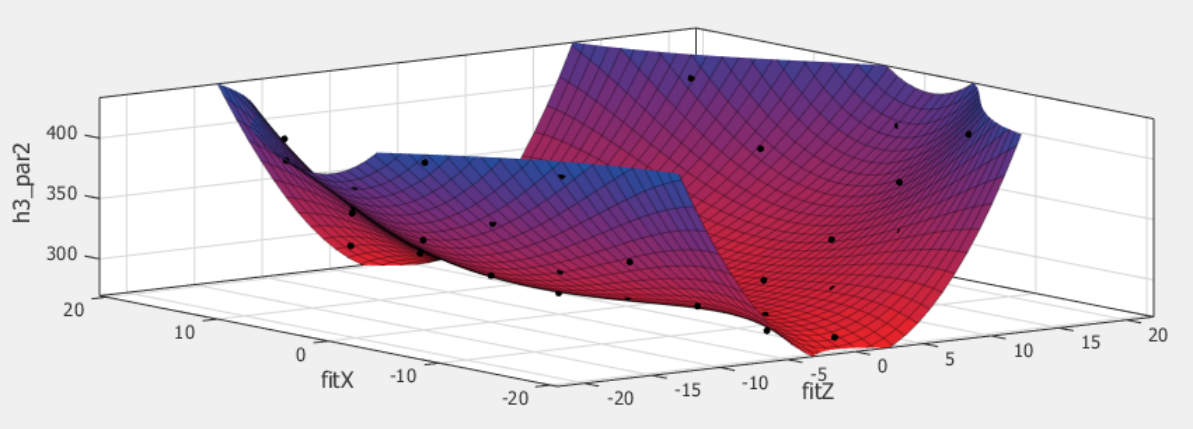

Figure C.2: 3D plot of the fitted polynomial, Goodness of fit information: SSE: 284, R-square: 0.9969, Adjusted R-square: 0.9944, RMSE: 3.44

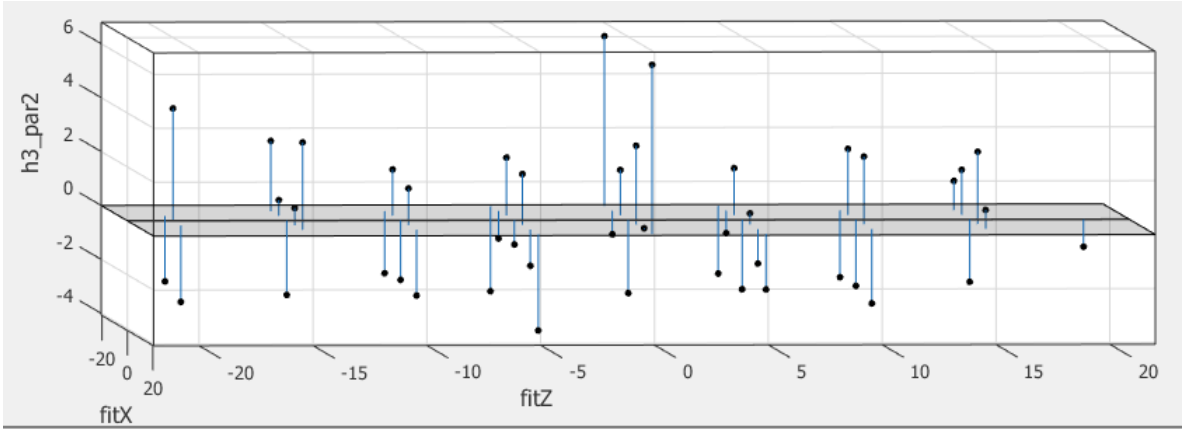

Figure C.3: Plot of the residuals in the z-direction

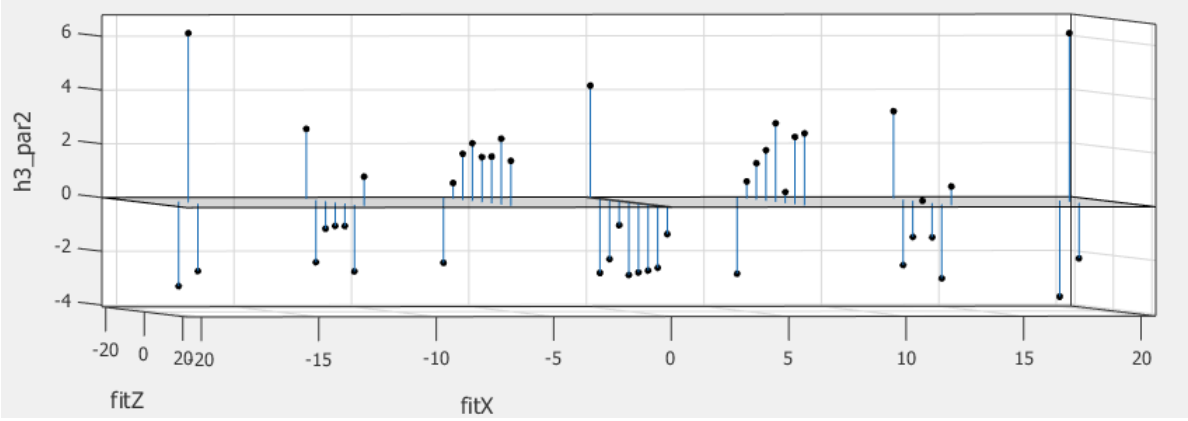

Figure C.4: Plot of the residuals in the x direction

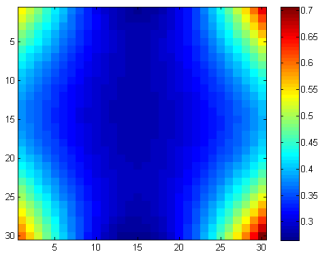

(a) Angle 1

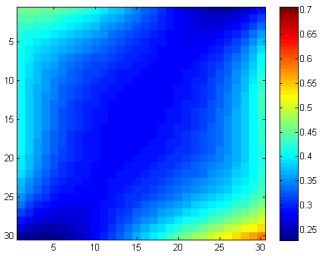

(b) Angle 2

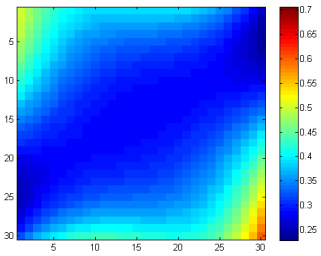

(c) Angle 3

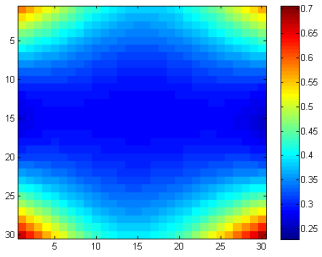

(d) Angle 4

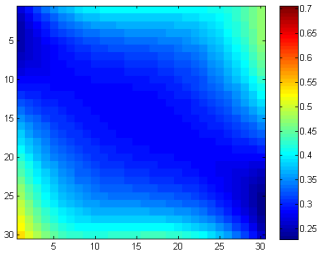

(e) Angle 5

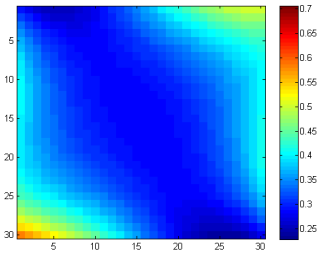

(f) Angle 6

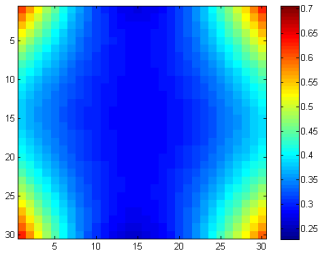

(g) Angle 7

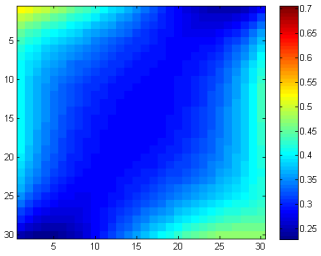

(h) Angle 8

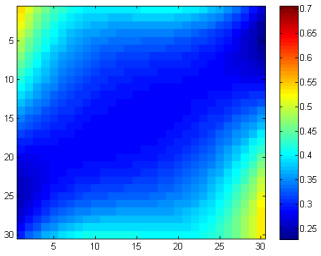

(i) Angle 9

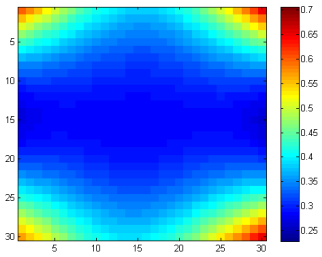

(j) Angle 10

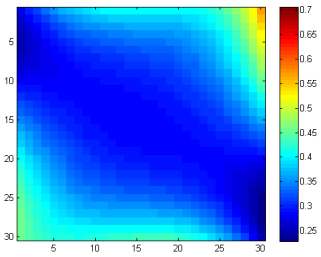

(k) Angle 11

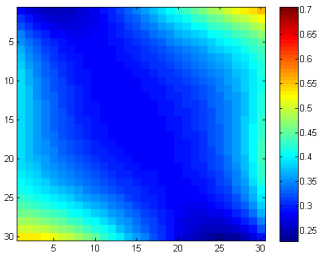

(l) Angle 12

Figure C.5: Full field (in mT) at different angles using the polynomial. 12 angles in total. Every 30 degrees. Rotation is clockwise.

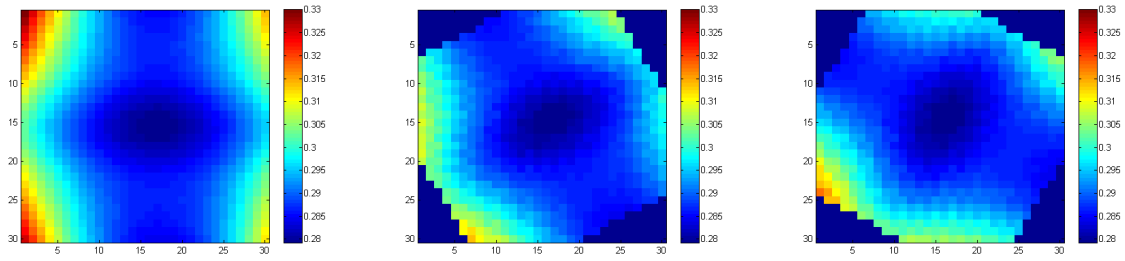

(a) Angle 1 (b) Angle 2 (c) Angle 3

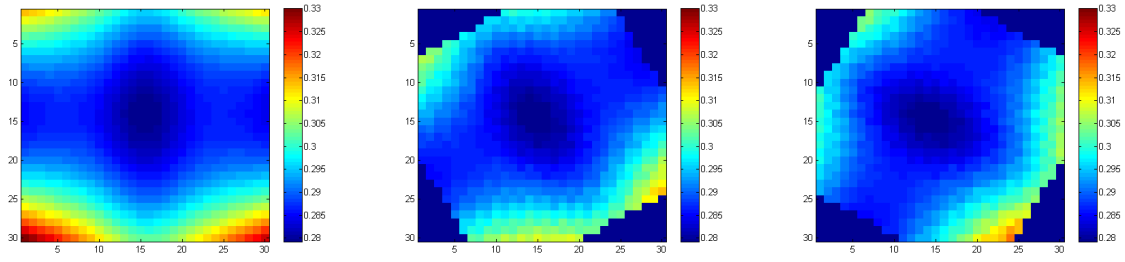

(d) Angle 4 (e) Angle 5 (f) Angle 6

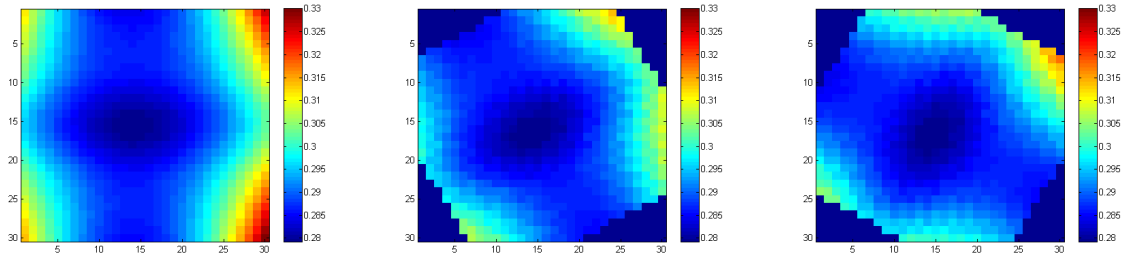

(g) Angle 7 (h) Angle 8 (i) Angle 9

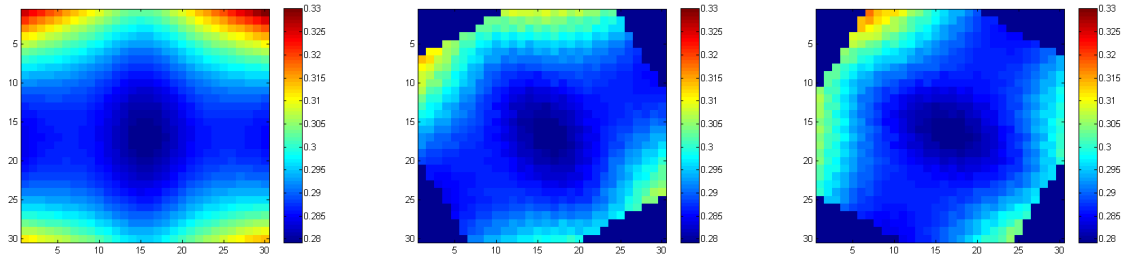

(j) Angle 10 (k) Angle 11 (l) Angle 12

Figure C.6: Full field (in mT) at different angles using the polynomial. 12 angles in total. Every 30 degrees. Rotation is anti clockwise.

D

Full result images

D.1. Perturbation analysis

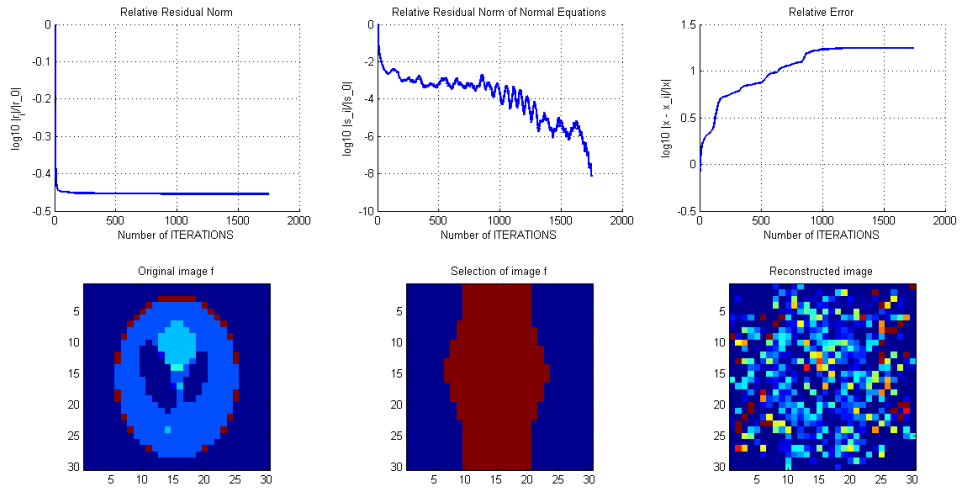

Figure D.1: Results with a 0.1 mT perturbation, angles= 70°, freq= 12 MHz, bw= 3 MHz.

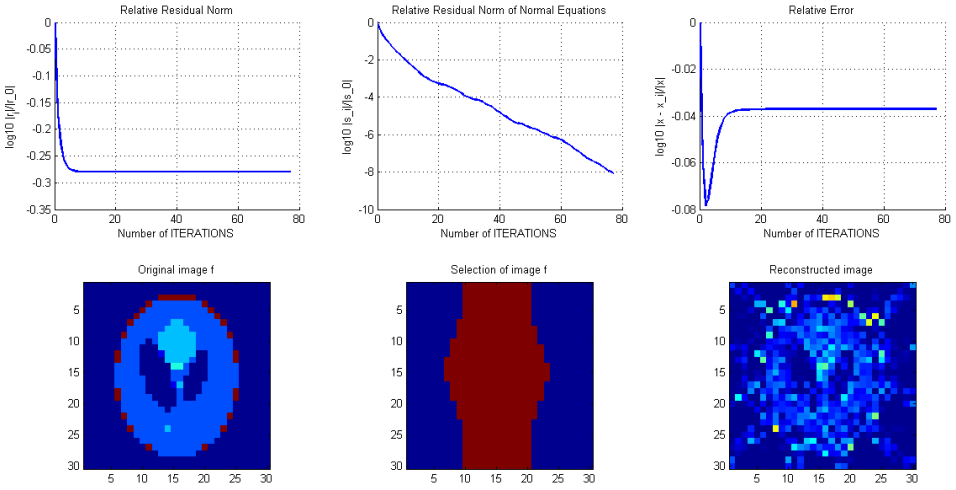

Figure D.2: Results with a 0.1 mT perturbation, angles= 30°, freq= 12 MHz, bw= 3 MHz.

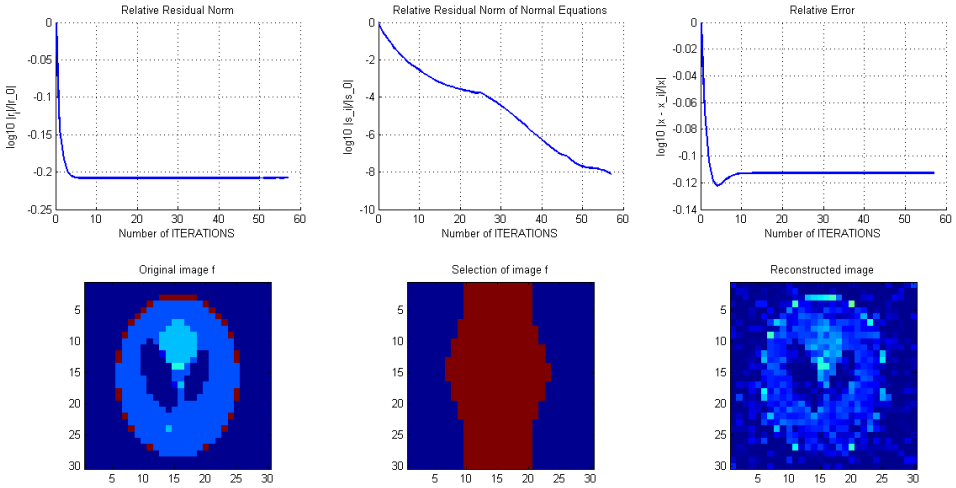

Figure D.3: Results with a 0.1 mT perturbation, angles= 10°, freq= 12 MHz, bw= 3 MHz.

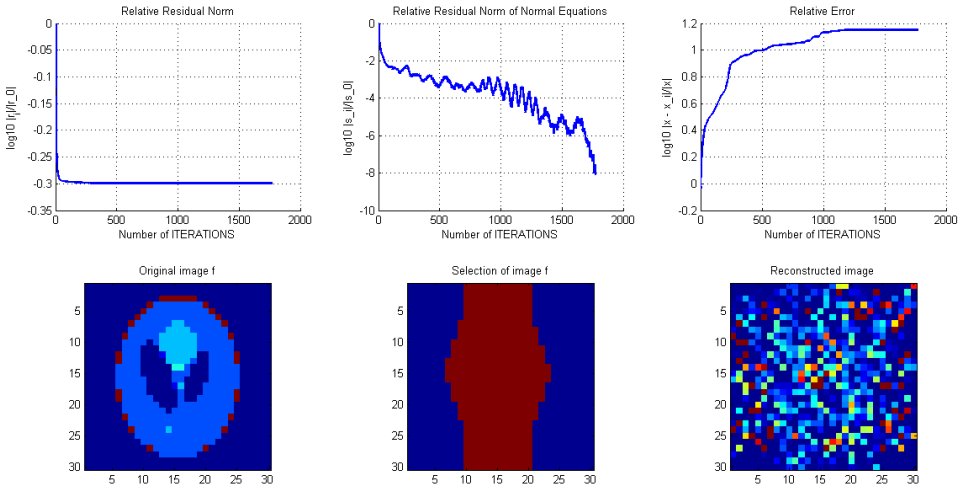

Figure D.4: Results with a 1 mT perturbation, angles= 70°, freq= 12 MHz, bw= 3 MHz.

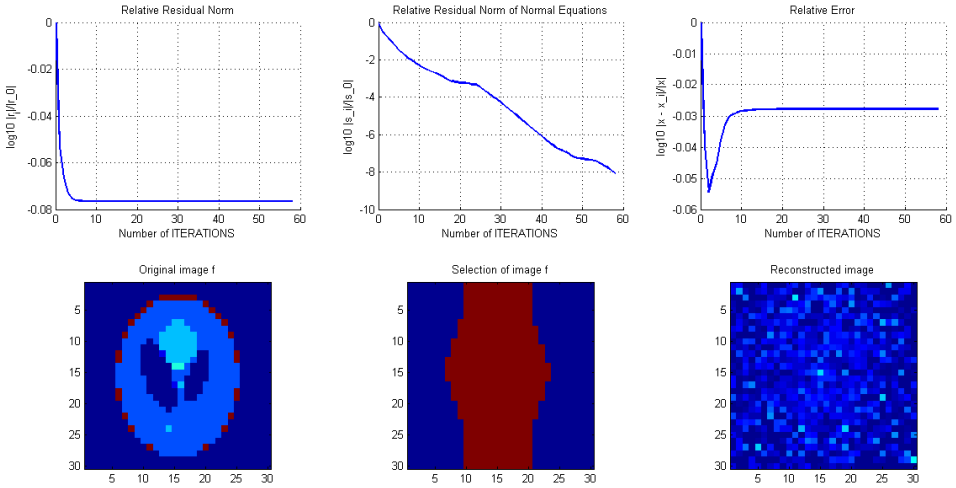

Figure D.5: Results with a 1 mT perturbation, angles= 10°, freq= 12 MHz, bw= 3 MHz.

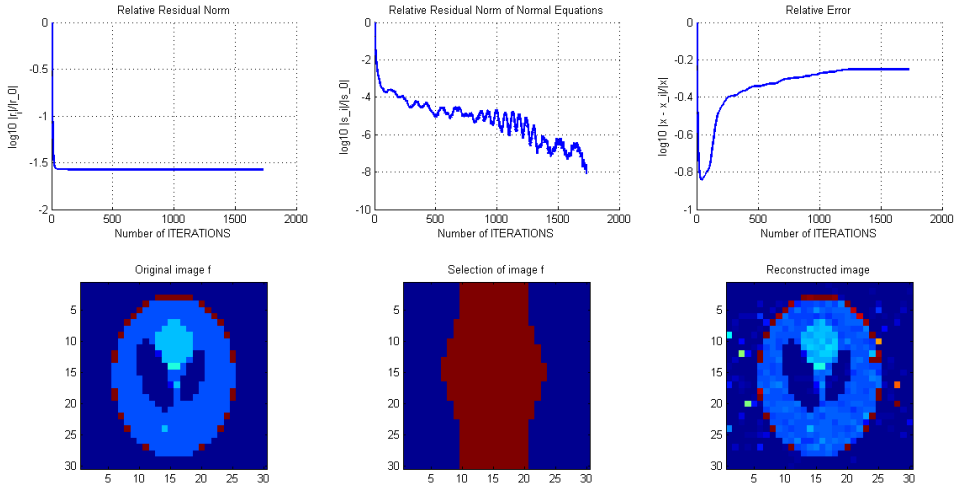

Figure D.6: Results with a 0.01 mT perturbation, angle= 70°, freq= 12 MHz, bw= 3 MHz.

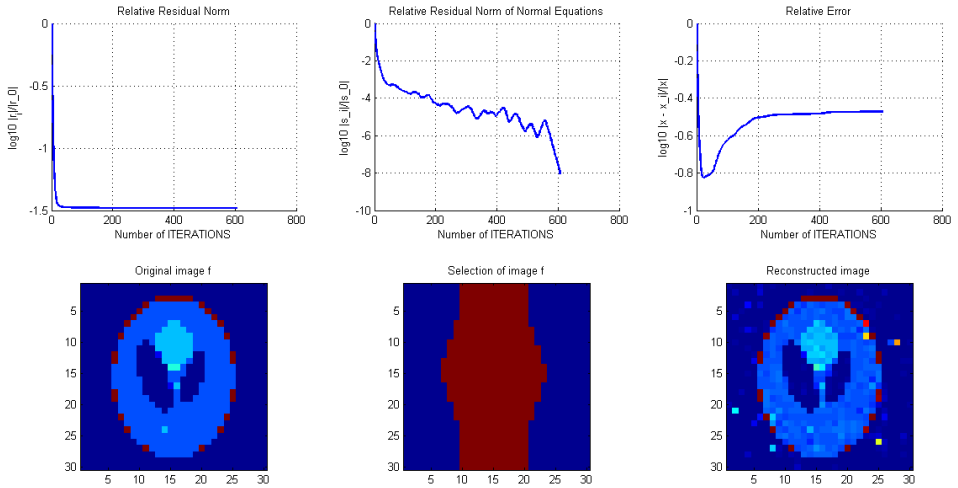

Figure D.7: Results with a 0.01 mT perturbation, angle= 55°, freq= 12 MHz, bw= 3 MHz.

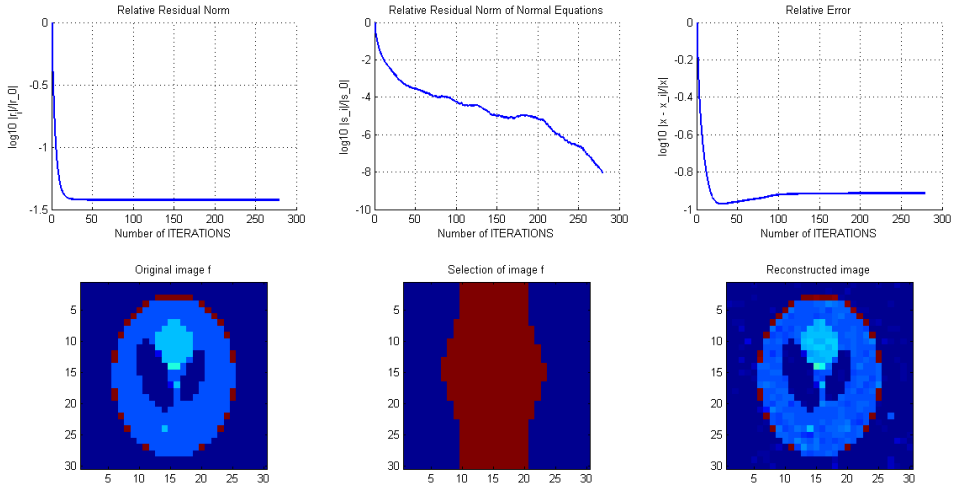

Figure D.8: Results with a 0.01 mT perturbation, angle= 48°, freq= 12 MHz, bw= 3 MHz.

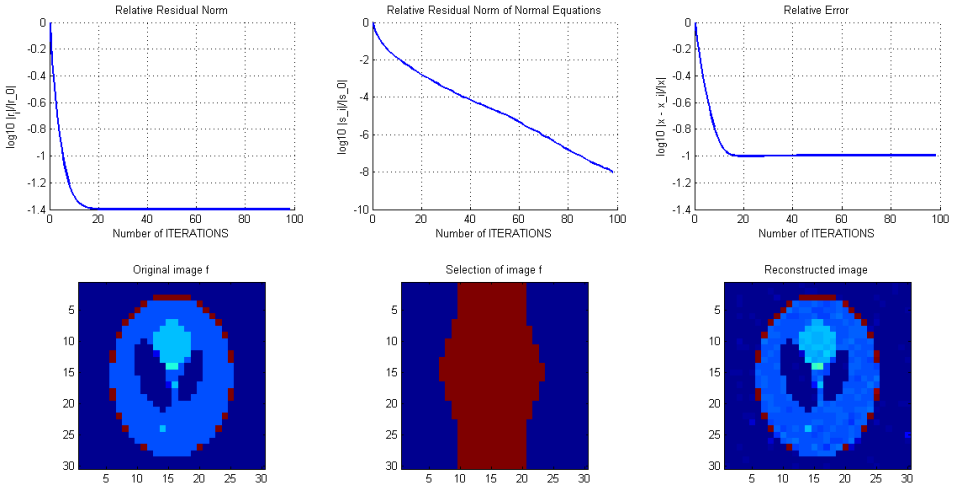

Figure D.9: Results with a 0.01 mT perturbation, angle= 40°, freq= 12 MHz, bw= 3 MHz.

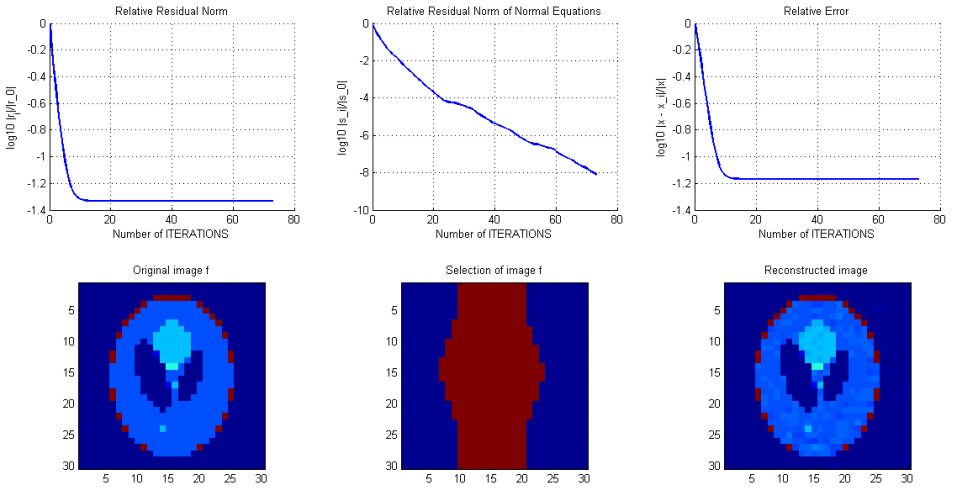

Figure D.10: Results with a 0.01 mT perturbation, angle= 30°, freq= 12 MHz, bw= 3 MHz.

D.2. Comparison of CGLS and CGNE

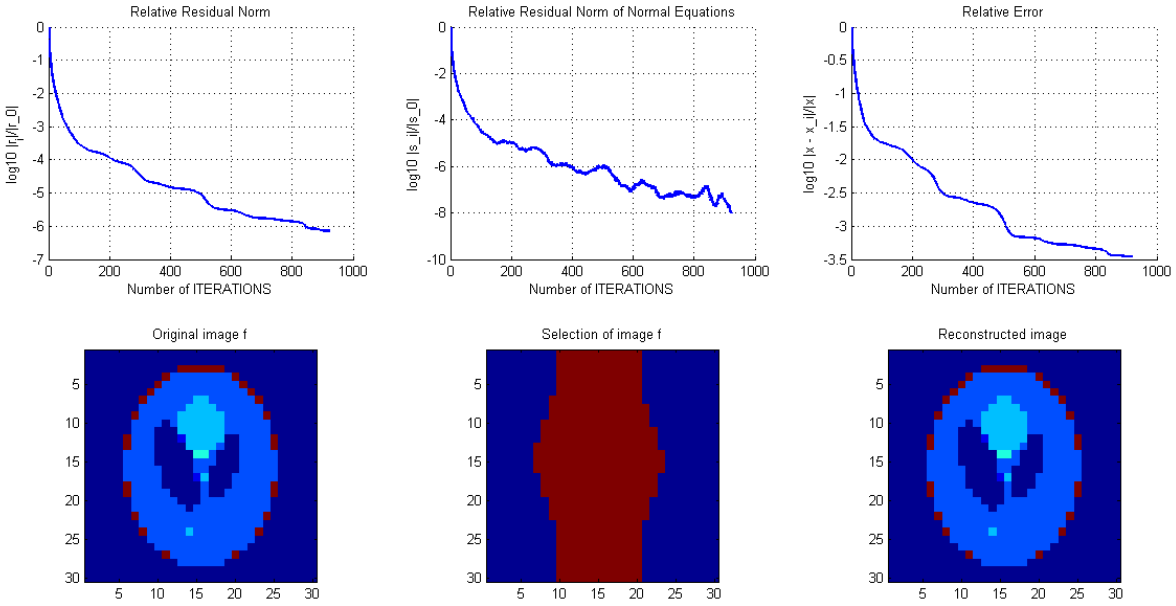

Figure D.11: Results of unlimited number of iterations for CGLS. Total number of iterations is 922. Using angles= 70°, freq= 12 MHz, bw= 3 MHz and no noise.

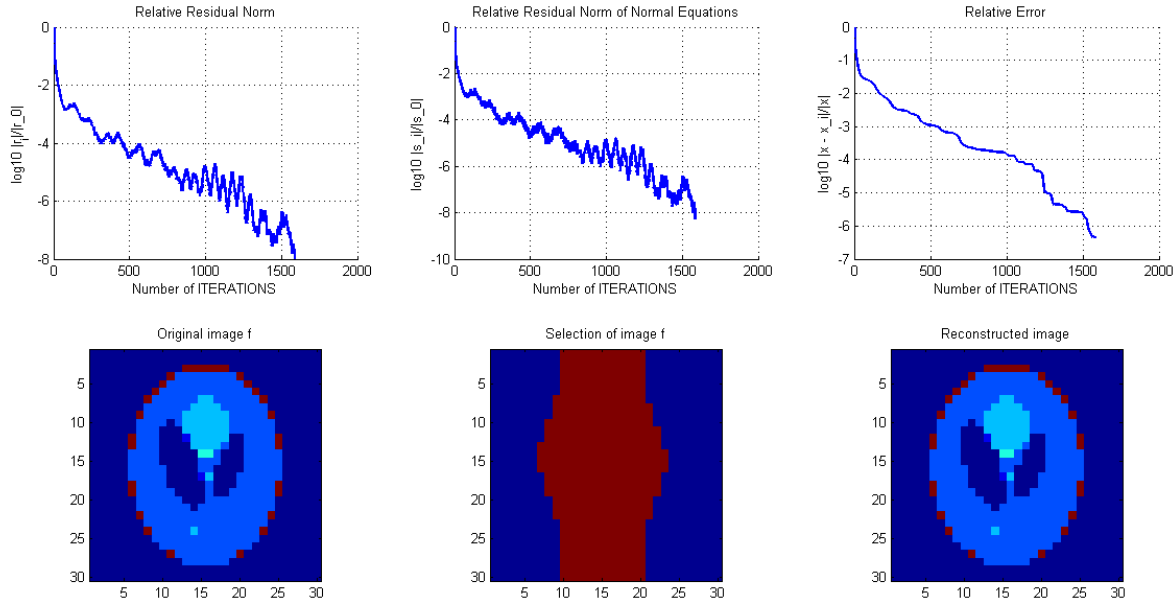

Figure D.12: Results of unlimited number of iterations for CGNE. Total number of iterations is 1586. Using angles= 70°, freq= 12 MHz, bw= 3 MHz and no noise.

Bibliography

[1] Fabio Baselice, Giampaolo Ferraioli, and Vito Pascazio. Relaxation time estimation from complex magnetic resonance images. *Sensors*, 10(4):3611–3625, 2010.

[2] Adi Ben-Israel and Thomas NE Greville. *Generalized inverses: theory and applications*, volume 15. Springer Science & Business Media, 2003.

[3] Ake Björck. *Numerical methods for least squares problems*. Siam, 1996.

[4] Ake Björck. *Numerical Methods in Matrix Computations*. Springer, 2015.

[5] Richard G Brewer and Erwin L Hahn. Atomic memory. *Scientific American*, 251(6):50–57, 1984.

[6] Robert W Brown, Y-C Norman Cheng, E Mark Haacke, Michael R Thompson, and Ramesh Venkatesan. *Magnetic resonance imaging: physical principles and sequence design*. John Wiley & Sons, 2014.

[7] Daniela Calvetti and Erkki Somersalo. *An Introduction to Bayesian Scientific Computing: Ten Lectures on Subjective Computing*, volume 2. Springer Science & Business Media, 2007.

[8] Govind B Chavhan, Paul S Babyn, Bejoy Thomas, Manohar M Shroff, and E Mark Haacke. Principles, techniques, and applications of t2*-based mr imaging and its special applications 1. *Radiographics*, 29 (5):1433–1449, 2009.

[9] Armstrong BD Sarracanie M Lev MH Rosen MS Wald LL. Cooley CZ., Stockmann JP. Two-dimensional imaging in a lightweight portable mri scanner without gradient coils. *Wiley online library*, 2015.

[10] Jeffrey A Fessler. Model-based image reconstruction for mri. *Signal Processing Magazine, IEEE*, 27(4): 81–89, 2010.

[11] Joachim Graessner. Bandwidth in mri. *MAGNETOM Flash*, 2:3–8, 2013.

[12] Per Christian Hansen. Regularization tools: a matlab package for analysis and solution of discrete ill-posed problems. *Numerical algorithms*, 6(1):1–35, 1994.

[13] Per Christian Hansen. *Discrete inverse problems: insight and algorithms*, volume 7. Siam, 2010.

[14] Per Christian Hansen and Dianne Prost O'Leary. The use of the l-curve in the regularization of discrete ill-posed problems. *SIAM Journal on Scientific Computing*, 14(6):1487–1503, 1993.

[15] SE Harms, PT Siemers, P Hildenbrand, and G Plum. Multiple spin echo magnetic resonance imaging of the brain. *Radiographics*, 6(1):117–134, 1986.

[16] J Hockx. Unknown. Master's thesis, Leiden University, https://openaccess.leidenuniv.nl/, 2017.

[17] Charles Howard. https://cure.org/hydrocephalus/.

[18] Zhi-Pei Liang and Paul C Lauterbur. *Principles of magnetic resonance imaging: a signal processing perspective*. The Institute of Electrical and Electronics Engineers Press, 2000.

[19] Joël Mispelter, Mihaela Lupu, and André Briguet. *NMR probeheads for biophysical and biomedical experiments: theoretical principles & practical guidelines*. Imperial College Press, 2006.

[20] D Mitchell and M Cohen. Mri principles. *Philadelphia, PA*, 2004.

[21] R.F. Remis. Electromagnetic field analysis of mri systems, research notes, 2015.

[22] Yousef Saad. *Iterative methods for sparse linear systems*. Siam, 2003.

[23] Michael A Saunders. Solution of sparse rectangular systems using lsqr and craig. *BIT Numerical Mathematics*, 35(4):588–604, 1995.

[24] AN Tikhonov and V Ya Arsenin. Solutions of ill-posed problems. *WH Winston, Washington, DC*, 330, 1977.

[25] MJ Vuik. Reconstructie van de aardkorst met tomografie (reconstruction of the earth's crust by tomography). 2010.

[26] Wikipedia. Halbach array, 2016. URL `https://en.wikipedia.org/wiki/Halbach_array`.

[27] Leonid P Yaroslavsky. *Theoretical Foundations of Digital Imaging Using MATLAB®*. CRC Press, 2012.